# ANALYSIS OF UNANCHORED LIQUID STORAGE TANKS UNDER SEISMIC LOADS

Thesis by

Ralf Peek

In Partial Fulfillment of the Requirements
for the Degree of
Doctor of Philosophy

California Institute of Technology
Pasadena, California

1986

(Submitted April 28, 1986)

## ACKNOWLEDGMENTS

My interest in this unanchored tanks problem arose in 1981, while working with Professor Hillary M. Irvine on a simplified method for the dynamic analysis of anchored tanks. I am most grateful for the opportunity to pursue this interest at Caltech in the years 1984-1986, with the encouragement, guidance and support of Professors Paul C. Jennings, Charles D. Babcock, George W. Housner, and John F. Hall. The willingness of two other members of the examining committee, Professors Ronald F. Scott and James K. Knowles to spend their time is much appreciated. Also, to Sotirios Natsiavas, thank you for several interesting discussions and for providing an extensive list of references.

Gloria T. Jackson and Sharon V. Beckenbach typed the manuscript with much patience and accuracy. Many of the figures were skillfully drawn by Cecilia S. Lin. Their dedication is gratefully appreciated.

Thank you also to Dr. Garrett D. Jeong for his help and advice in the use of Caltech's Prime computer.

Without the support of the National Science Foundation's Earthquake Hazard Reduction Program under Grant No. CEE81-19962 this work would not have been possible.

Finally, to my wife, Sopa, thank you for the many sacrifices she made, so that I could complete this work and the other degree requirements.

## ABSTRACT

Because of cost, cylindrical, ground supported liquid storage tanks are often not fixed to their foundation, even in seismic areas. For such an unanchored tank made of steel, the weight of the cylindrical shell is mostly insufficient to prevent local uplift due to seismic overturning moments. Although, for properly designed connecting pipes, uplift itself is not a problem, it results in larger vertical compressive stresses in the tank wall at the base, opposite to where the uplift occurs. These compressive stresses have often caused buckling, even in earthquakes which did not cause much damage to other structures.

Various investigators have studied the behavior of unanchored tanks experimentally, but, due to the complexity of the problem, so far very little theoretical work has been done. Two methods of analysis for static lateral loads are presented: An approximate one in which the restraining action of the base plate is modeled by nonlinear Winkler springs, and a more comprehensive one in which the two dimensional nonlinear contact problem is solved by the finite difference energy method. The theoretical results are compared with existing experimental results and with the approach from current U.S. design standards. The theoretical peak compressive stresses are in good agreement with the experimental results, but in some cases exceed those calculated by the code method by more than 100%.

Finally, a new design concept, by which the tank wall is preuplifted all around its circumference by inserting a ring filler is described. It will be shown theoretically and experimentally that this preuplift method substantially improves the lateral load capacity.

TABLE OF CONTENTS

TABLE OF CONTENTS (CONTINUED)

TABLE OF CONTENTS (CONTINUED)

TABLE OF CONTENTS (CONCLUDED)

# 1. INTRODUCTION

## 1.1 MOTIVATION

For anchored tanks, the tank wall is effectively fixed to a foundation which is sufficiently heavy to prevent uplift in the event of an earthquake. This means that the anchor bolts must be able to transmit the earthquake induced vertical tension in the tank wall to the foundation. Methods for the seismic analysis of such tanks are well established [Jacobsen (1949), Housner (1957, 1963), Veletsos and Yang (1977), Shaaban and Nash (1975), Haroun (1980), Haroun and Housner (1981, 1982 a,b), Liu and Lam (1983)], and complicating effects such as the excitation of modes with a higher circumferential wavenumber due to imperfections and geometrically nonlinear effects in the shell have also been considered [Turner (1978), Haroun (1980), Zui and Shinke (1984), Tani et al. (1984)].

In practice, anchoring a tank requires a large number of anchor bolts and suitable attachments welded onto the tank wall, so that the tension forces in the anchor bolts can be distributed evenly in the tank wall. Poorly designed attachments, or an attempt to carry too high a bolt force on a single attachment could result in tearing of the tank wall. Also, a fairly massive foundation may be required, especially for a larger tank. Thus, anchoring a tank is expensive, and, as a result, many tanks are unanchored, even in seismic areas. This is especially true for large capacity, broad tanks.

When an unanchored tank is subjected to strong ground shaking, the lateral force due to hydrodynamic pressures acting on the tank wall is of the same order of magnitude as the weight of the liquid. Unless the tank wall uplifts, the overturning moment induced by this lateral force can only be balanced by the stabilizing effect of the weight of the tank. For typical steel tanks the weight of the tank is much less than the weight of the contained liquid. Therefore, the weight of the tank is insufficient to balance the overturning moment due to hydrodynamic pressures acting on the tank wall, and the tank wall uplifts locally, as shown in Fig. 1.1. As a result, a crescent-shape strip of the base plate is also lifted from the foundation. The weight of the fluid resting on the uplifted portion of the base plate provides the resisting moment against further uplift.

It must be emphasized that unanchored tanks are special in that only the weight of fluid resting on the uplifted portion of the base plate contributes to the stabilizing moment, whereas the entire mass of liquid contributes to the overturning moment. This is different from the usual case in which the entire weight of a structure and its contents contributes to the stabilizing moment. As a result, unanchored fluid storage tanks are particularly prone to uplift problems.

Evidence of uplift can be found in the 1964 Alaska earthquake, during which snow found its way underneath the base plate of some tanks [Hanson (1973)] and during the 1971 San Fernando earthquake, when an anchor bolt of a 30 ft tall and 100 ft diameter tank was pulled up by 14 in [Figure 7.21 in Jennings (1971)].

Although uplift itself is not necessarily associated with serious damage, it can be accompanied by large deformations and major changes in the stresses in the tank. The consequences of large uplift can include,

(i) Damage and breakage of connecting pipes.

(ii) Buckling of the tank wall because the vertical compressive stresses in the portion of the tank wall which remains in contact with the ground on the other side of the tank are greatly increased.

(iii) Fracture at the junction between the base plate and the shell wall due to cyclic plastic hinge rotations.

Therefore, it is important to understand and be able to predict the behavior of unanchored liquid storage tanks in earthquakes.

As will be seen in the next subsection, some experimental studies on unanchored tanks have been performed. However, because of the complexity of the problem, not much theoretical work has been done. Although the experiments provide useful information for certain prototype tanks, the results are not directly applicable for other tank dimensions. Also, an improved understanding of the behavior of unanchored tanks can be gained from theoretical analysis and comparison with existing experimental results.

## 1.2 BACKGROUND

A very large number of papers have been published on the dynamic behavior of anchored tanks. However, here the attention is focused on the somewhat more scanty literature on unanchored tanks. Publications on unanchored tanks can be divided into three categories,

(i) Those documenting and evaluating the damage to unanchored tanks during past earthquakes.

(ii) Experimental studies.

(iii) Theoretical studies.

These will be dealt with in the next three subsections.

1.2.1 Experience from Past Earthquakes

The Prince William Sound, Alaska, earthquake of 1964 caused extensive damage to oil tanks, most of which appear to have been unanchored, as reported by Rinne (1967). For one of the tanks, plastic deformations in the base plate (presumably developing due to uplift) caused the tank to remain uplifted by 2 in after the earthquake. Many tanks buckled near the base due to vertical compressive stresses. A few of them collapsed as a consequence. Rinne defined a buckling resistance coefficient, $C_R$, to be the lateral force coefficient applied to the total weight of the tank and contents[1] for which the overturning stress[2] at the base is equal to a "theoretical buckling stress"[3]. He found that tanks for which $C_R > 0.44$ did not buckle at the base, whereas tanks for which $C_R < 0.44$ did. He concluded that there must have been a substantial amplification or resonance buildup of the lateral forces. An alternative explanation is that the tanks buckled at lower lateral forces because of the large concentration of compressive stresses which occurs if the tank uplifts.

---

1 Rinne approximated the total weight of the tank and contents by 1.1 times the weight of the contents, and assumed that the lateral force acts at a height of 0.4 h above the base, where h is the height to which the tank is filled.

2 The maximum vertical compressive stress at the base as calculated with the assumption that the tank is anchored.

3 The "theoretical buckling stress" used by Rinne is about 0.18 times what is generally known as the classical buckling stress [Timoshenko and Gere (1961), p. 458, equation 11-1].

Hanson (1973) took another look at the damage to tanks during the 1964 Alaska earthquake. He performed a calculation to estimate a peak compressive stress for an unanchored tank which exceeds the peak compressive stress for the anchored case by a factor of more than 5. Thus he concluded that a 20%g maximum ground acceleration and a lightly damped spectral velocity of $S_v$ = 2.0 ft/s was sufficiently intense to account for the observed damage. He also made the important suggestion that the base be thickened near the junction with the shell wall. This makes it possible for the base plate to carry the weight of the fluid on a larger uplifted portion. Thus a larger hold-down force can be developed. Finally, Hanson made the interesting observation that a possible source of roof damage is that "uplift on one side of the tank requires the roof to act as a structural diaphragm to hold the top of the shell circular. This diaphragm action tends to make the roof buckle unless it has been designed as a structural element." It will be seen in Chapters 3 and 4 that, for a tank without a roof, uplift can indeed result in large out-of-round distortions of the tank cross section associated with inextensional deformation modes of the cylindrical shell.

During the 1971 San Fernando earthquake [Jennings (1971)] several tanks were also damaged, including a 100 ft diameter, 30 ft tall wash-water tank at the Balboa Water Treatment Plant which experienced 14 in of uplift as evidenced by a pulled up anchor bolt. The tank was reported to be 1/2 to 3/4 full at the time of the earthquake and did not buckle at the base. However, at the top, the tank wall buckled inward,

possibly due to subatmospheric pressures induced by the increase in the enclosed volume which is associated with uplift.

The Imperial County earthquake [Leeds (1980)], of magnitude $M_L = 6.6$, also caused damage to a number of tanks located about 5 km from the Imperial Fault. Since strong ground motion data were available for nearby sites, Haroun (1983) was able to compare the observed damage with predictions based on existing methods of analysis. He computed overturning moments assuming that the tanks were anchored and rigid, and determined the actual and allowable maximum compressive stresses using the procedure recommended in the API standard 650 [American Petroleum Institute (1979)]. He concluded that the current standards and codes for seismic analysis of unanchored tanks lead to a conservative design. However, it is not clear whether the conservatism lies in the assumption that the lateral loads are the same as for a rigid anchored tank, in the method of estimating the peak compressive stress, or in the buckling criterion.

Moore and Wong (1984) collected an extensive set of damage data from the 1980 Livermore earthquake, the 1978 Miyaki-Ken-Oki earthquake in Japan, the 1971 San Fernando earthquake, and from Alaska. From this set of data and experimental results [Clough (1977), Niwa (1978), Clough and Niwa (1979), Niwa and Clough (1982)], they concluded that the maximum width of the uplifted strip of the base plate and the allowable vertical stress in the tank wall given in the API standard 650 are too small. By modifying these quantities they obtained good correlation with the observed damage.

Finally, the damage to a number of unanchored tanks during the 1983 Coalinga earthquake was studied by Manos and Clough (1985). Based on accelerographs from a nearby site recorded during the main event, and accelerographs from the tank sites recorded during aftershocks, they estimated peak ground accelerations ranging from 0.39g to 0.82g for the tank sites. Damage included buckling of the tank wall at the base, damage to floating roofs, spilling of oil over the top of many tanks, and damage to connecting pipes. All tanks included in the study were unanchored. Manos and Clough concluded that current U.S. practice [American Petroleum Institute (1979)] underestimates the sloshing response of tanks with floating roofs and does not adequately address the uplifting mechanism of tanks with floating roofs.

### 1.2.2 Experimental Studies

A number of shaking table tests were performed at the University of California at Berkeley [Clough (1977), Niwa (1978), Manos and Clough (1982)] using aluminum models, and for a full scale stainless steel wine tank [Niwa and Clough (1982)]. Based on the modulus of elasticity of aluminum, the models satisfy the requirement for similarity to steel prototypes which are three times larger. Uplift and out-of-round deformations of the cross section were a dominant feature of the response, and resulted in larger displacements and stresses in the tank wall. In several cases the measured vertical compressive stresses in the tank wall exceeded the code allowable values, without any signs of buckling or other distress. Manos and Clough (1982) measured stresses 2.85 and

2.35 times larger than the allowable from the AWWA [American Water Works Association (1979, 1984)] and API standards respectively. They also showed that the peak compressive stresses could be reduced by using a flexible foundation.

The observed response was quite complex, and the author believes that more can be learned from the test results than has been learned to date. Certainly these experimental results are an important basis for comparison with any analytical models.

Somewhat simpler experimental results are obtained from static tilt tests [Clough and Niwa (1979), Manos and Clough (1982), Shih (1981)] in which a lateral load is induced by tilting the tank. Shih (1981) has shown that the stresses due to tilting are similar to those induced by seismic lateral loads (if the inertia associated with out-of-round distortions is neglected). Some of the results of these tilt tests will be used in Chapters 4 and 5, for comparison with analytical results.

Shih (1981), and Shih and Babcock (1980, 1984) use a different approach for their experimental work: Their mylar tanks satisfy the requirements for similarity with steel tanks 40 times larger. As a result, models as small as 5 in in diameter can be used to represent steel prototypes of a realistic size. Such models are easy to fabricate. Since they are not damaged by buckling of the shell, the same tank can be used in a number of buckling experiments. Another advantage of mylar tanks is that residual stresses due to welding are avoided. On the other hand, since mylar sheets are too flexible for the use of straingages, stresses can only be determined by analysis. Also,

for plastic deformations of the steel prototype, the similarity conditions break down because mylar does not yield. This is important if the steel prototype experiences some plastic deformation prior to buckling.

The mylar tanks were tested on a shake table (with harmonic and transient excitation), and by static tilt. Test conditions which were varied include tank dimensions, base fixity condition (anchored or unanchored), top condition (with or without a roof or stiffening rim), and water level. In one of the transient tests the intensity of motion which produced buckling for an anchored tank is up to 10 times larger than for the unanchored case. Also, the experiments for the anchored case indicate that buckling occurs at stress levels close to the classical value.

### 1.2.3 Theoretical Work

Despite the very large number of publications on the behavior tanks in earthquakes, only a few deal with the analysis of unanchored tanks.

The method of analysis that has enjoyed the widest use is that of Wozniak and Mitchell (1978), which has been adopted in the AWWA and API standards: Using a rigid-plastic beam model for the base plate shown in Fig. 1.2, the maximum hold-down force due to the weight of fluid resting on an uplifted portion of the base plate is*

---

* Eq. 1.1 is valid for any consistent set of units.

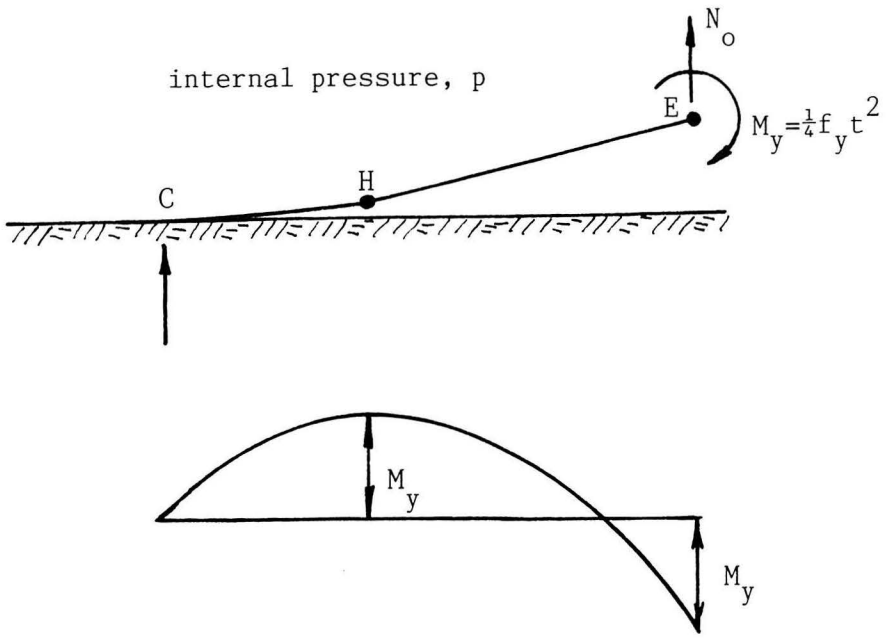


Figure 1.2: Rigid-plastic beam model used by Wozniak and Mitchell (1978) to calculate the hold-down force due to the weight of fluid resting on the uplifted portion of the base plate. Note: Since the moment at the plastic hinge location, H, is a maximum, the shear must vanish there. Therefore, the unknown distance HE and the force $N_o$ can be determined by balancing the vertical forces and moments for the free body HE. The hold down force is equal to the weight of fluid resting over the portion HE of the base plate.

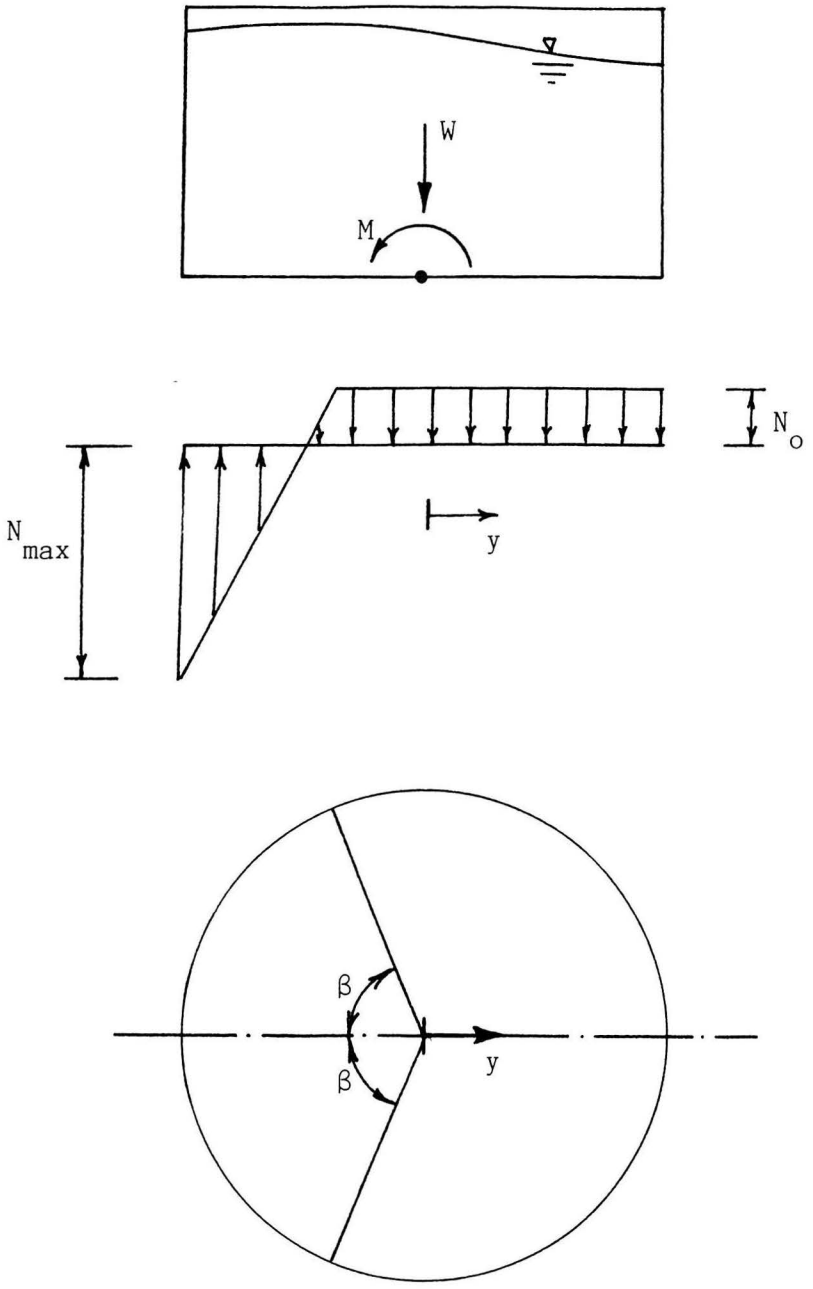


Figure 1.3: Assumed distribution of vertical forces in the tank wall at the base in the model of Wozniak and Mitchell (1978). Note: The parameters $N_{max}$ and $\beta$ are determined by balancing the vertical forces and moments acting on the cylindrical shell.

$$N_o = t\left[f_y p\right]^{1/2} \quad . \tag{1.1}$$

$N_o$ = hold down force per unit length along the circumference of the shell, which is also the vertical membrane tension developed in the shell at the base.

$t$ = thickness of the base plate.

$f_y$ = yield stress of the base plate.

$p$ = hydrostatic pressure acting on the base plate.

For a rigid-plastic beam, the force $N_o$ is independent of the amount of uplift. In reality however, the displacements required to develop the plastic hinges are so large that small deflection theory is no longer applicable. Nevertheless, Wozniak and Mitchell assumed that the hold down force given in Eq. 1.1 would be developed around the entire circumference except in a contact region which spans an angle $2\beta$. In this contact region, the vertical force in the tank wall at the base is assumed to vary linearly with respect to a coordinate y measured along the loading axis as shown in Fig. 1.3. The resulting assumed distribution of vertical forces in the tank wall contains two unknown parameters: The maximum vertical force in the tank wall, denoted by $N_{max}$ in Fig. 1.3, and the angle spanned by the contact region, $2\beta$. These two unknowns can be determined by balancing the vertical forces and moments acting on the shell.

What makes the model of Wozniak and Mitchell particularly simple is that the magnitudes of the displacements do not enter in the calculation. Other simplified methods have been proposed by Clough (1977),

Shih (1981), Cambra (1983), Ishida et al. (1985) and Leon and Kausel (1986). None of these consider the deformations of the shell in determining the extent of the contact region and the distribution of vertical stresses therein.

Auli, Fisher and Rammerstorfer (1985) present an analysis in which the vertical restraining action of the base plate and the foundation is modeled by a circular bed of nonlinear Winkler springs. In tension these springs represent the restraining action due to the weight of fluid resting on an uplifted portion of the base plate, and in compression they represent the rigidity of the foundation. A number of different models were studied in order to obtain the force-deflection of the springs in tension. In the one which best addresses the uplift problem, Auli et al. use the finite element method to solve the axisymmetric problem in which the base plate experiences a uniform uplift all around the circumference. The resulting relationship between uplifting force and uplifting displacement is then assumed to be applicable locally when the uplift varies around the circumference. Auli et al. also performed a stability analysis for the shell with and without imperfections, and found that buckling at the base occurred at stress levels close to the classical value.

The concept of using equivalent Winkler springs to model approximately the restraining action due to the base plate is also used in Chapter 4. The method of analysis presented therein was completed before the work of Auli et al. (1985) was known to the author or published, and can therefore be considered to be developed

independently. It will also be seen in Chapter 5 that there are instances when this method is not satisfactory.

So far the discussion on methods of analysis for unanchored tanks has focused on the analysis of the tank for given lateral loads. Rocking affects the dynamics of the tank, and therefore also the lateral load level. A number of papers address the problem of the dynamic analysis of liquid filled tanks including rocking [Ishida (1980), Sakai et al. (1984), Haroun and Ellaithy (1985)]. In some cases the base of the tank is assumed to participate in the rocking motion, in others the base of the tank is assumed to remain flat, and only the shell undergoes the rocking motion. What happens for an unanchored tank is somewhere in between these two extremes: Close to the tank wall, the base plate participates in the rocking motion, but at the center the base plate remains in contact with the ground.

Ishida and Kobayashi (1985) use a four degree of freedom dynamic model for a rocking tank. In order to obtain the properties of a rotational spring which resists the rocking motion for an unanchored tank, they assumed that the shell rotates as a rigid body. They also used a circular bed of nonlinear Winkler springs to model the resistance to vertical displacements of the tank wall at the base. An elastic-plastic beam model with axial tension served to estimate the resistance to uplift provided by the base plate. Ishida and Kobayashi also performed shaking table experiments, and compared the results with those from a time history analysis for their four degree of freedom system.

An effect which is not included in any of the dynamic rocking analyses is the vertical displacement of the combined center of gravity of the tank and contents: At any time, the vertical displacement field for the base plate can be decomposed into one component which is antisymmetric in the coordinate y (Fig. 1.3), and a component which is symmetric in y. During a cycle of rocking motion, the antisymmetric part also undergoes one cycle of motion, but the symmetric part undergoes two. Furthermore, the spatial average of the symmetric part over the base plate is non-zero, indicating that the center of gravity of the fluid undergoes two cycles of vertical motion for each cycle of rocking. This not only increases the effective period of oscillation, but may also contribute towards dangerously high hydrodynamic pressures.

## 1.3 SCOPE AND ORGANIZATION

The author believes that it is important to gain a thorough understanding of the statics problem of the tank subjected to lateral loads before much confidence can be placed in any dynamic solution. Therefore attention is focused on the analysis of the tank under given lateral loads, and comparison with (for the most part existing) experimental results.

Since, in a time history analysis, the solution to the dynamic problem is obtained by solving a statics problem at each time step, the solution presented is a key ingredient for solving the dynamic problem. The method of analysis chosen for the static case is such that it can readily be incorporated in a dynamic analysis. Also, any simplifying

approximations which may emerge from studying the static solution are also applicable for the dynamic case.

Although it is certainly desirable to obtain a dynamic solution to the problem, the uncertainty in the maximum seismic lateral load a tank might experience during its lifetime due to incomplete understanding of the dynamic behavior is probably no larger than the uncertainty about the intensity and frequency content of ground motion that might occur. Therefore, for design purposes, a justifiable approach is to design the tank for a given lateral load, which is estimated with due consideration of both sources of uncertainty.

In Chapter 2 the axisymmetric problem in which the tank is uniformly uplifted all around the circumference is solved. After studying the behavior of the shell in Chapter 3, the relationship between uplift and hold-down force from the axisymmetric analysis of Chapter 2 is used to define the properties of a bed of equivalent nonlinear Winkler springs at the base. The analysis of the tank on such a bed of springs is formulated in Chapter 4. The validity of this equivalent springs method is verified in Chapter 5 by solving the coupled, non-axisymmetric problem for the base plate and shell by the finite difference energy method. Both geometric and material nonlinearities are considered in the analysis. Finally, a new design concept is proposed and evaluated in Chapter 6, and the main conclusions are summarized in Chapter 7.

The symbols used are redefined in each chapter, except that the nomenclature for Chapter 3 also applies for Chapter 4. Thus, for example, in Chapter 2, u denotes the radial displacement of a point on the base plate, whereas in Chapter 3 the same symbol is redefined to denote the vertical displacement of a point on the cylindrical shell.

## 2. AXISYMMETRIC UPLIFT PROBLEM

When the tank wall uplifts due to earthquake induced overturning moments, it pulls the base plate up with it. Consequently, part of the weight of the fluid resting on the uplifted portion of the base plate becomes effective in resisting overturning moments. In this section the relationship between the radial extent of the uplifted portion of the base plate and the vertical uplift of the tank wall is studied by solving the axisymmetric problem in which the tank is uniformly uplifted all around its circumference (see Fig. 2.1). It will be seen that due to geometrically nonlinear effects in the base plate, membrane stresses develop which are of primary importance.

In strict terms, the solution to the axisymmetric problem is not applicable if the uplift varies around the circumference. However, if the uplifted width in the radial direction is small compared to the radius of the tank, and if the variations in vertical uplift are gradual, intuition suggests that the relation between vertical uplift and the uplifted width determined from the axisymmetric solution may be approximately applicable at any given point on the circumference. Thus, although axisymmetric uplift does not occur in an earthquake, the solution to this problem may be useful in developing an approximate method of analysis for seismic lateral loads.

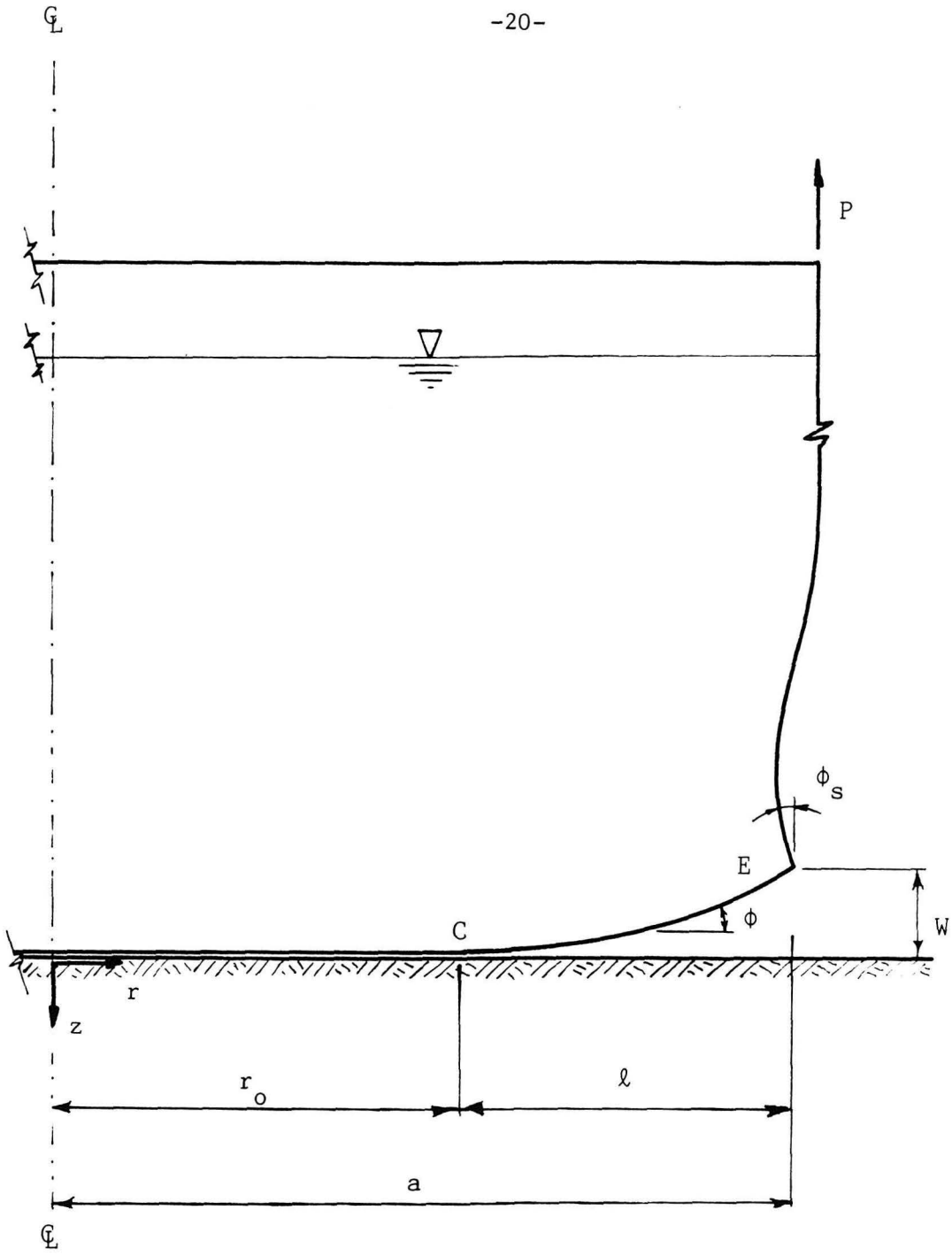


**Figure 2.1:** Definition of Axisymmetric Uplift Problem.

## 2.1 DEFINITION OF THE PROBLEM

The axisymmetric uplift problem considered is shown in Fig. 2.1. Point E will be referred to as the edge, and point C, as the contact point. The displacements are taken to be u and w in the r and z coordinate directions, respectively.

It is assumed that

a) The foundation is rigid and frictionless;

b) The tank is weightless and stress free when it is empty;

c) Both the base plate and the shell remain elastic, but a plastic hinge can form at the edge, E. The stresses and displacements due to the hydrostatic fluid load and an axisymmetric uplift force per unit length, P, applied at the top of the tank, are to be determined.

## 2.2 AXISYMMETRIC SHELL PROBLEM

Since the radial displacements of the shell are relatively small, the linear theory for an axisymmetrically loaded cylindrical shell (Timoshenko and Woinowsky-Krieger, 1959) is applicable. According to this theory, bending moments and shears in the shell decay rapidly with distance from the edge. As a result, the shell may be assumed to be sufficiently long that the solution depends only on the thickness and elastic properties of the lowest course of the shell. In addition, the fluid pressure is taken to be constant over the region of influence of the shell. With these assumptions, the displacement and rotation of the

shell at the edge are found to be given by

$$u = \frac{a(pa-\nu_s P)}{E_s t_s} + \frac{\lambda^2}{2D_s}[M-\lambda H] \qquad (2.1)$$

$$\phi_s = \frac{\lambda}{2D_s}[2M-\lambda H] \quad , \qquad (2.2)$$

in which

$u$ = radially outward component of displacement of the edge;

$\phi_s$ = rotation of the shell-wall at edge, taken to be positive in the anti-clockwise direction, as shown in Fig. 2.1;

$H$ = radially inward force acting on the shell;

$M$ = moment acting on the shell at the edge, defined to be positive when it acts in the same sense as the rotation $\phi_s$;

$D_s = E_s t_s^3/[12(1-\nu_s^2)]$, the flexural stiffness of shell;

$E_s, \nu_s$ = Young's modulus and Poisson's ratio for the shell, respectively;

$\lambda = [t_s a]^{1/2}/[3(1-\nu_s^2)]^{1/4}$, the characteristic length, which determines the rate of decay of bending moments in the shell;

$p$ = Fluid pressure at the edge (point E in Fig. 2.1).

a = Radius of tank, as defined in Fig. 2.1. Equations 2.1 and 2.2 will be used in the boundary conditions for the solution of the base plate problem.

## 2.3 GENERAL THEORY FOR BASE PLATE

For a typical tank the uplift may be of the order of 50 times the base plate thickness. Since linear plate theory is only applicable for deflections which are small compared to the plate thickness, a nonlinear theory is required. The moderate deflection theory, also known as the Von Karman plate theory [used by Timoshenko and Krieger (1959) and Stoker (1968)] is applicable as long as the deflections are not too large compared to dimensions of the plate. For even larger displacements, the large deflection theory must be used. Here the equations for large deflections are developed first, then the approximations of the Von Karman theory are introduced.

In the development of the large deflection theory the following assumptions are made in addition to those listed in Section 2.1:

1. The strains are small. As a result, the differences between natural strains and engineering strains, or Piola-Kirchoff stresses and Cauchy stresses, are negligible.
2. Changes in the distance of any point in the plate to the mid-surface are negligible.
3. The pressure p is applied at the mid-surface.

A typical segment of the base plate is shown in Fig. 2.2. It is assumed that a point on the midsurface of the base plate moves from a point (r,0) in the original (empty, not uplifted) configuration to a point (R,w) = (r + u,w) in the loaded (full and uplifted) configuration. The membrane forces, denoted $N_r$ in the radial direction and $N_\theta$ in the tangential direction, are given by

$$N_r = K(\varepsilon_r + \nu u/r) \tag{2.3}$$

$$N_\theta = K(\nu\varepsilon_r + u/r) \quad , \tag{2.4}$$

in which $\varepsilon_r$ is the strain in the radial direction, and K is the extensional rigidity given by

$$K = Et/(1-\nu^2) \quad , \tag{2.5}$$

in which E, $\nu$ and t are Young's Modulus, Poisson's Ratio, and the thickness of the base plate, respectively.

The radial and tangential moments, are taken to be positive when they induce tension on the bottom of the base plate, and are given by

$$M_r = D(\phi' + \nu \sin \phi/r) \tag{2.6}$$

$$M_\theta = D(\nu\phi' + \sin \phi/r) \quad , \tag{2.7}$$

in which $\phi$ is the slope angle defined in Figs. 2.1 and 2.2, $D = Kt^2/12$ is the flexural rigidity of the base plate, and the prime denotes differentiation with respect to r. Here the radial and circumferential curvatures, $\phi'$ and $\sin \phi/r$, respectively, are taken to be the rate of

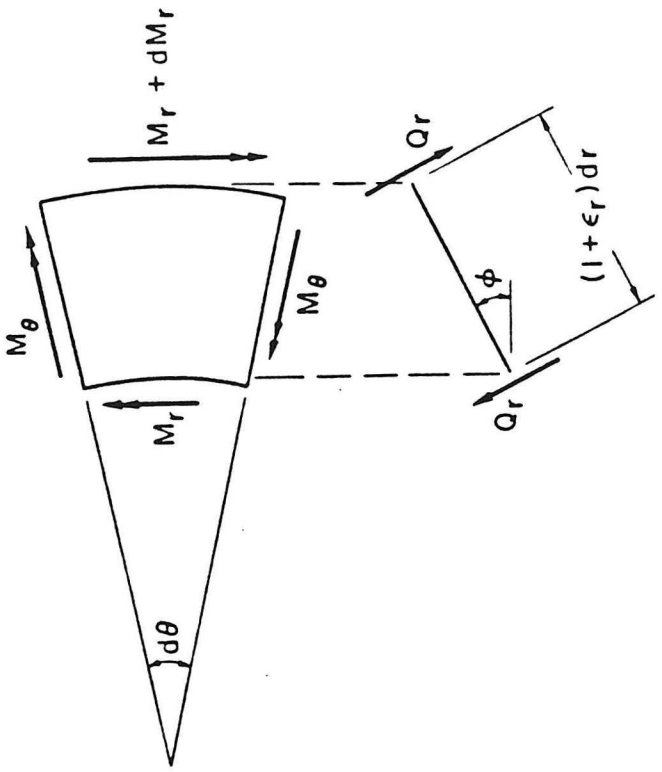


Figure 2.3

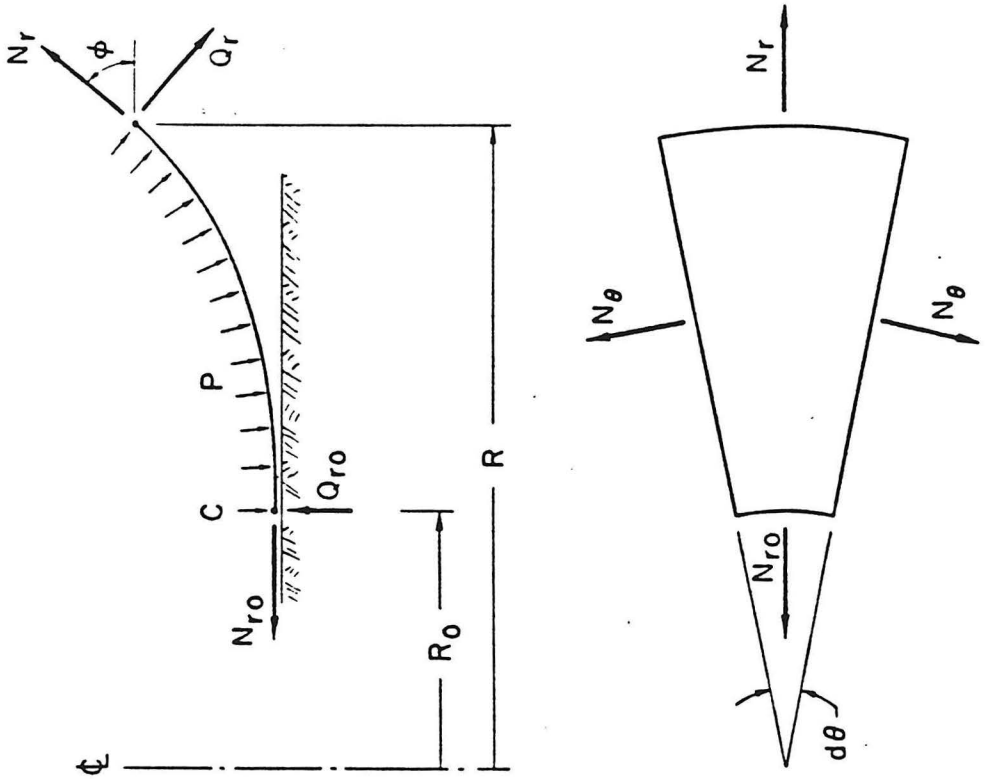


Figure 2.2

change of the unit normal vector to the mid surface per unit length in the original configuration. The radial shear force is denoted by $Q_r$, and acts as shown in Fig. 2.2. The shear force, the membrane forces, and the moments are expressed as forces per unit length in the original configuration.

Considering the changes in w and u for an infinitesimal change in the material coordinate gives

$$w' = -(1+\varepsilon_r) \sin \phi \tag{2.8}$$

$$u' = (R-r)' = \varepsilon_r - (1+\varepsilon_r)(1-\cos \phi) \quad . \tag{2.9}$$

The vertical and radial equilibrium equations for the segment of the base plate shown in Fig. 2.2 may be written as

$$rQ_r \cos \phi - rN_r \sin \phi = F_v \tag{2.10}$$

$$rQ_r \sin \phi + rN_r \cos \phi = F_h \quad , \tag{2.11}$$

in which

$$F_v = r_o Q_{ro} - \int_{R_o}^{R} pRdR \tag{2.12}$$

$$F_h = r_o N_{ro} + \int_{o}^{w} pRdw + \int_{r_o}^{r} N_\theta dr \quad . \tag{2.13}$$

In Eqs. 2.12 and 2.13 $N_{ro}$ and $Q_{ro}$ are the radial membrane force and the shear force at the contact point. This shear force is generated by a concentrated line reaction exerted by the foundation on the base plate. The concentrated contact reaction occurs without deformations since the foundation is assumed to be rigid. Without the contact reaction no solution would be possible; it is required for the sudden change in shear force. In reality however the foundation always has some flexibility, and the concentrated line reaction redistributes over a finite width.

A third equilibrium equation results from considering the moments acting about the tangential axis on an element of the plate shown in Fig. 2.3. In obtaining this equilibrium equation, note that the vertical components of the moments $M_\theta$ cancel, and only the radial component $M_\theta \cos\theta$ changes through an angle $d\theta$. The resulting moment-shear relation is

$$(rM_r)' = M_\theta \cos\theta + (1+\varepsilon_r) r Q_r \quad . \tag{2.14}$$

There are now nine equations, 2.3, 2.4, 2.6 through 2.11 and 2.14 for the nine variables: u, w, $\varepsilon_r$, $\phi$, $N_r$, $N_\theta$, $M_r$, $M_\theta$, $Q_r$. Many of the variables could readily be eliminated, but here it is found convenient to leave any simplifications of the governing equations for later, when the method of numerical solution is discussed.

The boundary conditions are as follows. At $r = r_o$, the contact point C:

$$w = 0 \, , \; \phi = 0 \, , \; M_r = 0 \tag{2.15}$$

$$K(1+\nu)u/r = K(1+\nu)\varepsilon_r = N_{ro} \, . \tag{2.16}$$

The last conditions arise because, since the foundation is frictionless, the entire portion of the base plate which remains in contact with the ground is in a state of uniform, isotropic membrane forces ($N_r = N_\theta = N_{ro}$ for $r < r_o$).

At r = a, the edge, Eqs. 2.1 and 2.2 for the shell need to be considered. The horizontal radial force and moment reaction conditions are:

$$H = N_r \cos \phi + Q_r \sin \phi \, , \tag{2.17}$$

and

$$M = -M_r \tag{2.18}$$

If no plastic hinge forms, the additional condition is $\phi = \phi_s$; if a plastic hinge does form, the moment at the edge must be the lesser of the yield moments of the base plate, or the shell. Defining the lesser of these two moments by $M_y$, the yield condition is

$$M = -M_r = M_y \, .$$

The effect of a stiffening ring at the edge could also be included, but is omitted here for simplicity.

## 2.4 SOLUTION FOR MODERATE DEFLECTIONS

For moderate deflections sin $\phi$ is replaced by $\phi$ and cos $\phi$ by unity, except that in Eq. 2.9, 1- cos $\phi$ is replaced by $\frac{1}{2}\phi^2$. In addition, terms containing the factor $\phi\varepsilon_r$ are neglected in Eqs. 2.8 and 2.9, and the radial component of the shear force $\phi Q_r$ is neglected in Eq. 2.11. Thus Eqs. 2.6, 2.7, 2.8, 2.9, 2.10, 2.11 and 2.14 become:

$$M_r = D(\phi' + \nu\phi/r) \tag{2.19}$$

$$M_\theta = D(\nu\phi' + \phi/r) \tag{2.20}$$

$$w' = -\phi \tag{2.21}$$

$$u' = \varepsilon_r - \tfrac{1}{2}\phi^2 \tag{2.22}$$

$$rQ_r - rN_r\phi = F_v \tag{2.23}$$

$$rN_r = F_h \tag{2.24}$$

$$(rM_r)' = M_\theta + rQ_r \tag{2.25}$$

Finally, the difference between R and r is neglected in Eq. 2.11 to give

$$F_v = r_o Q_{ro} - \int_{R_o}^{r} prdr \quad , \tag{2.26}$$

and the horizontal component of the pressure force is neglected in Eq. 2.13 to give

$$F_h = r_o N_{ro} + \int_{r_o}^{r} N_\theta dr \quad . \tag{2.27}$$

All other equations and boundary conditions remain the same except that the edge condition for radial force (Eq. 2.17) becomes $H = N_r$. This nonlinear contact problem is solved by the shooting method: The location of the contact point, as well as the radial membrane force ($N_{ro}$) and the shear ($Q_{ro}$) at the contact point are assumed. This defines an initial value problem starting at the contact point, which is readily solved numerically. However, unless by chance the correct values of $N_{ro}$ and $Q_{ro}$ were assumed, the solution of the initial value problem will not satisfy the boundary conditions at the edge. The mismatch in the boundary condition may be expressed as an out-of-balance force, termed $H_{ob}$, and an out-of-balance moment, $M_{ob}$. These out-of-balance forces depend on $N_{ro}$ and $Q_{ro}$. They must vanish in order that the correct solution to the problem be obtained. Symbolically, these requirements may be written as

$$H_{ob}(N_{ro}, Q_{ro}) = 0 \tag{2.28}$$

$$M_{ob}(N_{ro}, Q_{ro}) = 0 \tag{2.29}$$

These equations can be solved numerically, by Newton's method, to any desired degree of accuracy. The gradient matrix can be obtained from a set of linear, ordinary differential equations which are derived by considering a perturbation to the governing equations, or, more conveniently, by computing the gradient matrix numerically. Finally,

solving the problem for a number of locations of the contact point, a parametric description of the relationship between any two variables of interest can be obtained.

Consider now the solution of the initial value problem in which $N_r$ and $Q_r$ are known at the contact point. Perhaps the most natural approach is to eliminate all variables except the displacements u and w from the equations. This gives two coupled ordinary differential equations, of 3rd order in w and 2nd order in u, which can be solved by standard numerical methods. This was attempted by the author who found that assuming that u'' and w''' vary linearly between nodal points, and using a method similar to Newmark's method of integrating the equations of motion, gives very poor results for any practicable step size, h. It is expected that similar problems would be encountered for other numerical methods. The reason is that the equations contain the terms $u' + w'^2/2$ for the radial strain. Except very close to the contact point, the magnitude of both u' and $w'^2/2$ is much larger than the magnitude of the sum. For the case in which u'' and w''' are linear; u' is quadratic, w' is cubic, and $w'^2/2$ is a sixth degree polynomial. Although u' and $w'^2/2$ are smooth, the sum can exhibit strong variations over a steplength, h. A similar phenomenon occurs in the finite element method, and is known as membrane locking [Belytschko et al. (1984)]. The method described below avoids these difficulties by using an integrated version of the radial equilibrium equation, assuming that the radial strain varies smoothly within each step, and then calculating the corresponding variation in u.

It follows from Eqs. 2.3, 2.19, 2.20, 2.23, 2.24 and 2.25 that

$$\phi'' = [(F_v + \phi F_h)/D + \phi/r - \phi']/r \tag{2.30}$$

$$\varepsilon_r = (F_h/K - \nu u)/r \quad . \tag{2.31}$$

From the boundary conditions at the contact point (Eqs. 2.15, 2.16), it is readily shown that at $r = r_o$:

$$(u,\ \varepsilon_r,\ w,\ \phi,\ \phi',\ \phi'',\ F_h,\ F_v)$$

$$= \left(\frac{r_o N_{ro}}{K(1+\nu)},\ \frac{N_{ro}}{K(1+\nu)},\ 0,\ 0,\ 0,\ \frac{Q_{ro}}{D},\ r_o N_{ro},\ r_o Q_{ro}\right) \tag{2.32}$$

The variables on the left hand side of Eq. 2.32 will be termed the state variables*. Any quantity of interest can be expressed as a function of these state variables. Now, suppose all state variables are known at $r = r_1$, and characterize their values at this point by a subscript 1. Thus, $u(r_1) = u_1$, and so on. Let $r_2 = r_1 + h$ for a small step h, and characterize the values of the variables at $r = r_2$ by a subscript 2. Thus $u(r_2) = u_2$, and so on. Assuming next that $\varepsilon_r$ and $\phi''$ vary linearly between $r = r_1$, and $r = r_2$, then all state variables at $r = r_2$ may be obtained as a function of $\varepsilon_r$ and $\phi_2''$, by evaluating the following expressions in sequence.

$$\phi'_2 = \phi'_1 + h(\phi''_1 + \phi''_2)/2 \tag{2.33}$$

---

* They are not state variables in the strict mathematical sense of the word, because they are interrelated.

$$\phi_2 = \phi_1 + h\phi'_1 + h^2(2\phi''_1 + \phi''_2)/6 \tag{2.34}$$

$$w_2 = w_1 - h\phi_1 - h^2\phi'_1/2 - h^3(3\phi''_1 + \phi''_2)/24 \tag{2.35}$$

$$u_2 = u_1 + h(\varepsilon_{r1} + \varepsilon_{r2})/2 - h(\phi_1^2 + \phi_2^2)/4 \tag{2.36}$$

$$F_{h2} = F_{h1} + Kh\left[u_1/r_1 + u_2/r_2 + \nu(\varepsilon_{r1}+\varepsilon_{r2})\right]/2 \tag{2.37}$$

$$F_{v2} = F_{v1} - ph(r_2+r_1)/2 \tag{2.38}$$

Equations 2.33 to 2.35 are obtained by exact integration. Equations 2.36 to 2.38 result from trapezoidal integration, and Eq. 2.38 is exact if the fluid pressure p is constant between $r_1$ and $r_2$. Equations 2.33 to 2.38 together with Eqs. 2.30 and 2.31 applied at $r = r_2$ are the set of 8 equations which determine the state variables at $r = r_2$ given their value at $r = r_1$. Numerical solution is simplified by the following iterative procedure:

1. Start with $\phi''_2 = \phi''_1$ and $\varepsilon_{r2} = \varepsilon_{r1}$.
2. Calculate $\phi'_2$, $\phi_2$, $w_2$, $u_2$, $F_{h2}$, $F_{v2}$ from Eqs. 2.33 to 2.38.
3. Calculate $\phi''_2$ and $\varepsilon_{r2}$ from Eqs. 2.30 and 2.31.
4. Repeat steps 2 and 3 until convergence in $\phi''_2$ and $\varepsilon_{r2}$.

This scheme is applied repeatedly, starting with the values of the state variables at the contact point given in Eq. 2.32, until the entire solution to the initial value problem is generated. With this solution method, accurate results can be obtained with relatively large step sizes, h. The results are identical to those that would be obtained by

subdomain collocation: the average of the residual over each element vanishes. For the example presented in the next section (a = 57 in, $t = t_s = 0.078$ in, p = 8.67 psi) for a 9 in width of the uplifted strip, 9 steps at h = 1 in gives results accurate to 0.11% in $M_r$, 1.5% in w, 2.3% in u, 4.8% in $\phi$, 2.5% in $N_r$ and 2.4% in $N_\theta$. For 36 steps at h = 0.25 in, these percentages become 0.01%, 0.08%, 0.12%, 0.29%, 0.14%, and 0.15%, respectively. Of several methods attempted by the author this one yields the most accurate results for a given step size.

## 2.5 EXAMPLE PROBLEM

One tank for which stresses in the baseplate have been measured is the stainless steel wine tank tested by Niwa and Clough (1982). This tank has a radius of a = 57 in, the thicknesses of the base plate and the lowest course of the shell are $t = t_s = 0.078$in. It is assumed that the tank is filled with water to a depth of 20 ft, for which the hydrostatic water pressure is 8.67 psi. The elastic properties for the stainless steel are taken to be $E = 29 \times 10^6$ psi, and $\nu = 0.3$. Based on a yield strength of 70 ksi for the stainless steel, the yield moment for the plastic hinge which is allowed to form at the edge is found to be $M_y = 106.5$ in-lb/in. The displacements, shear forces, bending moments, and membrane forces for widths of the uplifted strip of 9 in and 18 in are shown in Figures 2.4 to 2.8. In Fig. 2.6 the shear force $Q_r$ is plotted as the continuous line, and the broken line shows the total shear, including the shear force $Q_r$ and the vertical component of the membrane force, $-\phi N_r$ (see Fig. 2.2). The difference between the broken

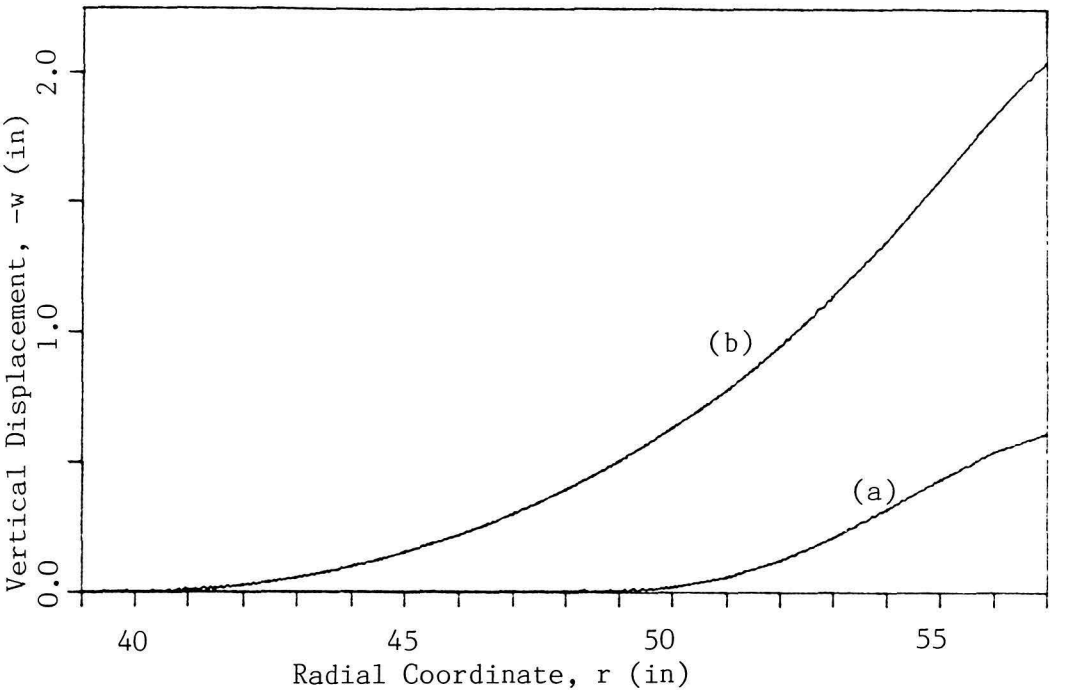


**Figure 2.4:** Vertical uplift for the wine tank of Niwa and Clough (1982); (a) for 9in uplifted width, (b) for 18in uplifted width.

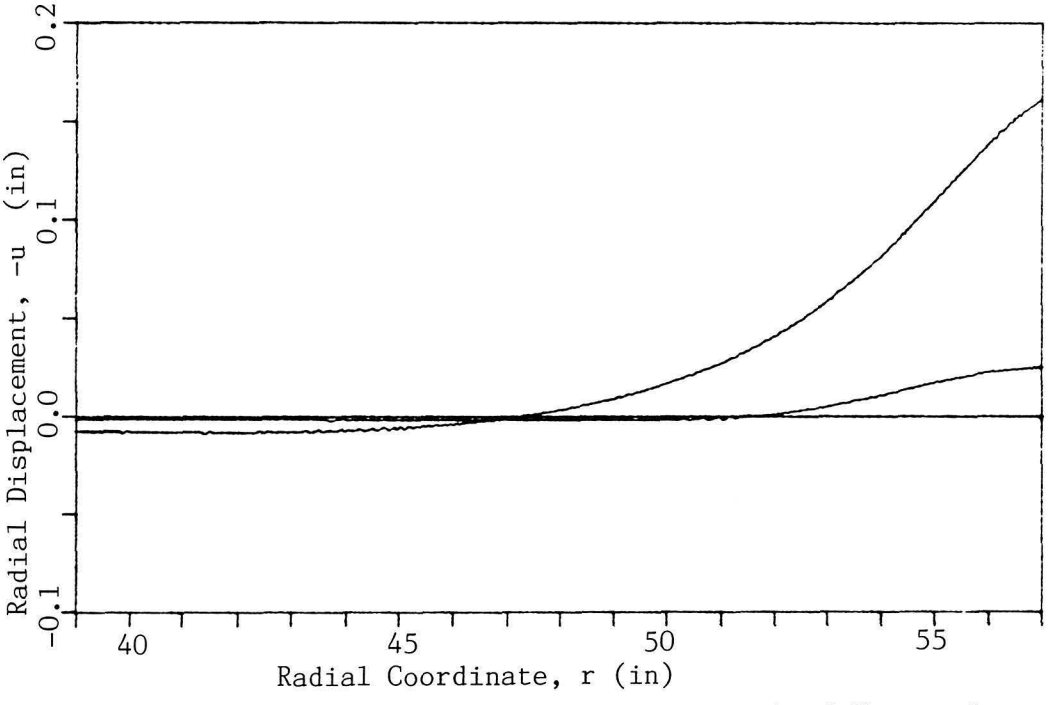


**Figure 2.5** Radial Displacement for the wine tank of Niwa and Clough (1982); (a) for 9in uplifted width, (b) for 18in uplifted width.

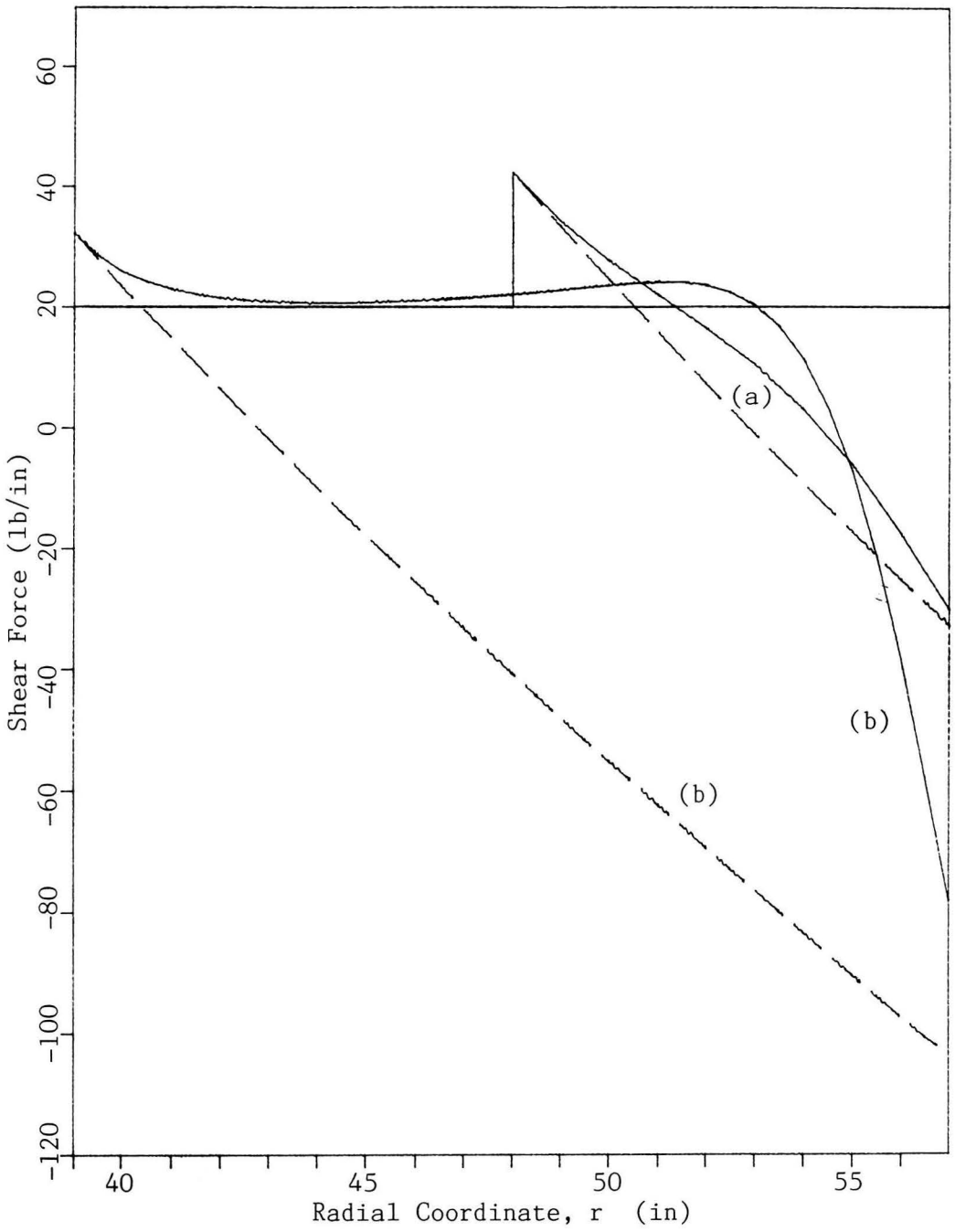


**Figure 2.6:** Shear force $Q_r$ (continuous lines), and total shear $Q_r - \phi N_r$ (broken lines) for the wine tank of Niwa and Clough (1982) for (a) 9in uplifted width, and (b) 18in uplifted width.

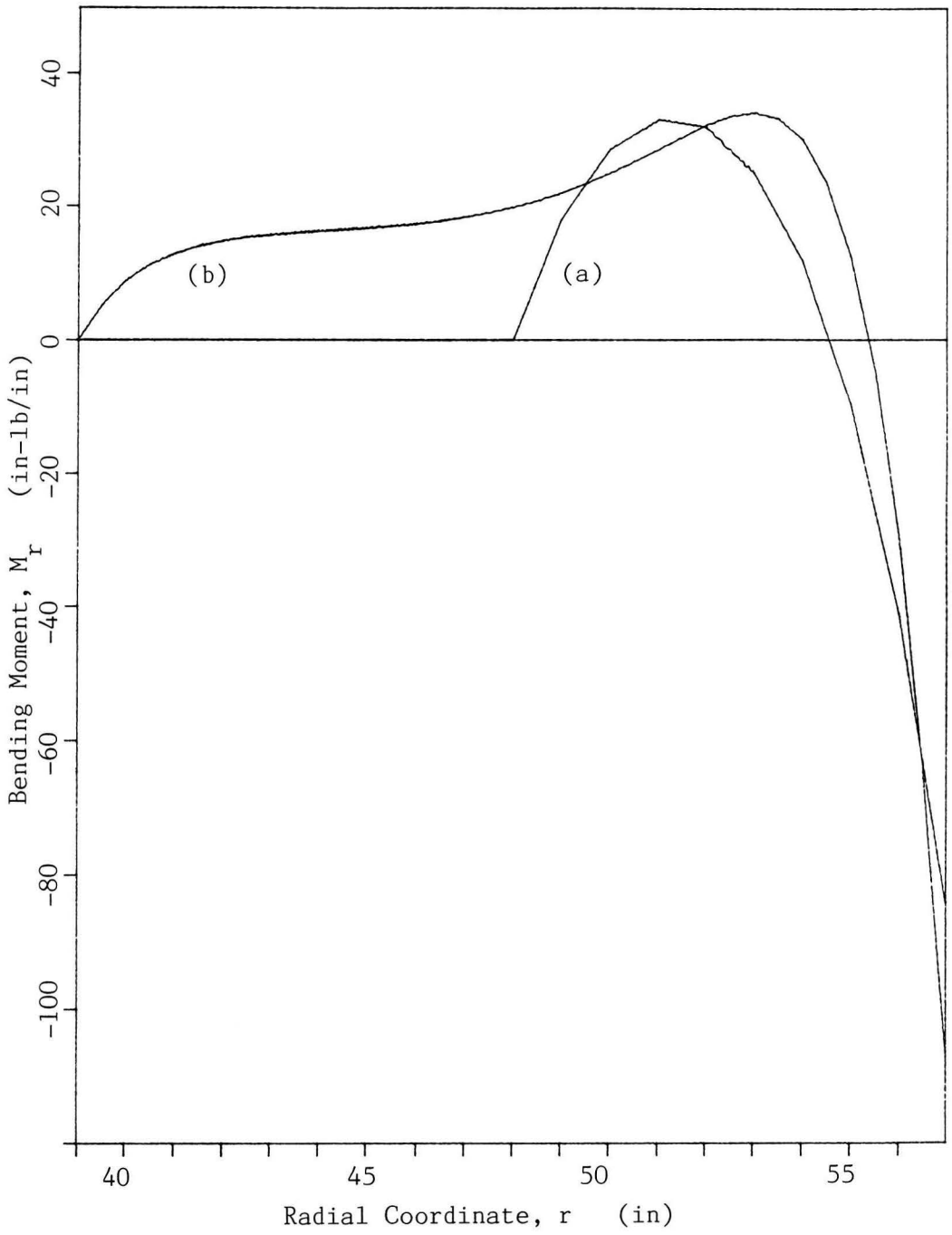


**Figure 2.7:** Radial bending moments for the wine tank of Niwa and Clough (1982), for (a) 9in uplifted, and (b) 18in uplifted width.

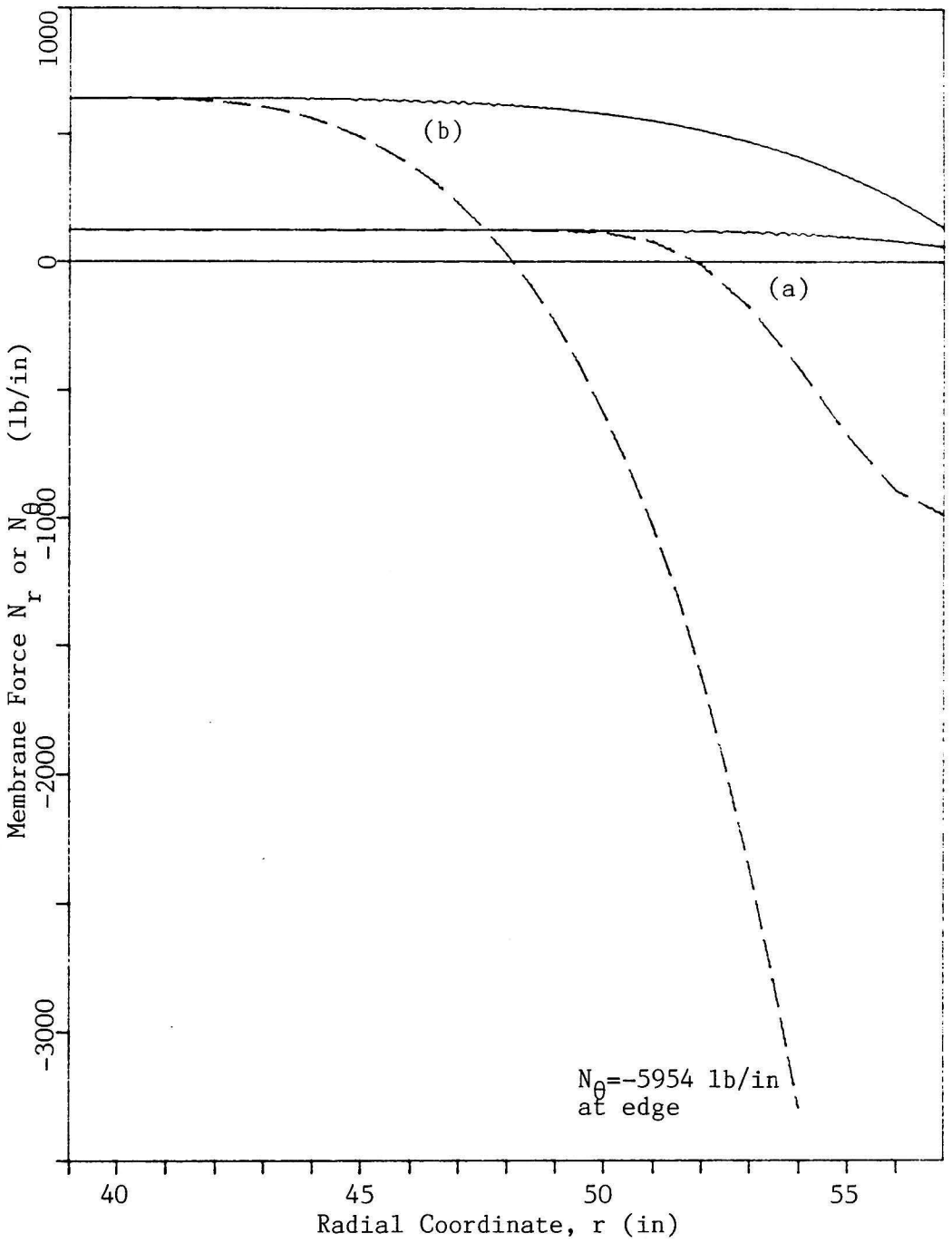


**Figure 2.8:** Radial Membrane force $N_r$ (continuous lines) and circumferencial membrane force $N_\theta$ (broken lines) for the wine tank tested by Niwa and Clough (1982), (a) for 9in uplifted width, and (b) for 18in uplifted width.

line and the continuous line is the vertical component of the radial membrane force, $\phi N_r$. For the case when small deflection theory is applicable, $\phi N_r$ is negligible compared to $Q_r$, and the broken and continuous lines would coincide. Figure 2.6 shows that even when the width of the uplifted strip is only 9 in, small deflection theory would be in error. For an uplifted width of 18 in, the shear is carried almost entirely by the membrane force $N_r$, except in localized boundary layers near the edge and contact point.

The radial membrane forces are shown in Fig. 2.8. They are generated almost entirely by nonlinear effects: Due to the finite slope of the baseplate in the radial direction, $\phi$, there is a tendency for the baseplate to move radially inwards. This inward displacement is restricted by the tank wall and also by the base plate itself which resists any axisymmetric deformation. Such restrictions to inward motion generate the radial membrane stresses. The restraining effect of the tank wall is represented by the radial membrane force at the edge. The increase in the membrane force inward from the edge is due to the restriction from the baseplate itself. It arises because the baseplate is being deformed into a non-developable shape. As a consequence of membrane action, the bending moments (Figs. 2.7 and 2.9) are relatively small and do not increase as the uplifted width is increased from 9 in to 18 in. In contrast, for the linear theory, the bending moments increase as the square of the uplifted width, and the shape of the bending moment diagram is close to parabolic.

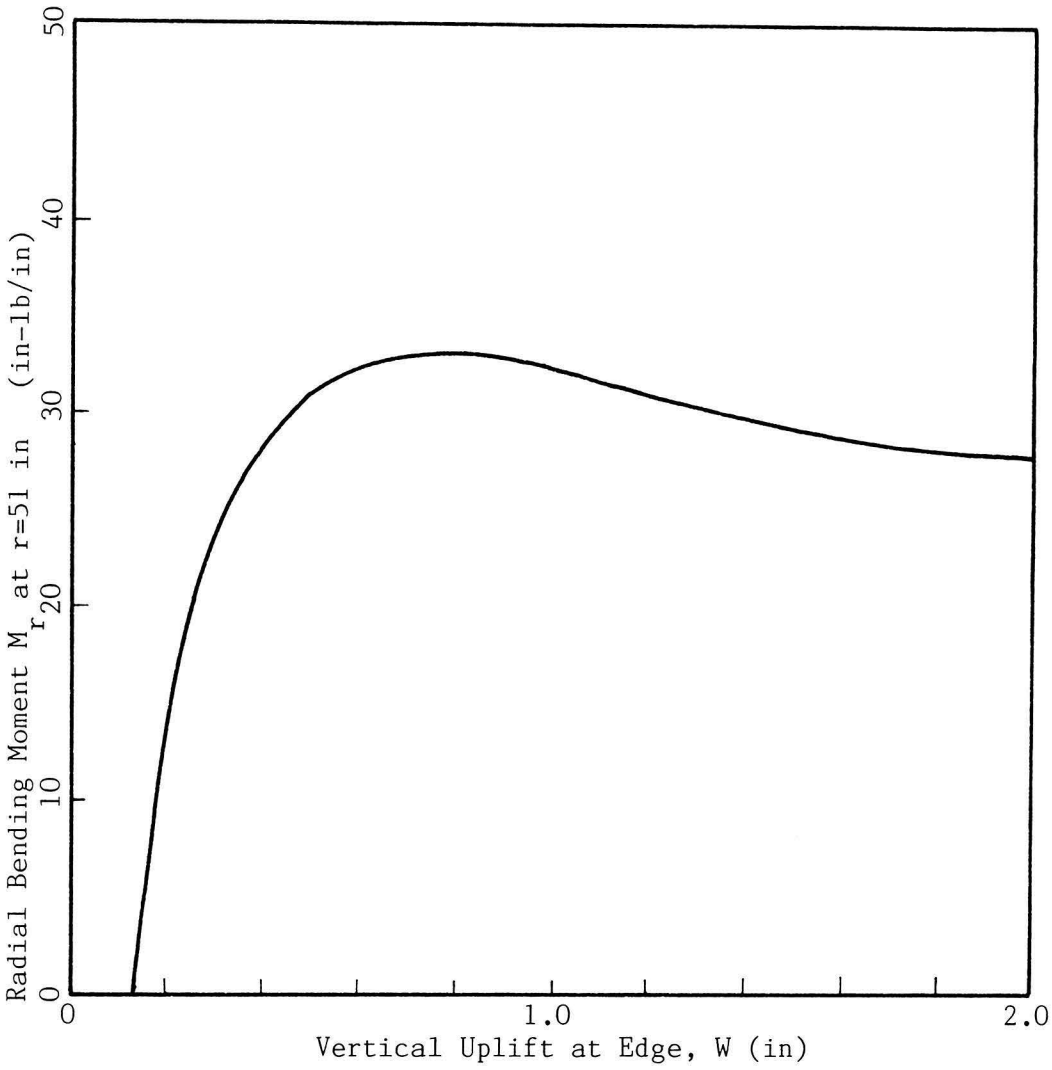


**Figure 2.9:** Relationship between radial bending moment at r=51 in (6 in inward from edge) and vertical uplift at edge for the wine tank tested by Niwa and Clough (1982).

## 2.6 SOLUTION FOR LARGE DEFLECTIONS

The governing equations for large deflections have already been developed. It remains to cast them in a convenient form for numerical implementation: Solving Eqs. 2.10 and 2.11 for $Q_r$ and $N_r$ gives

$$Q_r = \left[F_v \cos \phi + F_h \sin \phi\right]/r \tag{2.39}$$

$$N_r = \left[-F_v \sin \phi + F_h \cos \phi\right]/r \quad . \tag{2.40}$$

Substituting Eqs. 2.6, 2.7 and 2.39 into Eq. 2.14 gives

$$\phi'' = \left[(1+\varepsilon_r)(F_v \cos \phi + F_h \sin \phi)/D + \sin \phi \cos \phi/r - \phi'\right]/r \quad . \tag{2.41}$$

Substituting Eq. 2.40 into Eq. 2.3:

$$\varepsilon_r = \left[(-F_v \sin \phi + F_h \cos \phi)/K - \nu u\right]/r \quad . \tag{2.42}$$

The numerical solution procedure is identical to that for moderate deflections except that Eqs. 2.30 and 2.31 are replaced by Eqs. 2.41 and 2.42, and Eqs. 2.35 to 2.38 are replaced by

$$w_2 = w_1 - h\left[(1+\varepsilon_{r1}) \sin \phi_1 + (1+\varepsilon_{r2}) \sin \phi_2\right]/2 \quad , \tag{2.43}$$

$$u_2 = u_1 + h\left[\sum_{i=1}^{2} \varepsilon_{r_i} + (1+\varepsilon_{ri})(1-\cos \phi_i)\right]/2 \tag{2.44}$$

$$F_{v2} = F_{v1} - p(R_2^2 - R_1^2)/2 \tag{2.45}$$

$$F_{h2} = F_{h1} + p(w_2-w_1)(R_1+R_2)/2 + Kh\left[u_1/r_1 + u_2/r_2 + \nu(\varepsilon_{r1}+\varepsilon_{r2})\right]/2 \quad , \tag{2.46}$$

in which

$$R_i = r_i + u_i \quad , \quad i = 1,2 \quad . \tag{2.47}$$

Equations 2.43 to 2.47 are obtained by trapezoidal integration of Eqs. 2.8, 2.9, 2.12 and 2.13. In evaluating 1-cos $\phi$ for small values of $\phi$, the Taylor series expansion must be used to avoid numerical truncation errors. By considering enough terms, 1-cos $\phi$ can be evaluated to the full accuracy of the machine used.

As an example, the wine tank tested by Niwa and Clough (1982) is considered again. The results for large deflections are so close to those for moderate deflections that the difference could not be seen on a plot. This confirms that the deflections in this problem (involving rotations up to around 0.2 radians) are characterizable as moderate, not large.

## 2.7 COMPARISON WITH EXPERIMENTAL RESULTS

If the width of the uplifted strip is small compared to the radius of the tank, the conditions in the uplifted portion of a rocking tank appear to be much the same as the conditions for the axisymmetric uplift problem with the same amount of uplift at the edge. If this is so for a rocking tank, for which stresses are changing as a function of the circumferential angle, $\theta$, the stresses and displacements for any value of $\theta$ may be approximated by those from the solution of the axisymmetric problem with the appropriate vertical uplift at the edge. When this hypothesis applies, the variations in stresses and displacements in the circumferential direction will be referred to as weak. The comparison

between experimental and theoretical radial membrane strains shown in Fig. 2.10 is based on the assumption that circumferential variations are weak and that the hydrodynamic pressure is small compared to the static fluid pressure, so that its effect on the uplifted portion of the baseplate may be neglected. At time 8.0s in Niwa and Clough's experimental results, a peak uplift of about 1.6 in occurs. The experimental points in Fig. 2.10 represent the measured radial strains at various locations at time 8.0s, and the continuous curve represents the axisymmetric solution for the case when the uplift at the edge is 1.6 in. As can be seen from Fig. 2.10, both theory and experiment show very high membrane strains, but the spatial variations of membrane strain differ: Theory predicts a steady increase in the radial membrane strain towards the edge, due mainly to Poisson's ratio strains induced by the very large hoop compressive force, $N_\theta$ (Fig. 2.8). In contrast, the experimental strains increase from 12 in to 6 in from the edge, then drop dramatically, being close to zero at 3 in from the edge. Possible reasons for this discrepancy include:

a) The neglected effect of hydrodynamic pressures.

b) Inapplicability of the assumption that the axisymmetric solution applies to non-axisymmetric uplift (assumption of weak circumferential variations).

c) Experimental error.

d) Buckling of the base plate due to the large compressive stresses in the circumferential direction.

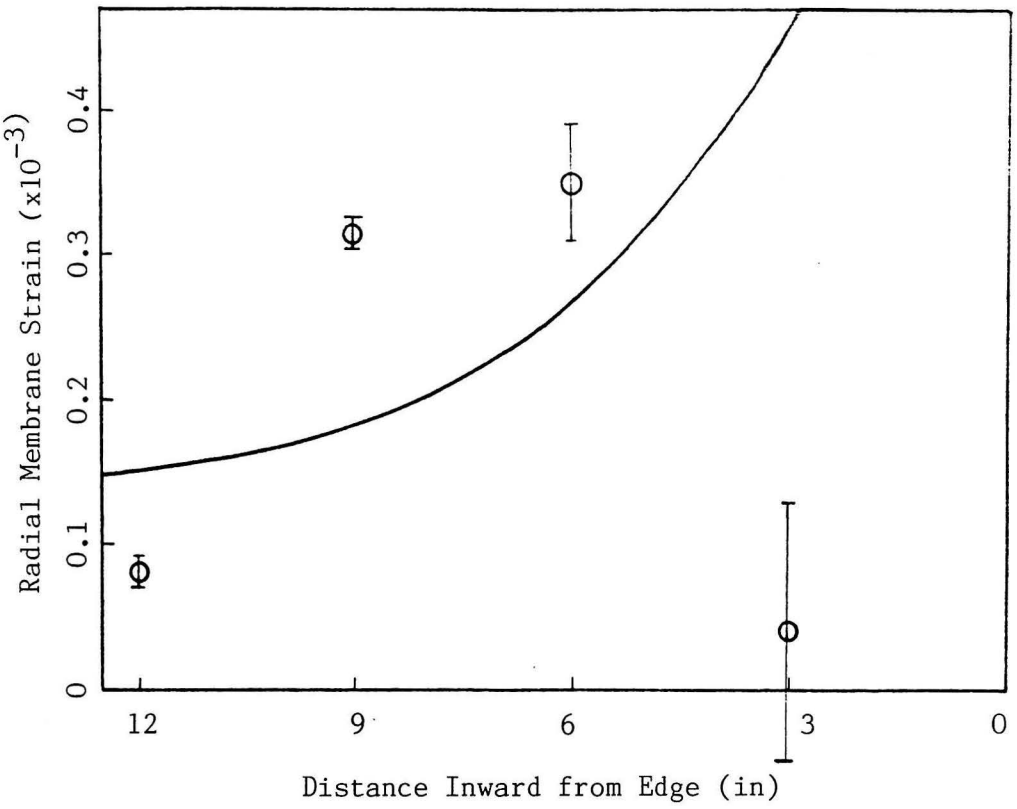


**Figure 2.10:** Theory versus experiment comparison of radial membrane strains.

o Experimental points, scaled from figures in Niwa and Clough (1982) at time=8s.

--- Axisymmetric solution for a verical uplift at the edge (W=1.62 in) matching the measured vertical uplift at time=8s.

[Note: Since original experimental data are no longer available, experimental strains had to be scaled from the figures in the journal paper. The error bars indicate the error in this scaling operation only.]

Which one of these explanations applies, or what combination, is not clear, but some assessment is possible.

Hydrodynamic pressures have been measured in the experiment, and are of the order of one-half the hydrostatic pressure. If variations in the circumferential direction are indeed weak, it would be possible to carry out the axisymmetric analysis with a modified pressure, thus obtaining a solution which includes the effects of hydrodynamic pressures. Such a corrected theoretical solution would exhibit much the same trends as the solution already obtained. Therefore the effect of hydrodynamic pressure alone is not considered to be a valid explanation for the drop in the experimental radial membrane strain close to the edge.

The assumption of weak circumferential variations is debatable: If it applies, the large circumferential compressive forces $N_\theta$ in the base plate must vary around the circumference just as the uplift does. It seems that, unless this is accompanied by large shear forces, $N_{r\theta}$, such changes in $N_\theta$ would violate equilibrium in the circumferential direction. However, it is hard to understand how the relatively slow variation in uplift around the circumference could cause the rather dramatic change in strains observed.

Buckling of the base plate by circumferential compression is thought to be the most likely explanation. Based on the theory of buckling of plates under uniform uniaxial stress, and an estimated effective half wavelength of 5 in in the radial and circumferential directions, a buckling circumferential force of $N_\theta$ = 2000 lb/in was

calculated. Although, due to prebuckling curvature, the actual buckling stress is somewhat higher than that predicted by the theory for flat plates, buckling still seems likely before the maximum circumferential force ($N_\theta$ = 5954 lb/in shown in Fig. 2.8 for 18 in uplifted width) is reached.

To define more precisely when buckling by circumferential compression may be expected to occur, the computer program BOSOR5 (Buckling of Shells of Revolution) developed by Bushnell (1974) was used. The capabilities of this program include material and geometrically nonlinear analysis of shells (and as a special case, plates) of revolution subjected to axisymmetric loads, and determination of bifurcation loads for non-axisymmetric buckling modes. Numerical solution of the governing equations is based on the finite difference energy method. Just as in the finite element method, the strains at integration points are expressed in terms of nodal displacements, and the contributions to the stiffness matrix from each integration point are summed. However, whereas in the finite element method a displacement field is defined within each element, and strains are computed by differentiation of this displacement field; in the finite difference energy method, strains are computed by finite difference expressions directly in terms of nodal displacements. Although the capabilities of BOSOR5 do not include contact problems, knowledge of the prebuckling solution from the shooting method makes it possible to simulate the prebuckling conditions in the base plate by judicious choice of constraints and loading. Details of how this can be achieved are given in Appendix A.

Using BOSOR5 to look at the stability of asymmetric modes for various locations of the contact point, it is found that the critical mode occurs for n = 33 circumferential waves, when the radial extent of the uplifted width is 12.75 in, the vertical uplift of the tank wall is 1.31 in, and the circumferential force at the edge is 3415 lb/in. The buckling modes are shown in Fig. 2.11. Also this type of buckling is illustrated in Fig. 2.12 for a mylar tank.

After the base plate buckles, the magnitude of circumferential compressive force, $|N_\theta|$, increases more slowly with increasing uplift. Via Poisson's effect, this means that the radial membrane strains also increase more slowly. In addition, since the radial membrane tension is for the most part generated by the hoop compressive forces, the radial membrane tension, $N_r$, also increases more slowly. Finally, there are local effects associated with buckling which vary over a half-wavelength. These can further influence experimental strain readings. Thus, bifurcation buckling appears to be the most likely explanation of the difference between theory and experimental points in Fig. 2.10. However, the other effects discussed may be contributing factors, too.

## 2.8 CONCLUSIONS

Solutions to the problem of uniform axisymmetric uplift of an unanchored filled liquid tank indicate that:

1. Large membrane stresses develop in the base plate. These membrane stresses carry a large part of the fluid pressure on

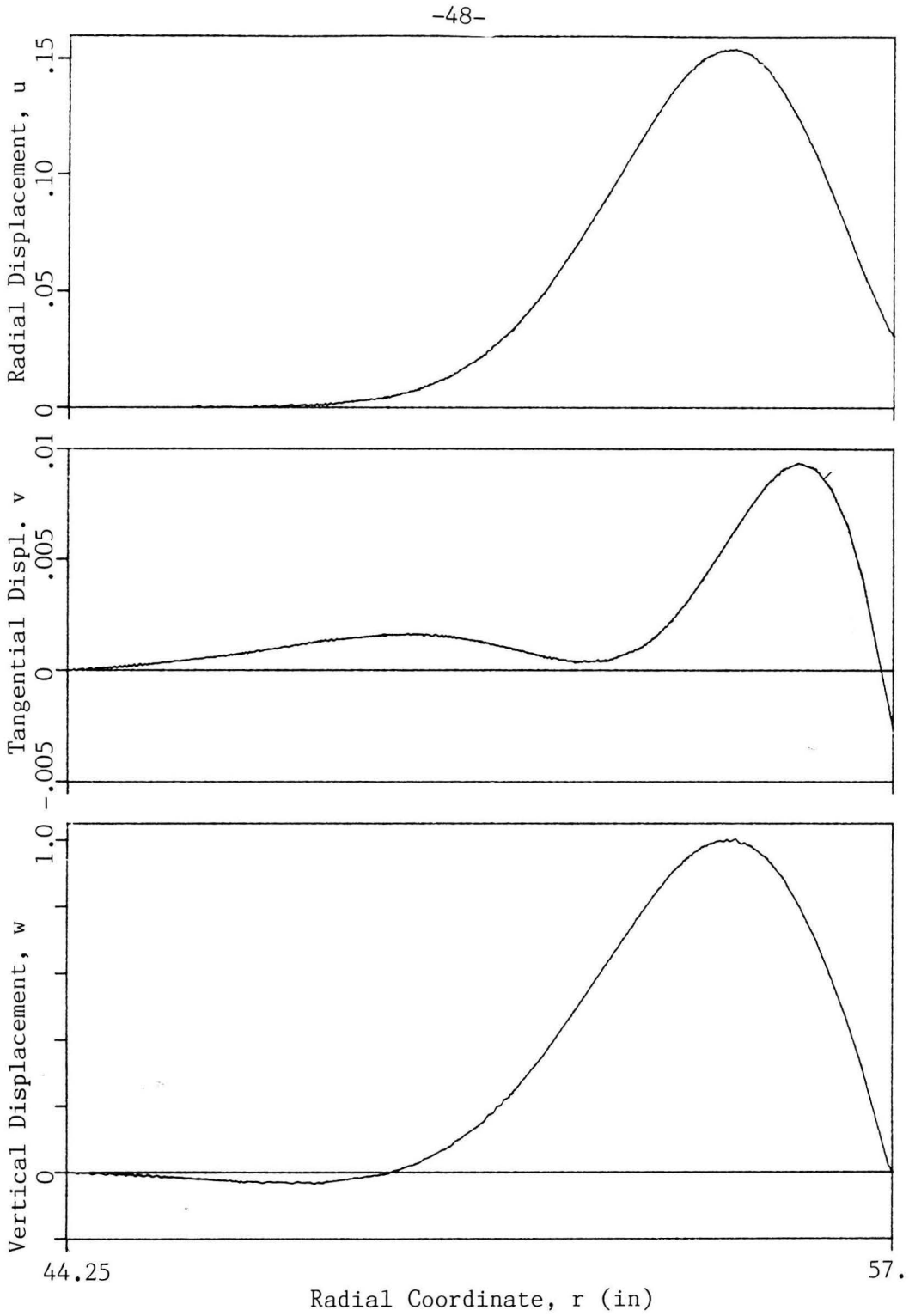


**Figure 2.11:** Buckling mode (eigenvector) for the wine tank of Niwa and Clough (1982), normalized so that the largest displacement is 1.0. Circumferencial wave number, n=33.

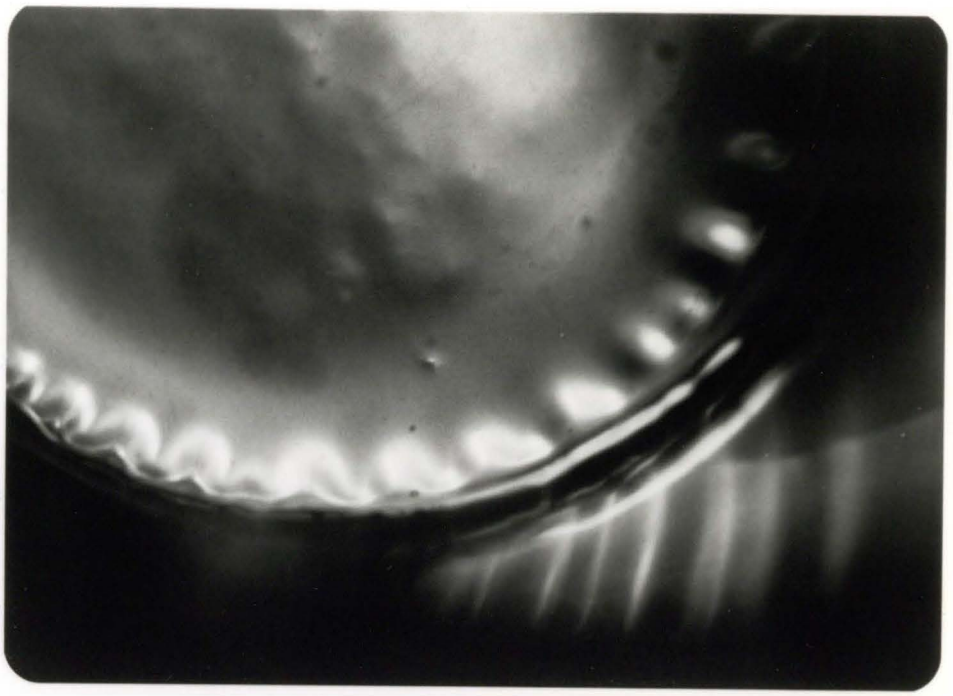

**Figure 2.12:**

Reflected light photograph of the buckles in the base plate of a mylar tank similar to the ones used by Shih(1981). An axisymmetric uplift of 1/16" was applied by inserting a ring filler under the shell wall at the edge. The ring filler consists of a sheet of plexiglass with a hole of diameter a few hundredth of an inch less than the inner diameter of the shell. The dimensions of this tank are 5" for the diameter, and 0.002" for the thickness of the shell and the base plate. It is filled with water to a depth of a few inches.

the uplifted portion of the base plate.

2. Bending stresses are relatively small except at the cylinder base plate joint, where a plastic hinge is expected to form.
3. For the realistic example studied, results obtained by the large deflection theory are virtually identical to those from the moderate deflection (Von Karman) plate theory.
4. For large enough uplift, buckling of the base plate due to the circumferential compressive forces occurs.
5. Buckling of the base plate is the most likely explanation of the difference between the theoretical and experimental radial membrane strains shown in Fig. 2.10.

## 3. ANALYSIS AND BEHAVIOR OF THE CYLINDRICAL SHELL

In this chapter, some elementary solutions relevant for understanding the behavior of the shell subjected to seismic loads and uplift are discussed, and certain results are developed for later use.

If the material yields at a critical section in the shell, such as near the base, it is likely that buckling would occur as a consequence of the drastic reduction in the material stiffness. Hence, from a design viewpoint, it is desirable to prevent yielding in the shell. Also, for the purpose of analysis of a tank at loads below the collapse load, plasticity in the shell need not be considered.

The importance of considering geometric nonlinearities in the shell is more debatable, and will be discussed later. As a first approximation, linear shell theory is assumed to hold.

The linear analysis of cylindrical (or, more generally, conical) shells using annular finite elements is well established, e.g., Klein (1964). This approach has been used by Haroun (1980), who also included the nonlinear effects of the hoop force due to the hydrostatic pressure. These results, as well as added stiffness matrices for the pressure-rotation effect on the hydrostatic pressure, are summarized in Appendix B. In the following pages some elementary solutions in the linear theory of cylindrical shells are examined; these results are relevant in understanding the behavior of an unanchored fluid storage tank.

Using superposition, the solution for an unanchored tank can be expressed as the sum of:

a) the solution for an anchored tank subjected to the loads experienced by the unanchored tank, and

b) the solution for imposed displacements at the base of the tank, and no other applied loads.

These two solutions will be discussed in sections 3.2 to 3.4, after presenting some basic definitions.

## 3.1 DEFINITIONS

The coordinates and displacement components are defined in Fig. 3.1. All definitions coincide with those of Flügge (1960), Chapter 5, except that the angle which defines the point on the circumference is denoted by $\theta$ instead of Flügge's $\phi$. In accordance with Flügge's notation, the components of displacement are taken to be u in the direction of increasing x, v in the direction of increasing $\theta$, and w in the radially outwards direction. The internal membrane forces, $N_x$, $N_\theta$, $N_{x\theta}$, $N_{\theta x}$, are defined in Fig. 3.1b, and the internal moments $M_x$, $M_\theta$, $M_{x\theta}$ and $M_{\theta x}$ are taken to be positive when they generate a positive stress at the inside of the shell. Shears $Q_x$ and $Q_\theta$, defined in Fig. 3.1b, are positive when they act radially inward on the face for which the outward pointing normal is in the positive x and $\theta$ directions, respectively. The thickness of the tank is denoted by t, and the radius by a.

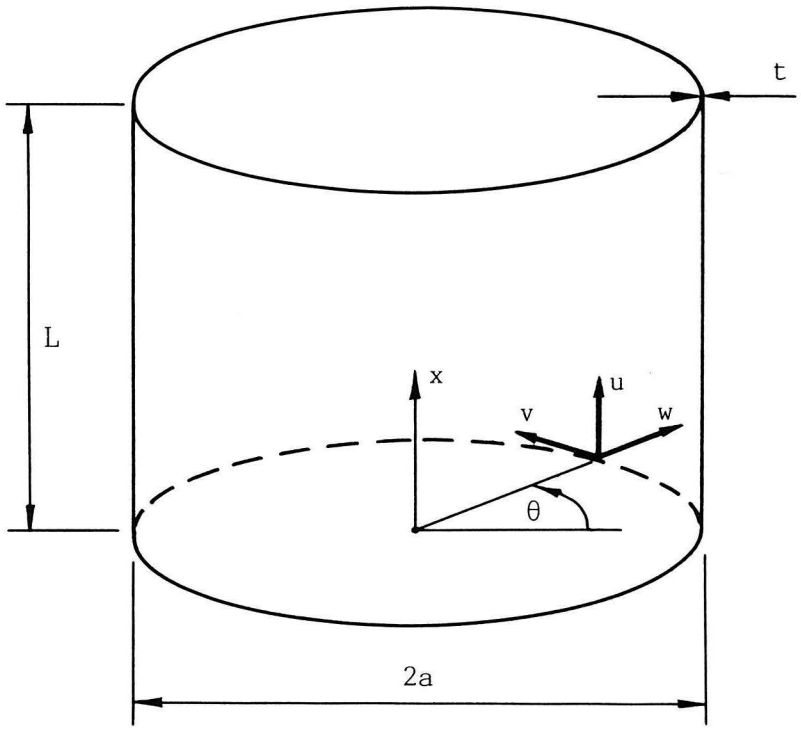


(a)

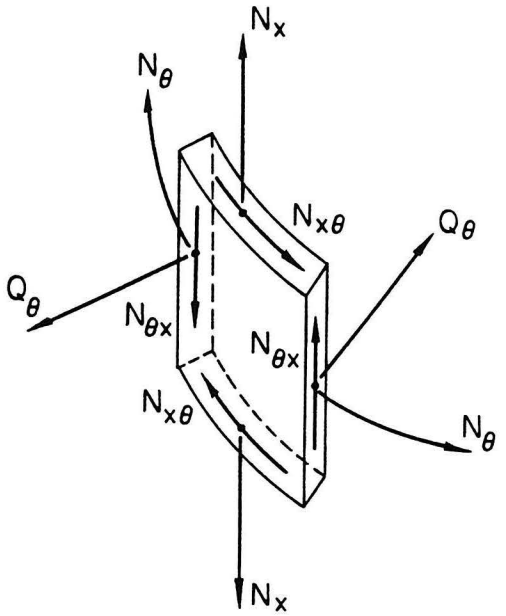


(b)

**Figure 3.1:** Dimensions, coordinate system, and stress resultants for the cylindrical shell.

## 3.2 COMMENTS ON THE SOLUTION FOR AN ANCHORED TANK

For an anchored tank, no inextensional modes are possible. This means that it is not possible to deform the shell without generating membrane strains. Smoothly varying loads from fluid pressure are carried mostly by membrane action with relatively little deformation of the shell. Except very close to the base, stresses and displacements can be accurately determined from the statically determinate membrane theory. Even close to the base, the solution can be obtained with good accuracy by superposing the solution from the membrane theory (which involves radial displacements at the base) upon an approximate solution for compensating imposed radial displacements at the base, which is discussed in the next section.

## 3.3 COMMENTS ON SOLUTION FOR IMPOSED RADIAL DISPLACEMENTS AND ROTATIONS AT THE BASE

The axisymmetric solution for a semi-infinite cylinder subjected to imposed radial displacements and rotations about the circumferential axis at the end (Timoshenko and Woinowsky-Krieger, 1959) is relatively simple, and has been used in Chapter 2 to formulate the boundary conditions for the axisymmetric analysis of the base plate. Solutions for imposed radial displacements and rotations that vary around the circumference are much more complicated. However, the author has shown that, as long as the variations in imposed displacements are slow in the sense that the change in imposed displacement over a length of $(at)^{1/2}$ is small, the axisymmetric solution, applied locally, is a good approxima-

tion to the much more complicated solution for imposed displacements which vary as functions of $\theta$. Furthermore, as the thickness to radius ratio, t/a, becomes very small, the error in the radial displacement and its derivatives up to the 4th order decrease like $(t/a)^{1/2}$. Since this result is not used extensively in what follows, the somewhat lengthy derivation is omitted. Instead, the range of validity of the approximation is verified numerically using the solution given by Flügge (1960) for a semi-infinite cylinder with loads applied at the base, $x = 0$. Suppose the radial displacement and rotation at the base are given by

$$\begin{bmatrix} w \\ \partial w/\partial x \end{bmatrix}_{x=0} = U_h \cos n\theta \quad ,$$

in which $U_h$ is a constant $2 \times 1$ vector. Then, from the solution for the non-axisymmetric problem, the applied shear force and moment at the base are

$$\begin{bmatrix} Q_x + \frac{1}{a}\frac{\partial M_{x\theta}}{\partial \theta} \\ M_x \end{bmatrix} = P_h \cos n\theta \quad ,$$

in which

$$P_h = K_{hn} U_h \quad ,$$

where $K_{hn}$ is a $2 \times 2$ matrix. If the axisymmetric solution is applicable locally, $K_{hn}$ must be independent of n. The ratio of the elements of $K_{hn}$ to the corresponding elements of $K_{ho}$ are shown in Fig. 3.2. For a given

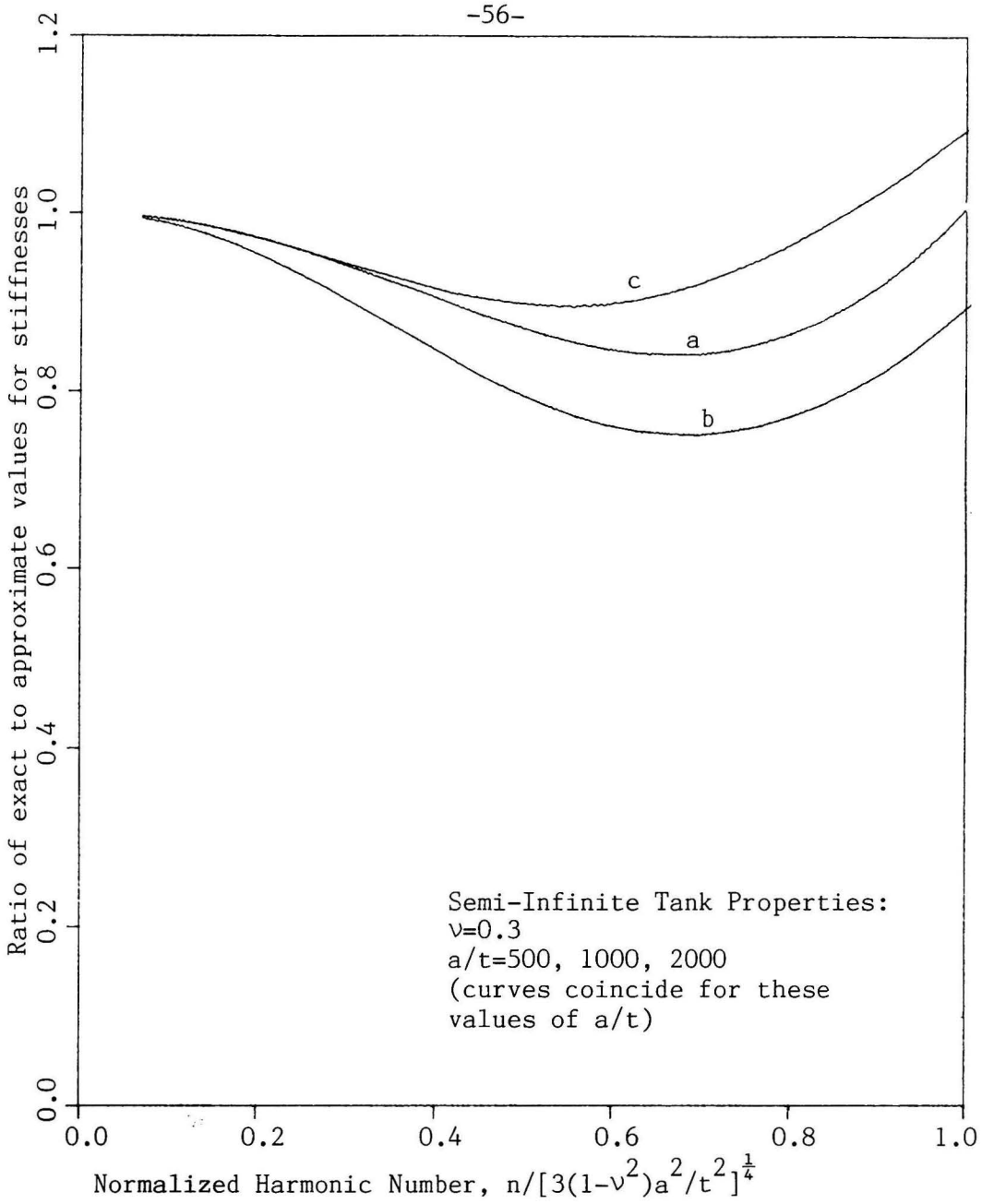


**Figure 3.2:** Solution for imposed radial displacement and rotation at the base: Ratio of the exact value to the approximate value from the axisymmetric solution for.

a) Radial force at base ($Q_x+M_{x\theta}/a$ at x=0) due to imposed radial displacement (w=1 at x=0)
b) Moment ($M_x$) at base due to imposed radial displacement, or radial force due to imposed rotation
c) Moment ($M_x$) due to imposed radial rotation (w'=1 at x=0).

value of Poisson's ratio, these ratios depend on the harmonic number n, and the radius to thickness ratio (a/t). However, in the shallow shell theory they depend only on a normalized harmonic number, $n/[3(1-\nu^2)a^2/t^2]^{1/4}$. Plotting the ratios obtained from the general (not necessarily shallow) shell theory as functions of this parameter, it was found that the curves for a/t = 500, 1000, and 2000 are indistinguishable. Hence, the shallow shell theory is seen to be essentially exact for a/t ratios typical of steel tanks. The error in applying the axisymmetric solution locally for values of the normalized harmonic number up to 1.0 is seen to be 20% at most. An important implication of this result is that if the circumferential displacement v of the edge of the base plate is negligible, then, in as far as the boundary conditions at the edge are concerned, the assumption of weak circumferential variations in the base plate is acceptable.

## 3.4 COMMENTS ON THE SOLUTION FOR IMPOSED VERTICAL DISPLACEMENTS AT THE BASE

Due to diaphragm action of the base plate, it is assumed that the horizontal displacements (radial and circumferential) at the base vanish. The rotation of the tank wall about the circumferential axis is assumed to be unrestrained and a vertical displacement U is imposed at the base. Thus the boundary conditions at the base are

$$u = U \, , \; v = w = 0 \, , \; M_x = 0 \quad \text{at} \quad x = 0 \; . \tag{3.1}$$

For a vertical displacement at the base,

$$U = \cos n\theta \quad , \tag{3.2}$$

the vertical force at the base is

$$P = \left[-N_x\right]_{x=0} = K_{vn} \cos n\theta \quad , \tag{3.3}$$

in which P, the vertical force at the base, is taken to be positive when it acts upwards. The sequence of stiffness coefficients, $K_{vn}$, defines the relation between vertical forces and displacements at the base. For n = 0, Eq. 3.2 defines an upward rigid body motion, for which $K_{vo} = 0$. For n = 1, the base undergoes a rigid body rotation about a horizontal axis $\theta = \pm \pi/2$. So $K_{v1} = 0$*. For $n \geq 2$ however, the tank is deformed and the stiffness coefficients are non-zero. It will be seen that for small n, the stiffness coefficients for a tank with a baseplate, but without a roof are of the order of $(a/t)^2$ times smaller than for the same tank with a roof. This radical difference arises because a tank without a roof can accommodate the displacement at the base without membrane strains.

### 3.4.1 Inextensional Deformation Modes of a Cylindrical Shell

For an inextensional cylindrical shell, the strains at the midsurface must vanish. Thus

---

* Except that when nonlinear effects discussed in Appendix B are included, $K_{v1}$ becomes negative.

$$u' = 0$$
$$u^{\cdot} + v' = 0 \qquad (3.4\ a\text{-}c)$$
$$v^{\cdot} + w = 0 \ ,$$

in which

$$(\ )' = a\frac{\partial}{\partial x}(\ ) \ , \quad (\ )^{\cdot} = \frac{\partial}{\partial \theta}(\ ) \ . \qquad (3.10)$$

The general solution to Eqs. 3.4 is

$$u = U$$
$$v = -(x/a)U^{\cdot} + V \qquad (3.5\ a\text{-}c)$$
$$w = (x/a)U^{\cdot\cdot} - V^{\cdot} \ ,$$

in which U and V are arbitrary functions of $\theta$ only.

If the horizontal displacements at the base are zero ($u = v = 0$ at $x = 0$), then $V = 0$. As a result, Eqs. 3.5 reduce to

$$u = U$$
$$v = -(x/a)U^{\cdot} \qquad (3.6\ a\text{-}c)$$
$$w = (x/a)U^{\cdot\cdot} \ .$$

Eqs. 3.6 represent the inextensional modes of an unanchored tank without a roof. For $U = \cos n\theta$, these become

$$u = \cos n\theta$$
$$v = n(x/a) \sin n\theta \qquad (3.7\ a\text{-}c)$$
$$w = -n^2(x/a) \cos n\theta \ .$$

A roof inhibits out-of-round displacements at $x = L$. It follows that only rigid body modes, but no inextensional deformation modes are possible. Hence, a tank with a roof cannot be deformed without

generating membrane strains.

### 3.4.2 Solution for a Tank With a Roof

For the analysis of the cylindrical shell the axisymmetric finite elements developed in Appendix B can be used. However, a compatible roof element needs to be added. For a typical roof consisting of a steel plate supported by trusses, the rigidity in the vertical direction is negligible. For the in-plane direction on the other hand, the rigidity due to the steel plate is large, but the effect of the trusses may be neglected. Hence, the stiffness matrix for a roof element can be derived by solving the plane stress problem for a disk with loads applied at the circumference. Timoshenko and Goodier (1970), p. 133 give a general expression for the Airy stress function for problems in polar coordinates. The solution of interest is obtained by selecting those terms which are not singular at r = 0. For the case in which the displacements at the circumference (r = a) are

$$\begin{aligned} w &= w_n \cos n\theta \\ v &= v_n \sin n\theta^* \quad , \end{aligned} \tag{3.8 a,b}$$

the radial and shear forces at circumference are

$$\begin{aligned} N_r &= N_{rn} \cos n\theta \\ N_{r\theta} &= N_{r\theta n} \sin n\theta^* \quad , \end{aligned} \tag{3.9 a,b}$$

---

* For the case n = 0, sin nθ is to be replaced by unity.

in which

$$\begin{bmatrix} N_{rn} \\ N_{r\theta n} \end{bmatrix} = K_{Rn} \begin{bmatrix} w_n \\ v_n \end{bmatrix} , \qquad (3.10)$$

where $K_{Rn}$, the in plane stiffness matrix for the roof, is given by

$$K_{Rn} = \begin{cases} \dfrac{E_R t_R}{a(1-\nu_R)} \begin{bmatrix} 1 & 0 \\ 0 & 0 \end{bmatrix} & \text{for} \quad n = 0 \\ \dfrac{E_R t_R}{a(3-\nu_R)} \begin{bmatrix} 1 & 1 \\ 1 & 1 \end{bmatrix} & \text{for} \quad n = 1 \\ \dfrac{E_R t_R}{a(1+\nu_R)(3-\nu_R)} \begin{bmatrix} 2n-(1-\nu) & 2-n(1-\nu) \\ 2-n(1-\nu) & 2n-(1-\nu) \end{bmatrix} & \text{for} \quad n \geq 2 \end{cases} , \qquad (3.11)$$

where $E_R$, $\nu_R$, $t_R$ are Young's modulus, Poisson's ratio and the thickness of the roof, respectively. The finite element analysis of the tank with a roof proceeds by adding this in-plane stiffness matrix of the roof into the approximate locations of the global stiffness matrix of the shell. The results for a typical tank are shown in Fig. 3.3 by square markers.

For comparison, consider the plane stress problem in a halfplane with loads applied at the edge. Let x be the coordinate direction normal to the boundary, such that x is positive in the halfplane, and let y be the coordinate tangential to the boundary. Let u and v be the displacements in the x and y direction, respectively. Specify the displacements at the edge as

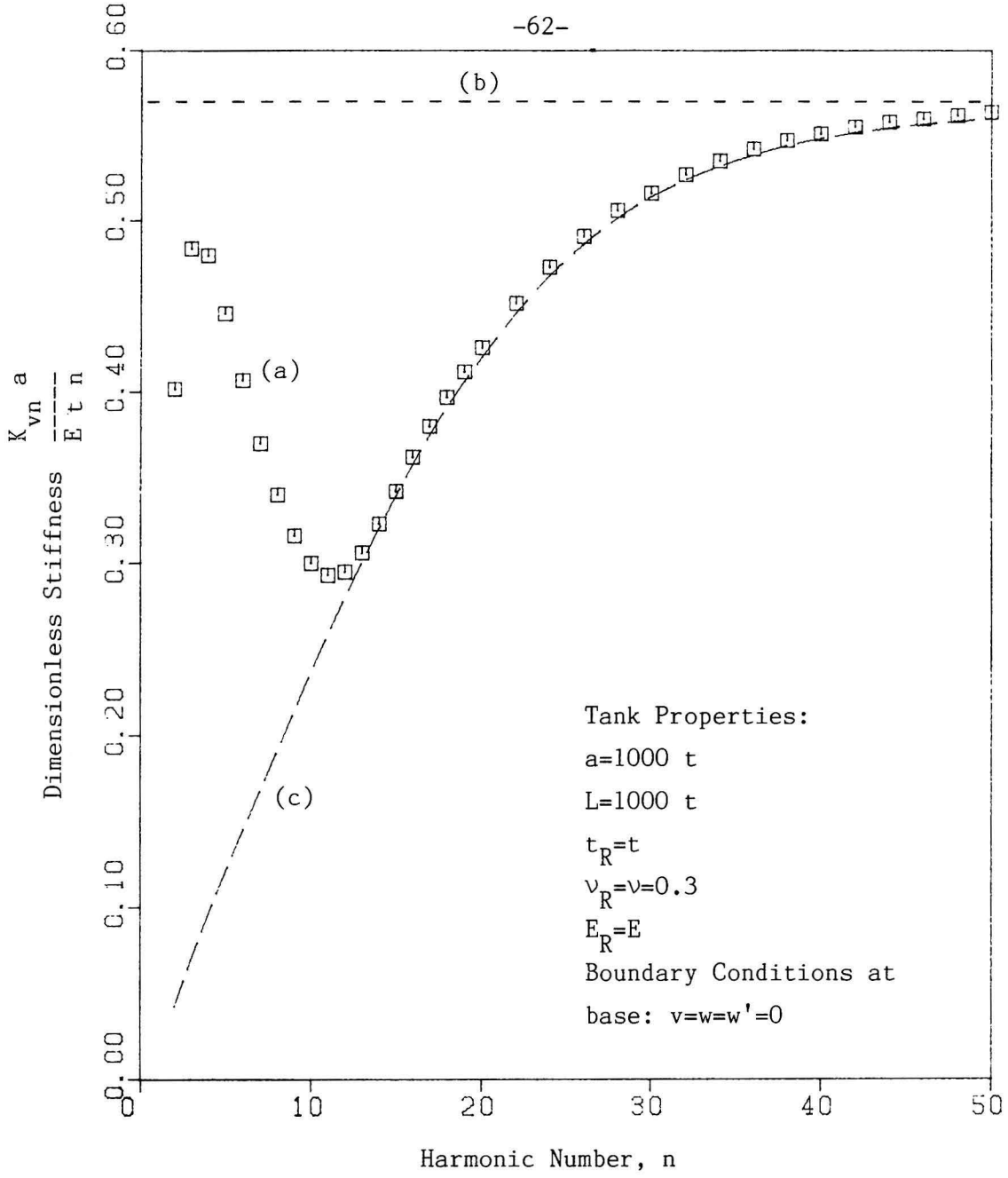


**Figure 3.3:** Stiffness for uplift u=cos nθ at base for

a) tank with roof (finite element solution)
b) semi-infinite plate (plane stress problem)
c) semi-infinite cylinder (analytical solution of Flügge, 1960)

$$u = \cos (ny/a)$$
$$v = 0 \quad .$$

Thus, the variation in u has the same wavelength as in the shell problem. As in Eq. 3.3, the normal force at the boundary can be written as

$$-\sigma_x t = K_{vn} \cos (ny/a) \quad .$$

From the solution of the plane stress problem*

$$K_{vn} = \frac{2Etn}{(3-\nu)(1+\nu)a} \quad .$$

This stiffness is shown in Fig. 3.3 as curve (b). As might be expected, for large n, the radius of curvature of the tank wall is small compared to the circumferential wavelength, and the stiffnesses for the tank and the halfplane coincide. More importantly, in this example, for any $n \geq 2$, the stiffness for the tank with a roof is no less than half the stiffness of the halfplane.

From the comparison of the tank with a roof to the semi-infinite cylinder, it is seen that the roof has more of a stiffening effect than a semi-infinite continuation of the cylinder. This occurs because the solution for a semi-infinite cylinder with a large ratio of a/t contains terms in the expressions for the stresses and displacements which decay very slowly in x (Flugge, 1960).

* The general solution to this problem is given by Timoshenko and Goodier (1970). The stresses and displacements decay like exp (-nx/a) or x exp (-nx/a).

### 3.4.3 Inextensional Solution for a Roofless Tank

When inextensional modes are possible, they are often so flexible compared to deformational modes involving membrane strains that the displacements associated with membrane strains become negligible compared to those associated with inextensional deformations. Under such conditions, the use of inextensional theory is in order.

Consider the determination of the vertical force that must be applied at the base to generate the displacements described by Eqs. 3.6: It can be obtained from the principle of virtual work by applying an inextensional virtual displacement. As a first step, the strains and stresses through the thickness of the shell need to be determined. For this purpose, substitute the inextensional displacement field (Eqs. 3.6) into what Flügge (1960) refers to as the exact* strain-displacement relations for a cylindrical shell, expand the resulting expressions in powers of the distance from the mid-surface, and neglect terms of second and higher order, to obtain

$$\varepsilon_x = 0$$

$$\varepsilon_\theta = -\frac{zx}{a^3}\left[ U^{(4)} + U^{(2)} \right] \qquad (3.12\ a\text{-}c)$$

$$\gamma_{x\theta} = -\frac{2z}{a^2}\left[ U^{(3)} + U^{(1)} \right] ,$$

in which $\varepsilon_x$ is the vertical strain, $\varepsilon_\theta$ the circumferential strain, $\gamma_{x\theta}$ the engineering shear strain, z is the distance from the mid-surface (positive so that a + z is the distance of the point from the axis of

---

* The expressions are exact for infinitesimal displacements.

the cylinder), and

$$U^{(n)} \equiv \frac{d^n U}{d\theta^n} \quad . \tag{3.13}$$

Now consider a virtual, inextensional deformation arising from a vertical virtual displacement $\delta U$ at the base, and the corresponding virtual displacements $\delta u$, $\delta v$ and $\delta w$, and virtual strains $\delta\varepsilon_x$, $\delta\varepsilon_\theta$ and $\delta\gamma_{x\theta}$ obtained by substituting $U = \delta U$ into Eqs. 3.6 and 3.12. Equating the virtual work done by the vertical force at the base, P, and loads $p_r$, $p_\theta$ and $p_x$ distributed over the surface of the cylinder to the virtual change in strain energy yields

$$\int_0^{2\pi} \left[ P\delta U + \int_0^L (p_x \delta u + p_r \delta w + p_\theta \delta v)\, dx \right] a\, d\theta$$

$$= \int_0^{2\pi} \int_0^L \int_{-t/2}^{t/2} \left[ \frac{E\varepsilon_\theta}{1-\nu^2}\, \delta\varepsilon_\theta + \frac{E\gamma_{x\theta}}{2(1+\nu)}\, \delta\gamma_{x\theta} \right] dz\, dx\, a\, d\theta \quad . \tag{3.14}$$

By substituting for the real and virtual strains from Eqs. 3.12, and for the virtual displacements from Eqs. 3.6, performing the integrations in x and z, and integrating by parts in $\theta$, Eq. 3.14 reduces to

$$\int_0^{2\pi} \left[ P + \int_0^L (p_x + \frac{x}{a}\, p_r^{\cdot\cdot} + \frac{x}{a}\, p_\theta^{\cdot}) dx \right] \delta U\, a\, d\theta$$

$$= K_s \int_0^{2\pi} \left[ U^{(8)} + (2-\alpha^2)U^{(6)} + (1-2\alpha^2)U^{(4)} - \alpha^2 U^{(2)} \right] \delta U\, a\, d\theta \quad , \tag{3.15}$$

where

$$K_s = \frac{Et^3L^4}{36(1-\nu^2)a^7} \tag{3.16}$$

$$\alpha = \left[6(1-\nu)\right]^{1/2} a/L \quad . \tag{3.17}$$

Finally, since $\delta U$ is arbitrary,

$$P + \int_0^L \left(\frac{x}{a} p_r'' + \frac{x}{a} p_\theta' + p_x\right)dx$$

$$= K_s\left[U^{(8)} + (2-\alpha^2)U^{(6)} + (1-2\alpha^2)U^{(4)} - \alpha^2 U^{(2)}\right] \quad . \tag{3.18}$$

The corresponding stiffness coefficient for $U = \cos n\theta$ is

$$K_{vn} = \frac{Et^3L^4(n^2+\alpha^2)(n^2-1)^2 n^2}{36(1-\nu^2)a^7} \quad . \tag{3.19}$$

Comparing this expression to the stiffnesses for the tank with a roof, it is seen that for small n these inextensional modes are of the order of $(a/t)^2$ times more flexible. Under such conditions, the inextensional theory is a good approximation. However, the stiffness of the inextensional modes increases like $n^8$, and for

$$n = [6a/t]^{1/4} \quad , \tag{3.20}$$

the flexibility due to inextensional modes is of the same order as that for deformations involving membrane strains. This phenomenon is illustrated in Fig. 3.4.

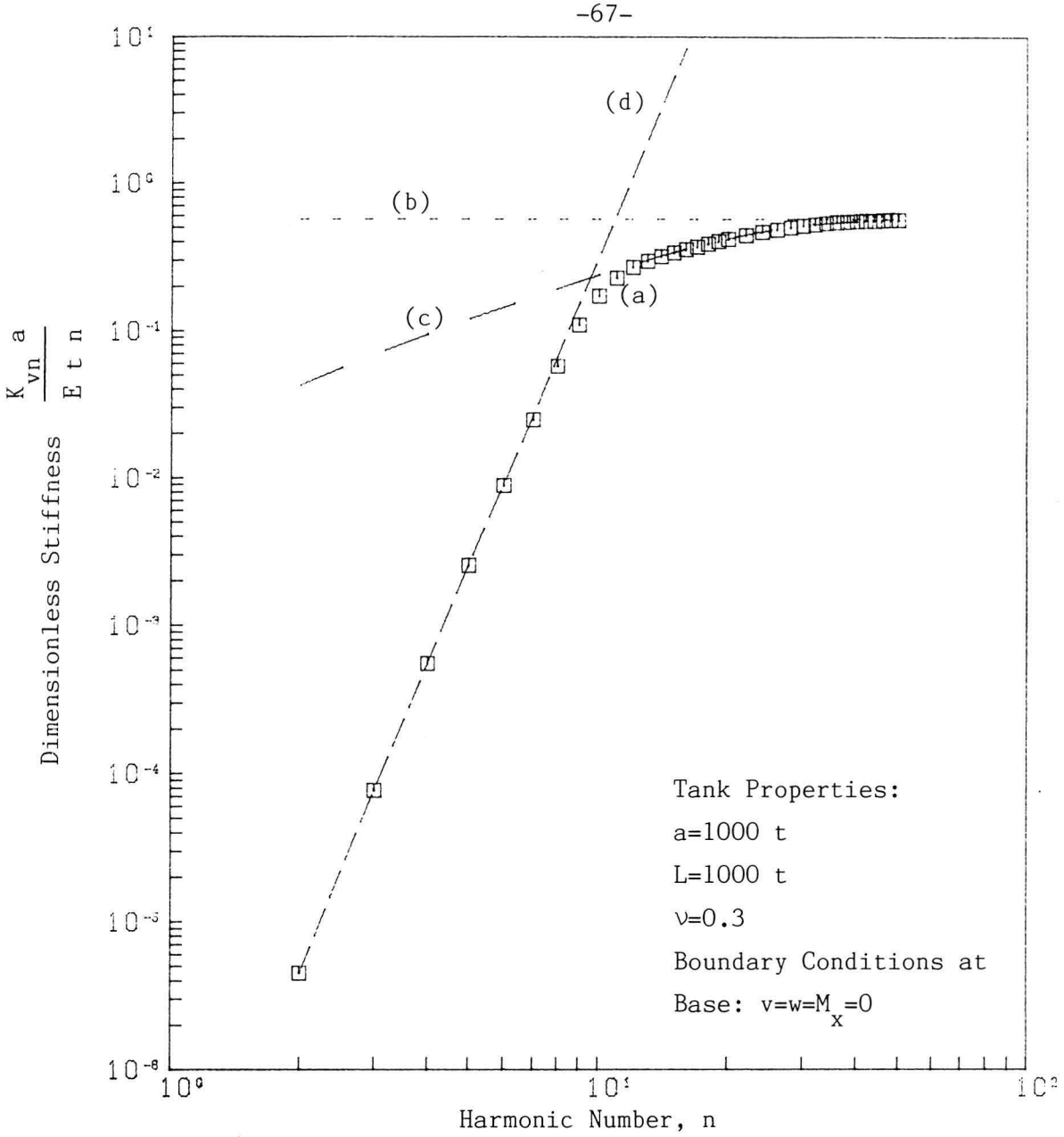


**Figure 3.4:** Stiffness for uplift u=cos n at base for

a) tank with no roof (finite element solution)
b) semi-infinite plate (plane stress problem)
c) semi-infinite cylinder (analytical solution of Flügge, 1960)
d) inextensional tank with no roof

## 3.5 CONCLUSIONS

The main purpose of this chapter is not to present techniques for the analysis of the shell. That is done in Appendix B. Rather, it is to review some relevant elementary solutions in order to help the reader interpret and evaluate the results of the following chapters.

The principal conclusions drawn from the results presented are:

1. If the circumferential displacement v at the junction between the base plate and the shell is negligible, then in as far as the determination of the radial force and moment exerted by the shell on the base plate is concerned, the assumption of weak circumferential variations in the base plate is acceptable.
2. For an unanchored tank without a roof, very flexible inextensional deformational modes exist, which involve out of round deformations of the shell. These displacements increase proportionally with the distance from the base. A roof prevents such inextensional modes, and is therefore expected to have an important effect on the behavior of unanchored tanks.
3. Although for some loading and boundary conditions, the behavior of a cylindrical shell is well described by the analytical approximations of this chapter; for an uplifting tank, the behavior is sufficiently complicated to require the use of numerical methods, such as the finite element method.

The formulation for axisymmetric elements used for this purpose, including a first order approximation for geometrically nonlinear effects, is given in Appendix B.

## 4. ANALYSIS OF A SHELL ON A BED OF VERTICAL NONLINEAR SPRINGS

In Chapter 2 the variations in the circumferential direction were said to be weak if the conditions in the baseplate at any circumferential location, $\theta$, were fully determined by the vertical uplift of the edge at the same location, and did not depend on the vertical uplift of the edge at other locations. If this is the case, and furthermore the foundation can be represented by Winkler springs, then the unanchored tank subjected to lateral loads can be modeled by considering the shell (and roof if present) to be mounted on a circular bed of vertical, nonlinear springs. The force per unit length-deflection relationship for these nonlinear springs in tension is determined from the axisymmetric uplift solution, and in compression from the properties of the foundation.

In addition to the vertical boundary condition at the base of the shell, the conditions for radial and circumferential displacements and for rotation about the circumferential axis need to be described. If the assumption of weak circumferential variations is followed strictly, the radial force and the moment at any location are determined from the axisymmetric solution by the vertical displacement at the same location. In the circumferential direction, the stiffness of the base plate acting as a diaphragm is large compared to the corresponding stiffness of the shell. Hence, circumferential displacements at the base are small and may reasonably be assumed to vanish.

Simpler boundary conditions for radial displacement and rotation are possible if interaction effects are small. In this case the vertical force is hardly affected by the non-vertical displacements, and the boundary conditions for radial displacement and rotation have little bearing on the solution for vertical displacements. Since the base plate offers a relatively large resistance to horizontal (radial and circumferential) displacements, and a relatively small resistance to rotations about the circumferential axis, it is assumed here that horizontal displacements of the shell wall vanish at the base, and that rotations about the circumferential axis are unrestrained. This assumption is made only for the purpose of defining the relationship between uplift and vertical forces acting on the shell at the base.

The formulation and solution for a tank on a circular bed of nonlinear Winkler springs will be given in Section 4.1 for a limiting case for which an analytical solution is possible, and in Section 4.2 for a more general case. Definitions given in Chapter 3 also apply here and are not repeated.

## 4.1 ANALYTICAL SOLUTION FOR A LIMITING CASE

For an inextensional shell without a roof, Eq. 3.18 gives rise to the possibility of solving contact problems analytically. Consider the case in which the foundation is perfectly rigid in compression, and any uplift causes a tensile force $N_x = N_0$ at the base.* Thus,

* This is the assumption made by Wozniak and Mitchell (1978) in what has become part of the design standard of the American Water Works Association (1979).

$$P = -N_0 \quad , \quad U \geq 0 \qquad \text{for} \quad \theta \in R_1$$
$$P \geq -N_0 \quad , \quad U = 0 \qquad \text{for} \quad \theta \in R_2 \quad , \tag{4.1 a,b}$$

where $R_1$ is the uplifted region and $R_2$ is the region in contact with the base. Since the foundation is rigid, P need not be finite in $R_2$. It may contain Dirac delta function singularities corresponding to vertically upward point reactions. However, dipoles and higher order singularities are not permitted, because they involve tensile as well as compressive forces. Such tensile force cannot be generated (Eqs. 4.1). With reference to Eq. 3.18 it is seen that this means that $U^{(7)}$ may be discontinuous, but all lower derivations must be continuous everywhere.

Suppose now the contact region, $R_2$, has some finite extent. Then U and all its derivatives vanish in $R_2$. Since the first six derivatives of U must be continuous, this means that the boundary conditions for the solution in the uplifted region $R_1$ are

$$U^{(n)} = 0 \qquad \text{for} \quad n = 0,1,\ldots,6 \quad , \tag{4.2}$$

at the boundary between regions $R_1$ and $R_2$. Thus, for the solution in region $R_1$, there are 7 boundary conditions at each of 2 boundaries, a total of 14 conditions. These are more boundary conditions than can, in general, be accommodated by the solution of an 8th order differential equation. As a result, it appears to be impossible to obtain a solution in which the contact region has a finite extent.

A more fruitful approach is to seek solutions in which the contact region $R_2$ consists of one or more discrete contact points. While the solution of such problems may be of some theoretical interest, their

practical value is limited because the membrane deformations due to point reactions in the vicinity of the contact points cannot be neglected. On the other hand, away from the contact points, the effect of local membrane strains associated with the point reactions may well be small.

Here only the simplest contact problem is considered, the case in which there is a single contact point. Since there can be no moment applied at a contact point, this means that loads applied to the tank must be such that the tank is just at the point of overturning.

Let the distributed loads due to lateral fluid pressure and the weight of the tank wall be

$$\begin{aligned} p_r &= -f(x)\cos\theta \\ p_\theta &= 0 \\ p_x &= -\gamma_t t \end{aligned} \qquad (4.3\ a\text{-}c)$$

in which $\gamma_t$ is the unit weight of the tank wall material. Substituting Eqs. 4.1a and 4.3 into Eq. 3.18, and factorizing the differential expression in U gives

$$K_s\left(\frac{d^2}{d\theta^2} - \alpha^2\right)\left(\frac{d^2}{d\theta^2} + 1\right)^2 \frac{d^2U}{d\theta^2} = -F_0 + F_1 \cos\theta \quad , \qquad (4.4)$$

in which $F_0 = \gamma_t tL + N_0$, and $F_1 = \int_0^L \frac{x}{a} f(x)dx$ is proportional to the overturning moment due to lateral fluid pressure on the tank wall.

The general solution to Eq. 4.4 which is symmetric in $\theta$ is

$$U = \frac{F_0}{K_s}\left[\frac{\theta^2}{2\alpha^2} - \frac{(F_1/F_0)\theta^2 \cos\theta}{8(1+\alpha^2)}\right] + C_1 + C_2 \cos\theta + C_3\,\theta \sin\theta + C_4 \cosh(\alpha\theta) \quad , \tag{4.5}$$

in which $C_i$ are arbitrary constants to be determined from the boundary conditions. The simplest case occurs when $F_1$ is such that the tank is at the point of overturning. This happens when

$$F_1 = 2F_0 \quad . \tag{4.6}$$

Under such conditions overall equilibrium can only be satisfied if there is a single contact point at $\theta = \pm\pi$. The boundary conditions at this point are

$$\begin{aligned} U^{(n)}(\pi) &= U^{(n)}(-\pi) = 0 \qquad \text{for } n = 0,1 \\ U^{(n)}(\pi) &= U^{(n)}(-\pi) \qquad \text{for } n = 2,3,\ldots,6 \quad . \end{aligned} \tag{4.7 a,b}$$

Since U is symmetric in $\theta$, all even derivatives are also symmetric in $\theta$, and therefore satisfy the continuity conditions at $\theta = \pm\pi$. However, the odd derivatives are antisymmetric and must therefore vanish at $\theta = \pm\pi$. Hence the boundary conditions reduce to

$$U^{(n)}(\pi) = 0 \qquad \text{for} \quad n = 0,1,3,5 \quad . \tag{4.8}$$

Eqs. 4.8 are four conditions for the four arbitrary constants $C_1$ to $C_4$. However, the solution is not unique. This can be expected because the tank is free to rotate about the contact point. For positive

displacements in the vicinity of the contact point, $U^{(2)}(\pi)$ must be non-negative. A limiting case occurs when

$$U^{(2)}(\pi) = 0 \quad . \tag{4.9}$$

Using this condition in addition to Eqs. 4.8 leads to a unique solution for the constants $C_1$ to $C_4$. The resulting expression for U is

$$\frac{UK_s}{F_0} = \frac{\theta^2-\pi^2}{2\,\alpha^2} - \frac{\theta^2 \cos\theta + \pi^2}{4(1+\alpha^2)} + \frac{5+3\alpha^2}{2(1+\alpha^2)^2}\,\theta \sin\theta$$

$$- \frac{\pi[\cosh(\alpha\theta) - \cosh(\alpha\pi)]}{\alpha^3(1+\alpha^2)^2 \sinh(\alpha\pi)}$$

$$- \left[\frac{1}{\alpha^2} - \frac{(\pi^2-2)}{4(1+\alpha^2)} - \frac{5+3\alpha^2}{(1+\alpha^2)^2} - \frac{\pi \cosh(\alpha\pi)}{\alpha(1+\alpha^2)^2 \sinh(\alpha\pi)}\right](1+\cos\theta) \quad . \tag{4.10}$$

By differentiating this expression according to Eqs. 3.6, the radial and tangential displacements are obtained. At any given location, the result can be expressed in the form

$$\frac{\delta}{a} = \frac{F_0}{Et}\left(\frac{a}{t}\right)^2 f\left(\frac{L}{a}, \nu\right) \quad , \tag{4.11}$$

in which $\delta$ stands for a displacement, and $f(.,.)$ is a dimensionless function. The resulting deformed shape is shown in Figs. 4.1 and 4.2 for L/a = 1 and 2, respectively.

As a numerical example, for a typical tank of radius a = 30 ft, height L= 30 ft, thickness t = 0.25 in, made of steel ($E = 30 \times 10^6$ psi, $\nu = 0.3$, $\gamma_t = 0.28$ lb/in$^3$) with no tensile force

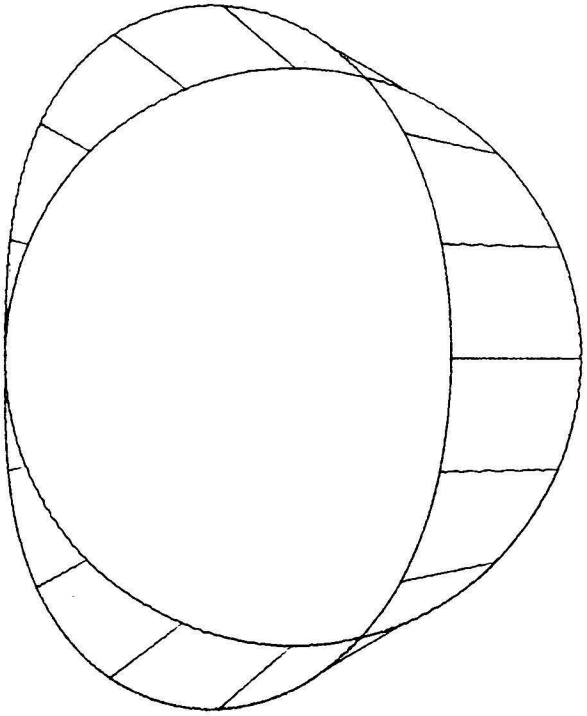

PLAN

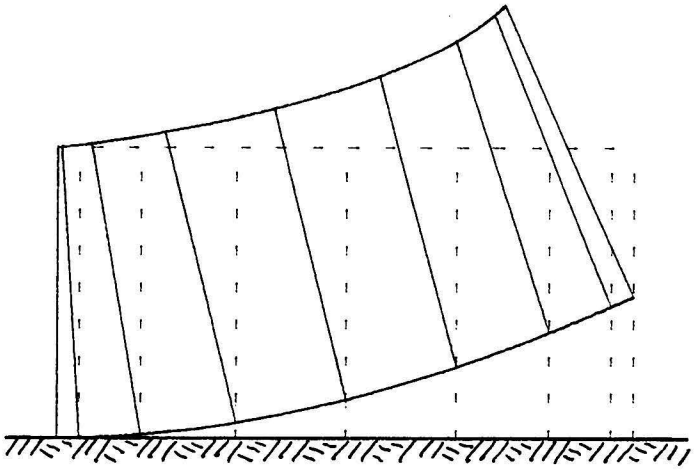

ELEVATION

**Figure 4.1:** Deformed shape of an unanchored, roofless, inextensional tank subjected to lateral loads. $L/a=1$, $F_o a^2/(E t^3)=0.25$, $\nu=0.3$

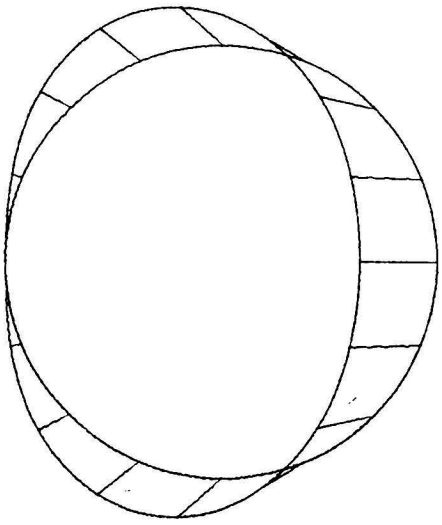

PLAN

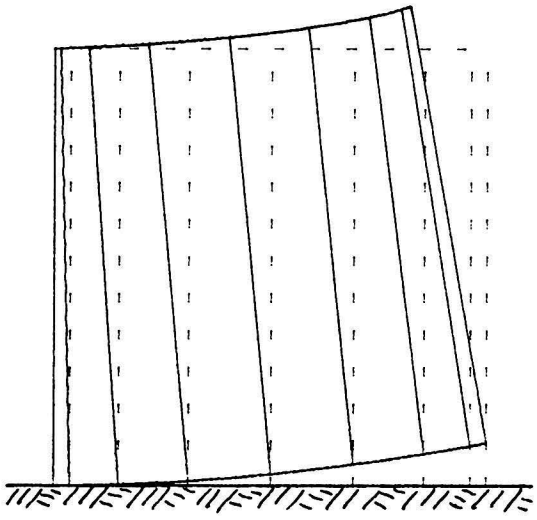

ELEVATION

**Figure 4.2:** Deformed shape of an unanchored, roofless, inextensional tank subjected to lateral loads
$L/a=2$, $F_o\, a^2/(E\, t^3)=1.0$, $\nu=0.3$

generated at the base ($N_0 = 0$), the scale factor for the deformed shape is

$$F_0 \, a^2/Et^3 = 7.0 \quad .$$

This means that the deformations would be 28 times larger than those shown in Fig. 4.1. For $N_0 > 0$, the deformations increase even more. In reality such large deformations do not occur because

1. Geometrically nonlinear effects become dominant;
2. Lateral loads change with a period which is short compared with the time it would take for the computed deformations to develop;
3. The tensile force developed at the base is not independent of the amount of uplift, but increases with increasing uplift. This tends to prevent very large amounts of uplift. In fact, for a roofless tank with no bending rigidity at all, and disregarding effects 1 and 2, the distribution of vertical stresses at the base, as determined from the solution of the shell problem, does not depend on the distribution of uplift around the circumference, and must therefore be the same as for an anchored tank. Under such conditions the distribution of vertical stresses at the base for an unanchored tank is the same as for the anchored tank. Furthermore, uplift at any location on the circumference can be determined directly from the force-deflection relation for the foundation.

4. Roofless tanks are required to have a stiffening rim or wind girder at the top, which tends to reduce the out-of-round deformations.

While the solution for an inextensional tank without a roof provides some insight into the behavior of the cylindrical shell under conditions of seismic uplift, it also points to the need for a more general method of analysis, one that includes the effects of membrane strains, a more general force-uplift relationship at the base, and the tendency of the hydrostatic internal fluid pressure to prevent out of round deformations of the shell.

## 4.2 NUMERICAL SOLUTION FOR THE GENERAL CASE

In this section, a numerical solution for the problem of the shell on a circular bed of nonlinear Winkler springs is given. The Winkler springs represent the restraining action of the foundation and the baseplate. It is assumed that the stiffness of the foundation is finite. As a result, finite displacements at the base imply finite forces, and no singularities in the solution are expected. Under such conditions, numerical solutions by Gallerkin's method can be expected to converge to the correct solution.

### 4.2.1 Formulation

Consider the cylindrical shell, loaded, with or without a roof, with boundary conditions at the base given by $u = U$, $v = w = 0$, $M_x = 0$. Suppose the imposed displacement, U, is expressed as a cosine series in

the form

$$U = \sum_{n=0}^{N} U_n \cos n\theta \quad . \tag{4.12}$$

Then, using the axisymmetric finite elements described in Appendix B, the vertical force at the base can be obtained in the form

$$P = \sum_{n=0}^{N} P_n \cos n\theta \quad , \tag{4.13}$$

where P, the vertical force acting on the shell at the base, is taken to be positive when it acts upwards, and

$$P_n = F_n + K_{vn} U_n \quad . \tag{4.14}$$

In Eq. 4.14, $F_n$ are the Fourier components of the reaction at the base that would be present if the displacements at the base were zero all around the circumference, and as in Eq. 3.3, $K_{vn}$ are the vertical stiffness coefficients of the shell.

At any point, the force acting on the circular bed of Winkler springs is equal in magnitude and opposite in direction to that acting on the shell. Thus, the equation for the springs is

$$-P = f(U) \quad , \tag{4.15}$$

where f(U) is the vertical force per unit length (positive upwards) acting on the Winkler springs. For positive U, i.e., an upward deflection, f(U) is determined from the axisymmetric solution for the base plate given in Chapter 2. For negative U, f(U) is given from the properties

of the foundation. For the present formulation f(U) is assumed to be a known, nonlinear function. Substituting Eq. 4.14 into Eq. 4.13 and using the resulting expression for P along with Eq. 4.12 in Eq. 4.15 gives

$$\sum_{n=0}^{N} (F_n + K_{vn}U_n) \cos n\theta + f\left( \sum_{n=0}^{N} U_n \cos n\theta \right) = 0 \quad . \qquad (4.16)$$

Following Galerkin's method, multiply Eq. 4.16 by cos $m\theta$, $m = 0,1,2,\ldots,N$, and integrate around the circumference to obtain

$$\pi\delta_m(F_m + K_{vm}U_m) + \int_0^{2\pi} f\left( \sum_{n=0}^{N} U_n \cos n\theta \right) \cos m\theta \, d\theta = 0 \quad , \qquad (4.17)$$

in which

$$\begin{aligned} \delta_m &= 2 \qquad \text{for} \qquad m = 0 \\ &= 1 \qquad \text{otherwise} \quad . \end{aligned} \qquad (4.18)$$

The integral in Eq. 4.17 needs to be evaluated numerically. To avoid locking of the problem, it is judged advantageous to make the number of integration points equal to the number of Fourier harmonics used, N. Physically, this is equivalent to replacing the continuous circle of Winkler springs by discrete springs at locations $\theta = i\pi/N$; $i = 0,1,\ldots,2N-1$. Thus Eq. 4.17 becomes

$$K_{vm}\delta_m U_m + \frac{2}{N} \sum_{i=0}^{N} \gamma_i \, f\left( \sum_{n=0}^{N} U_n \cos \frac{ni\pi}{N} \right) \cos \frac{mi\pi}{N} = -F_m\delta_m \quad , \qquad (4.19)$$

where

$$\gamma_i = \frac{1}{2} \quad \text{for} \quad i = \ldots -2N,-N,0,N,2N, \ldots$$
$$= 1 \quad \text{otherwise} , \tag{4.20}$$

are weighting factors which arise because the points at $\theta = 0,\pi$ only occur once, whereas other points occur at each side of the circumference.

Equations 4.19 for $m = 0,1,2,\ldots N$ are $N + 1$ coupled nonlinear equations for the unknown Fourier components of the displacements $U_0$, $U_1,\ldots,U_N$. They can be solved numerically. However, in many practical cases, the stiffness of the foundation in compression is very high compared with other stiffnesses. As a result, the displacements at points that remain in contact with the foundation are very small. Computing these displacements by summing Fourier components which are not small in absolute value is potentially an illconditioned calculation. Difficulties can be avoided by the following transformation of variables. Denote the displacement at $\theta = j\pi/N$ by $U^j$. Thus,

$$U^j = \sum_{n=0}^{N} U_n \cos(nj\pi/N) \quad . \tag{4.21}$$

From Appendix C, Eq. C8, the inverse relation as derived from the theory of discrete Fourier transforms is

$$U_n = \frac{2\gamma_n}{N} \sum_{j=0}^{N} \gamma_j U^j \cos(nj\pi/N) \quad . \tag{4.22}$$

Thus Eq. 4.19 can be rewritten in terms of what might be termed the nodal displacements $U^j$ as follows:

$$K_{vm}\delta_m \frac{2\gamma_m}{N} \sum_{j=0}^{N} \gamma_j U^j \cos(mj\pi/N)$$

$$+ \frac{2}{N} \sum_{j=0}^{N} \gamma_j f(U^j) \cos(mj\pi/N) = -F_m\delta_m \quad . \tag{4.23}$$

Finally, multiplying Eq. 4.23 by $(2/N)\gamma_m\gamma_i \cos(mi\pi/N)$, summing for $m = 0,1...N$, and making use of the discrete orthogonality relation given in Eq. C6 of Appendix C yields

$$\sum_{j=0}^{N} S_{ij}U^j + \frac{2\gamma_i}{N} f(U^i) = -\bar{F}^i \quad , \tag{4.24}$$

in which

$$S_{ij} = \left(\frac{2}{N}\right)^2 \gamma_i\gamma_j \sum_{m=0}^{N} K_{vm}\delta_m\gamma_m^2 \cos(mi\pi/N) \cos(mj\pi/N) \tag{4.25}$$

$$\bar{F}^i = \frac{2\gamma_i}{N} \sum_{m=0}^{N} \gamma_m\delta_m F_m \cos(mi\pi/N) \quad . \tag{4.26}$$

Equation 4.24 can be solved numerically by Newton's method with the advantages that the matrix of coefficients $S_{ij}$ is symmetric, and only the diagonal terms of the Jacobian or tangent matrix change at each iteration.

### 4.2.2 Implementation

If the number of Fourier harmonics, N, is large, a large number of Newton iterations and/or loading steps are required to obtain a converged solution at load levels that are typical for earthquake resistant design. In addition, the computational effort for each

iteration increases like $N^3$. To reduce the effort for large N, the program was implemented with the capability to restart the analysis with a larger value of N. To achieve this, the nodal displacements $U^j$ can be interpolated as follows: Suppose N1 is the value of N for the first run, and N2 $\geq$ N1 is the value of N for the restart. Then the nodal displacements for the restart can be obtained from

$$U^j = \sum_{n=0}^{N1} U_n \cos(nj\pi/N2) \quad ; \quad j = 0,1,\ldots,N2 \quad , \qquad (4.27)$$

in which $U_n$ are the Fourier amplitudes for the displacements at the last load step of the first run, as obtained from Eq. 4.22 with N = N1.

With the restart capability, the user of the program can start with a small value of N, increase the loads to the desired level in several loadsteps, and restart at the desired load level with a larger value of N. In this case convergence to a more accurate solution occurs in only a few iterations. It is then possible to restart the program with an even larger value of N. Thus a high degree of accuracy can be achieved with a much reduced amount of computational effort.

### 4.2.3 Results

The analysis is performed for two tanks for which experimental results from tilt tests by Clough and Niwa (1979), and Manos and Clough (1982) are available. These will be dealt with in sections 4.2.3.1 and 4.2.3.2 respectively. Most of the discussion of the results is reserved for Chapter 5, where the same tanks will be reanalyzed by a more

comprehensive method.

4.2.3.1 Tall Tank Tested by Clough and Niwa (1979)

Design details for this 15 ft tall, 7 ft-9 in diameter aluminum tank are shown in Figure 4.3. The shell is fabricated out of three 5 ft courses, the lower two being 0.090 in thick, and the third 0.063 in thick. For the present analysis, it is modeled with 35 axisymmetric elements of lengths varying between 2 in near the base and top, and 8 in at midheight. Nonlinear effects due to the internal hydrostatic pressure described in Appendix B are included. The wind girder (stiffening ring at the top rim) is modeled as a 2 in long thickened shell element, assuming perfect bonding between the stiffening elements and the shell, plus a 1-1/16 in $\times$ 3/16 in rectangular ring element at the appropriate radial eccentricity to model the horizontal leg of the angle which forms the outer part of the stiffening rim. The 4 $\times$ 4 stiffness matrix for such a ring stiffener is given in Lee and Nash (1982), and restated in Appendix D. The ring stiffener is attached to the top node of the finite element model of the shell with zero vertical eccentricity. Although in reality, the centroid of the stiffener is 3/32 in below the top node of the finite element model, the assumption of zero vertical eccentricity makes it possible to use the readily available results from Lee and Nash (1982) and is expected to be a good approximation.

The roof consists of a flat, 1/16 in thick aluminum plate, stiffened by two angle sections. The contribution to the stiffness matrix from the flat plate is calculated from Eqs. 3.11. This stiffness

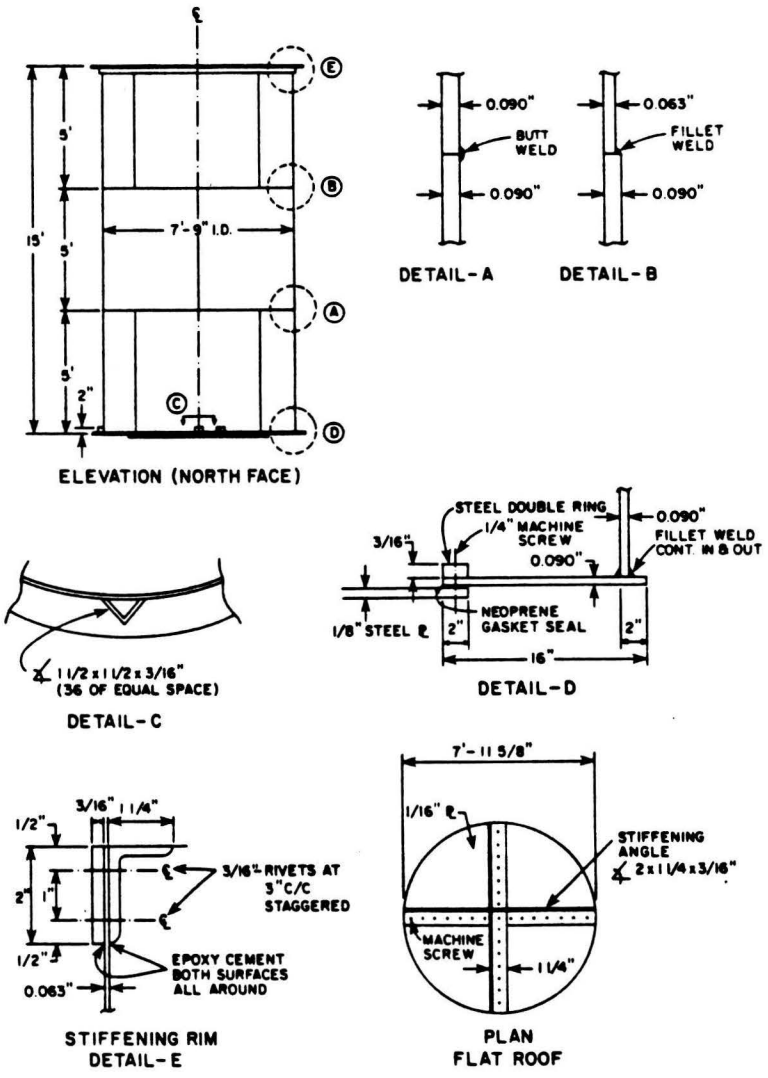


**Figure 4.3:** Design details of the tall aluminum tank tested by Clough and Niwa (1979). (Reproduced from their report with the authors' permission)

alone is sufficient to suppress any out-of-round displacements at the top. Therefore, neglecting the in-plane stiffness of the angles hardly affects the stresses and displacements in the shell.

For the axisymmetric analysis of the base plate, it is assumed that the entire base plate consists of one continuous sheet of 0.09 in thick aluminum. In reality, the inner part of the base plate consists of a 1/8 in thick steel plate and is therefore stiffer, but this is offset by the flexible joint between the 1/8 in thick steel plate and the 0.09 in aluminum sheet (Detail-D in Fig. 4.3). The 2 in overlap of the base plate beyond the shell wall is included as a ring with only an axial stiffness provided by 0.18 sq. in of aluminum. The fluid pressure acting on the base plate is calculated for zero tilt and assumed to be constant.

The properties of aluminum are taken to be $E = 10 \times 10^6$ psi for Young's modulus, and $\nu = 0.25$ for Poisson's ratio. The yield stress of the aluminum is taken to be sufficiently high to prevent formation of a plastic hinge at the junction between the tank wall and the base plate. To verify the sensitivity of the results to the last assumption, the axisymmetric analysis was repeated for a plastic moment capacity of 60.75 in-lb/lb corresponding to a yield strength of 30 ksi. Even for large uplift, when some hinge rotation occurs, the uplift force is not sensitive to such rotations.

The force per unit length-deflection relation, F(U), for the Winkler springs, for positive U, as obtained from the axisymmetric analysis, is shown in Fig. 4.4. Linear interpolation is used for values

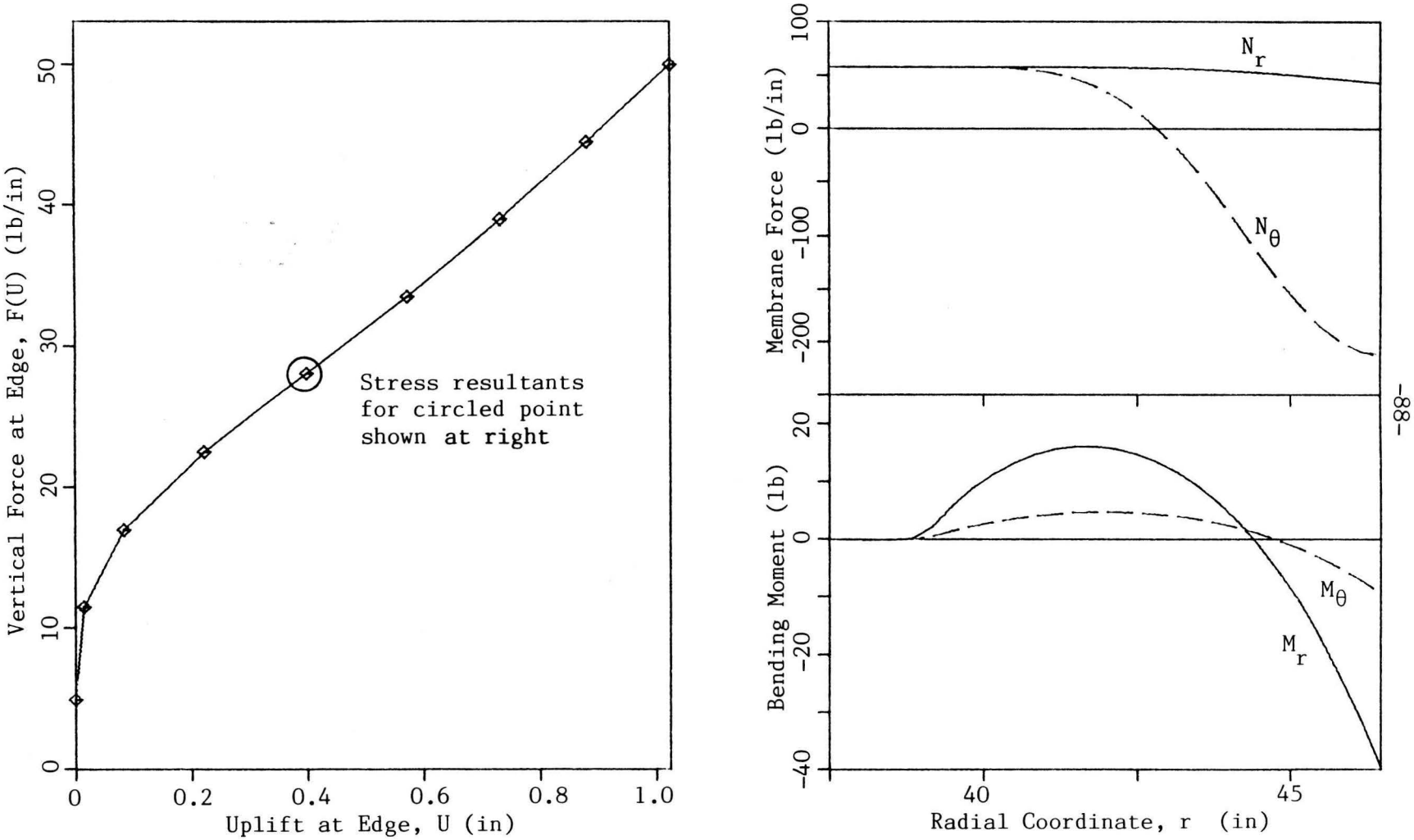


**Figure 4.4:** Results from the axisymmetric uplift analysis of the tall aluminum tank tested by Clough and Niwa (1979), [13ft water depth, no yielding and continuous base plate of constant thickness assumed]

between the points shown in Fig. 4.4. For negative U, compressive forces, the Winkler springs are taken to be linear with a stiffness of $4.7 \times 10^{10}$ lb/in$^2$. This high stiffness simulates a rigid foundation.

In applying the loads from fluid pressure to the shell, special care had to be taken in the vicinity of the free surface, where the fluid pressure only acts over part of the circumference of the shell. At such locations, the fluid pressure on the wetted part of the circumference can be expressed as a cosine series containing only two terms, one of order zero and one of order one. However, on the dry part of the circumference, the same expression is not valid since the pressure is zero. For the purpose of applying the loads, the pressure at every elevation must be expressed as a cosine series which is valid on the entire circumference. Where the circumference is partially wetted such a cosine series contains infinitely many terms. Expressions for the coefficients are given in Appendix E.

The analysis is performed for a 13 ft water depth, a tilt angle of $6.45^{\circ}$, and with and without the enclosing roof.

Convergence of the numerical method is studied in Figs. 4.5 and 4.6. The maximum uplift is seen to converge very rapidly. Although in Fig. 4.5 convergence is from below, this is not necessarily the case. The maximum vertical compressive force at the base converges somewhat slower, because for N = 2 and 5, contact with the foundation occurs at only one of the discrete Winkler springs. When this is the case, the force in the one Winkler spring that is in compression may well be a good approximation to the total compressive force transmitted from the

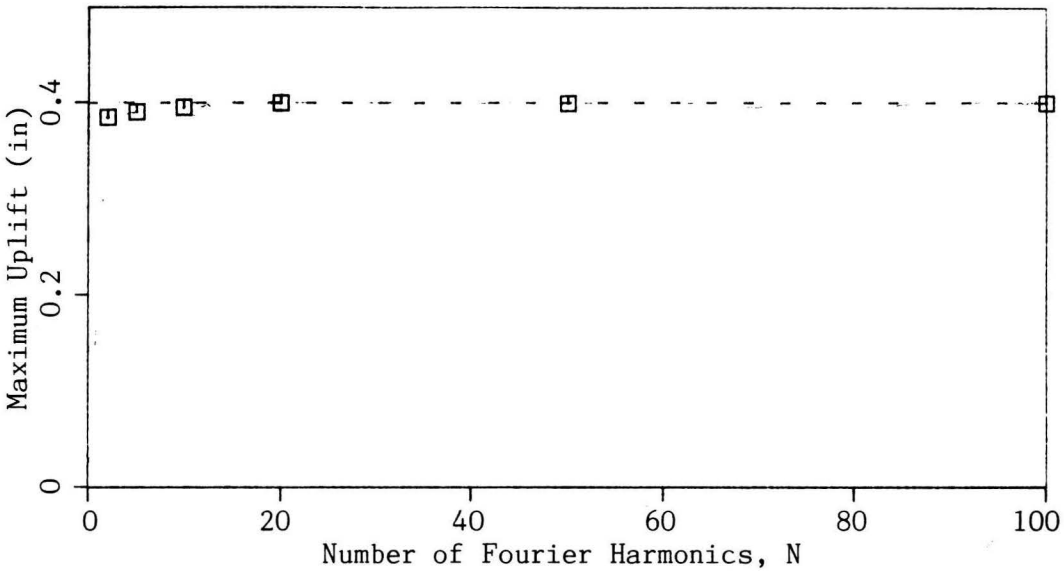


**Figure 4.5:** Convergence of maximum uplift for the tank tested by Clough and Niwa (1979). N=2,5,10,50,100. [13ft water, tilt=6.45°, closed]

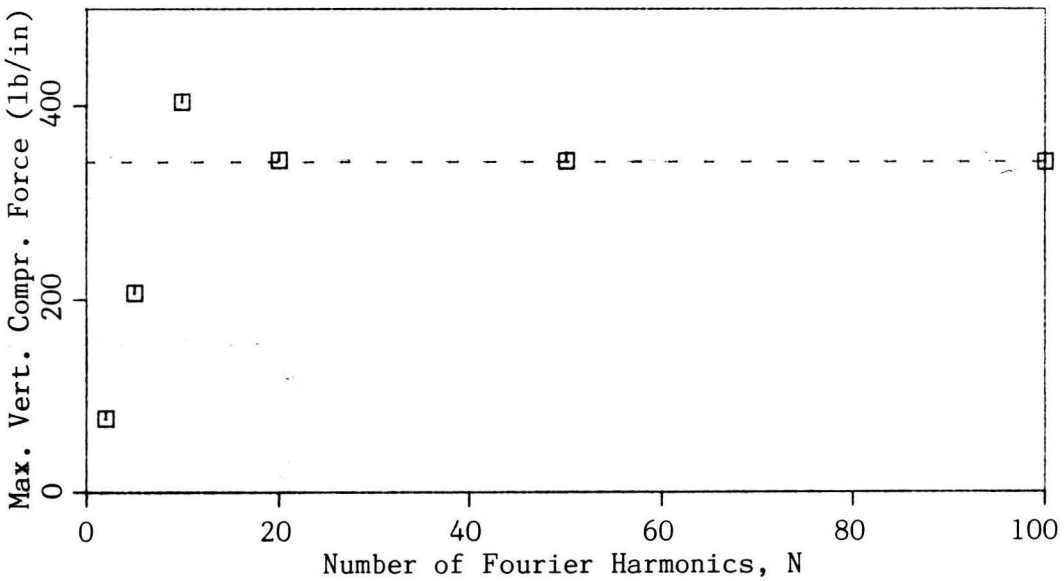


**Figure 4.6:** Convergence of maximum vertical compressive force for the tank tested by Clough and Niwa (1979). N=5,10,20,50,100. [13ft water, tilt=6.45°, closed]

foundation to the structure, but the length of the contact region is less than the tributary length ($\pi a/N$) for a discrete spring. As a result, the calculated maximum vertical compressive force per unit length is too low, and increases proportionately with N until there is more than one Winkler spring in compression, or, equivalently, until the length of the contact region exceeds the tributary length for a discrete spring.

The distribution of vertical stresses at the base of the shell is shown in Fig. 4.7 together with the experimental results by Clough and Niwa (1979)*. As can be seen, both theory and experiment show a higher compressive stress for the closed case. The reason for this is that the roof suppresses the inextensional deformation modes, leading to an increase in the vertical stiffness coefficients $K_{vn}$ and a decrease in the length of the contact region.

Perhaps the most marked discrepancy between theory and experiment occurs at $\theta = 0$. At this point, the uplift and the theoretical vertical tension in the shell wall is a maximum, but the experimental stress is zero. Almost equally surprising are the large tensile stresses at $\theta = 135^{\circ}$ and $270^{\circ}$ that were measured, but not indicated by the theory. Although these discrepancies are significant, the most important comparison is for the large compressive stresses. In design, the plane of motion is unknown and the design must accommodate these stresses at

---

* The comparison neglects the small stresses (about 20 psi) caused by the weight of the tank wall. These stresses are included in the analysis, but not in the experiment where only the changes in stresses from tilting were measured.

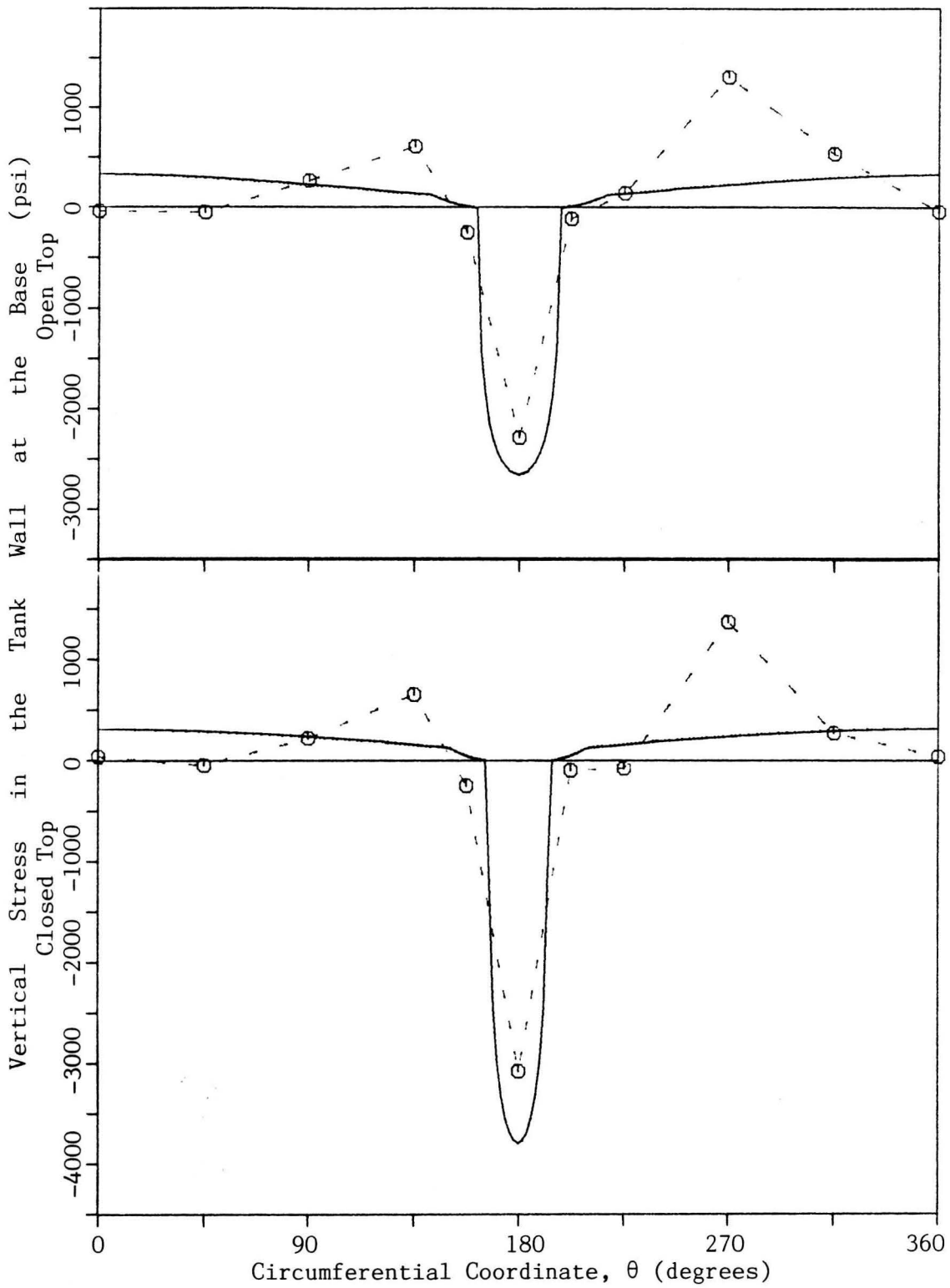


**Figure 4.7:** Theoretical (continuous line) and experimental distributions of vertical stress at the base. Experimental data (joined by dashed line) from Clough and Niwa (1979). [13ft water depth, 6.45° tilt]

any point in the circumference. For large compressive stresses, the theory and experiment agree quite well.

The Fourier coefficients for the displacements are shown in Table 4.1.

TABLE 4.1. Fourier Amplitudes of Vertical Uplift at Base, $U_n$, Theory Versus Experimental Results from Fig. 5.15 of Clough and Niwa (1979)

| | Open Top | | Closed Top | |
|---|---|---|---|---|
| n | Theory (in) | Experiment (in) | Theory (in) | Experiment (in) |
| 0 | 0.195 | .46 | 0.193 | .39 |
| 1 | 0.234 | .54 | 0.205 | .44 |
| 2 | 0.032 | .06 | 0.003 | .03 |
| 3 | -0.003 | .04 | -0.003 | .03 |

Both theory and experiment show larger displacements for the open case. However, for n = 0, 1, the experimental displacements are about double the theoretical displacements.

For larger n, the theoretical displacement coefficients are essentially zero, and the experimental values are also small, probably of the same order as the error in measuring them and scaling them from figures in the experimenters' report.

A comparison of the analytical results with the compressive stresses calculated by the code procedure of Wozniak and Mitchell (1978) is shown in Fig. 4.8. For the code analysis of the aluminum model, the

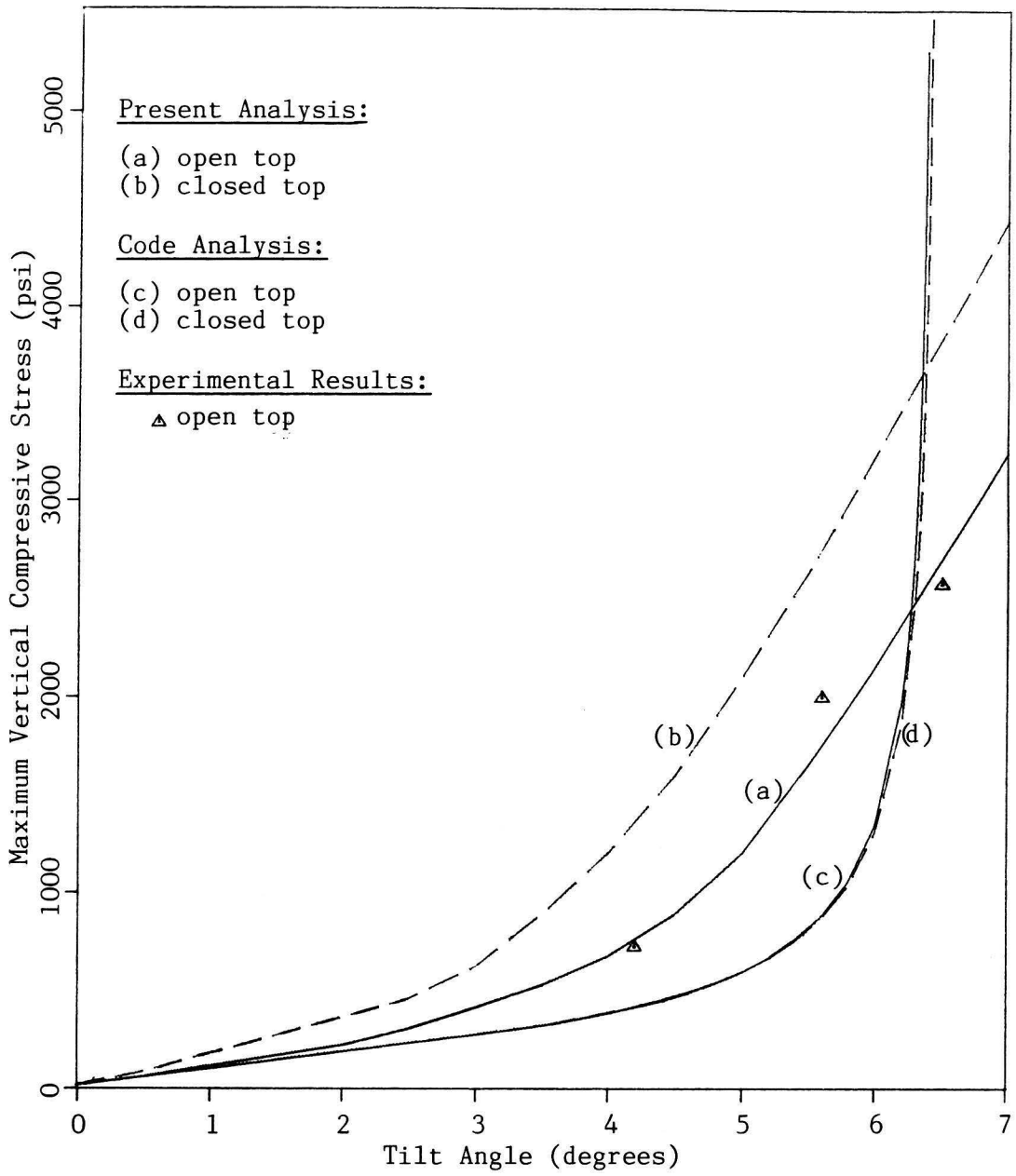


**Figure 4.8:** Maximum vertical compressive stress as a function of the tilt angle as obtained by

(i) the approximate method of analysis described in this chapter
(ii) the method of Wozniak and Mitchell (1978), which is also part of the American Water Works Association (1979) design standard
(iii) the experimental data from Clough and Niwa (1979).

yield stress of the base plate is taken to be 12 ksi, the appropriately scaled value for a mild steel prototype with a yield stress of 36 ksi. At a tilt angle of approximately $6.5^{\circ}$, the compressive stress calculated by the code procedure increases to infinity. For larger tilt angles the hold down force calculated by the code procedure is insufficient to prevent overturning. On the other hand, for smaller tilt angles, the maximum compressive stress from both the present analysis and the experimental results (the latter available for the open top case only) are higher than those from the code approach. Two reasons for this difference are offered: Firstly, the distribution of vertical compressive stresses is different from that assumed in the code analysis. In fact, for the open case at tilt angles between $1^{\circ}$ and $5^{\circ}$, the maximum compressive stress does not occur at $\theta = 180^{\circ}$. Secondly, and more importantly, in the code analysis, it is tacitly, but erroneously assumed that the hold down force is fully developed for any amount of uplift, no matter how small. In reality, a substantial amount of uplift is required to develop the hold down force, and, as a result, the length of the contact region decreases and the maximum compressive stress increases.

Since developing the required hold down force for an infinitesimal amount of uplift seems to be advantageous, the question that comes up naturally is whether the tank can be designed so that such conditions are achieved. It was in this context that the author conceived what might be termed the preuplift method: An annular filler is inserted under the tank wall as shown in Fig. 6.1, uplifting an annular region of

the base plate. For a properly designed filler, most of the weight of the fluid resting on that annular region is then carried by the filler in compression. As a result, for the tank wall to loose contact with the filler, the vertical tension in the tank wall must exceed the pre-compression in the ring filler. The effect of such preuplift on the behavior of a mylar tank is studied in Chapter 6 by analysis and experiment.

4.2.3.2 Broad Tank Tested by Manos and Clough (1982)

Design details for this 6 ft tall and 12 ft in diameter aluminum tank are much the same as for the tall tank discussed in Section 4.2.3.1. The shell consists of two 3 ft courses of aluminum of thicknesses of 0.08 in and 0.05 in for the lower and upper course, respectively. The entire base plate consists of an outer annulus and an inner portion. Both parts consist of 0.08 in thick aluminum sheet and are joined by a double ring of 3/32 in countersunk rivets at 3 in spacing. As before, the base plate is modeled as one continuous sheet of 0.08 in thick aluminum. All other design details, including the wind girder, are identical to those for the tank of Section 4.2.3.1 and are treated in the same way. The stiffness of the foundation in compression is taken to be $10^{11}$ lb/in$^2$ in order to simulate a rigid foundation.

The case considered is for the top open, 5 ft water depth, and $16^{\circ}$ tilt. In order to prevent the water from overflowing due to the tilt, the experimenters built an external structure to extend the tank. The forces resulting from water pressure acting on the external structure

were transmitted directly to the foundation and need therefore not be considered in the analysis of the tank. Also, to prevent leakage between the external structure and the tank a membrane was provided. The force exerted by the membrane on the tank is small, and was therefore neglected.

Theoretical and experimental results for this broad tank are shown in Figs. 4.9 to 4.11. The experimental stresses are the changes in stresses due to tilting*, measured 2 in above the base. Perhaps the most remarkable feature of the vertical stress distributions is the bimodal distribution of compressive stresses predicted by the theory, which is not seen in the experimental data. Although surprising at first, the theoretical result becomes more plausible when one bears in mind that the tank under consideration is broad and has no roof. As a result, inextensional deformation modes can be expected to play an important role. For an inextensional tank, there would be a number of discrete contact points. For the case of Fig. 4.10, there would probably be two such contact points located near the maxima of compressive stress shown in the figure. As the inextensionality requirement is relaxed, the compressive point reactions redistribute over a finite length resulting in a compressive stress distribution like that of Fig. 4.10.

Although the bimodal distribution of compressive stresses is consistent with what one might expect from the inextensional theory,

---

* The theoretical stresses also include a 7 psi uniform compression at zero tilt, which is negligible compared to stresses associated with tilting.

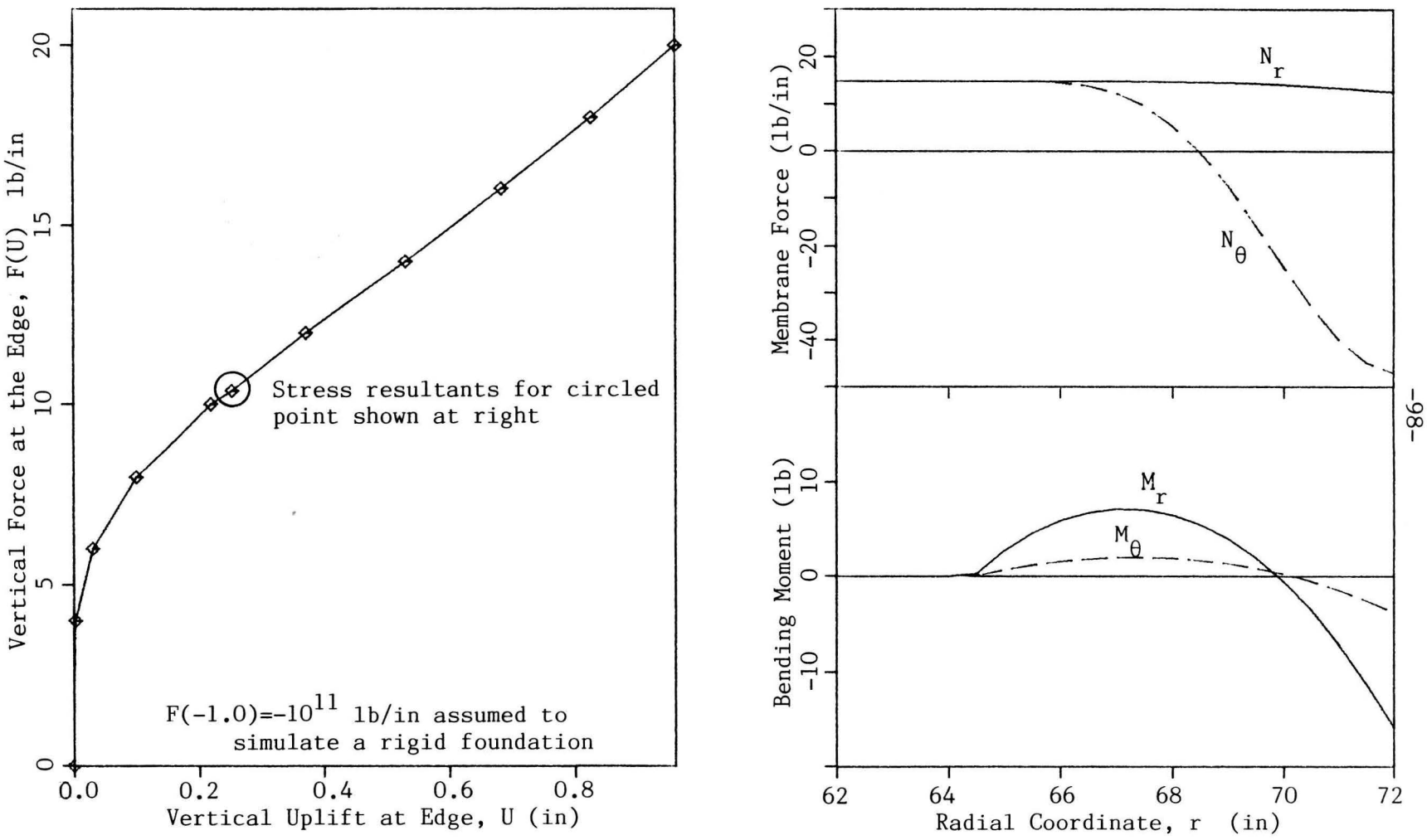


**Figure 4.9:** Results from the axisymmetric uplift analysis of the broad aluminum tank tested by Manos and Clough (1982). [5ft water depth]

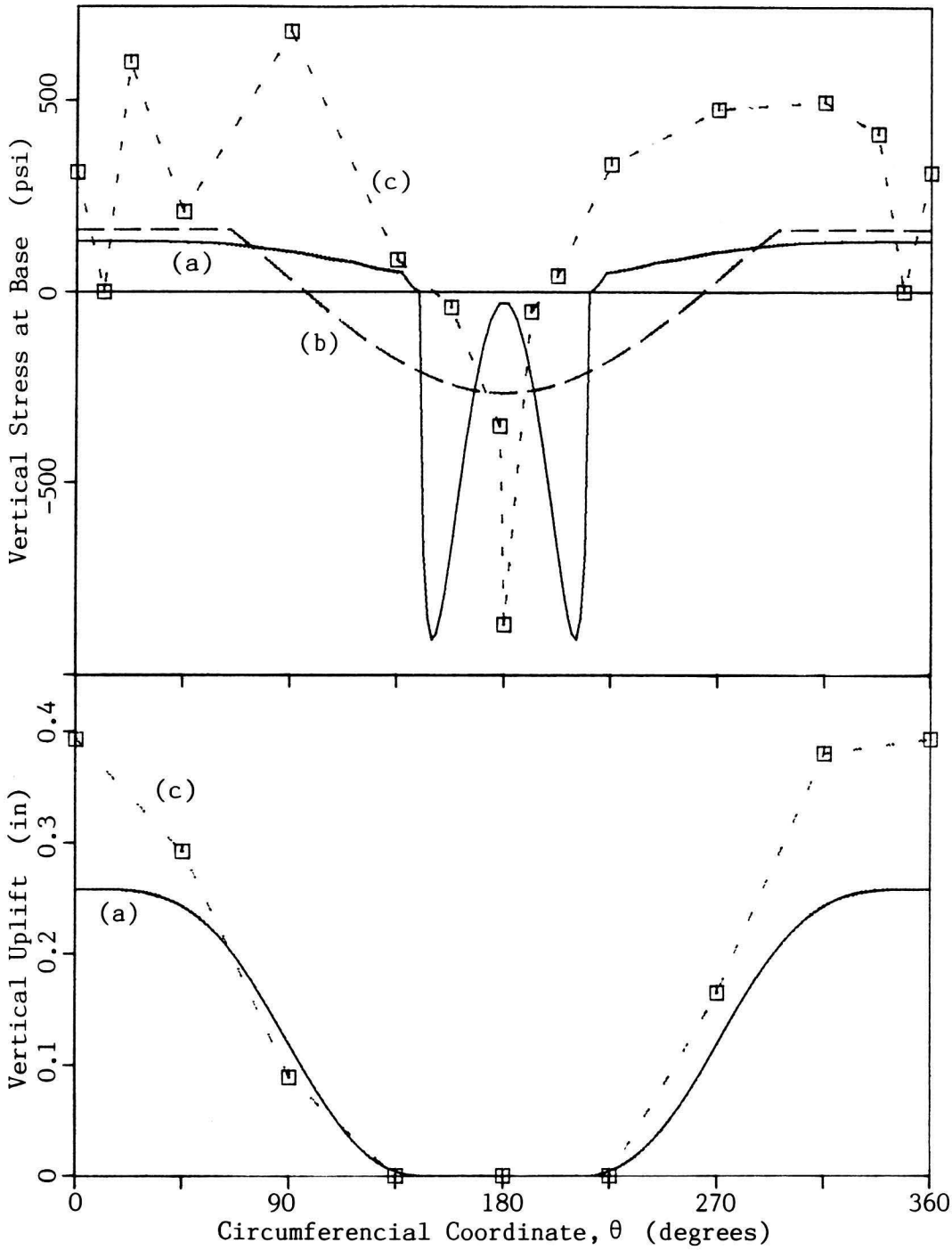


**Figure 4.10:** Results for broad aluminum tank [5 ft water depth, open top, 16° tilt, rigid foundation]
(a) Approximate method of analysis described in this Chapter,
(b) Code analysis of Wozniak and Mitchell (1979)
(c) Experimental results by Manos and Clough (1982), scaled with the permission of the authors from the report with an approximate precision of ±100 psi for stress, and ±0.05in for uplift.

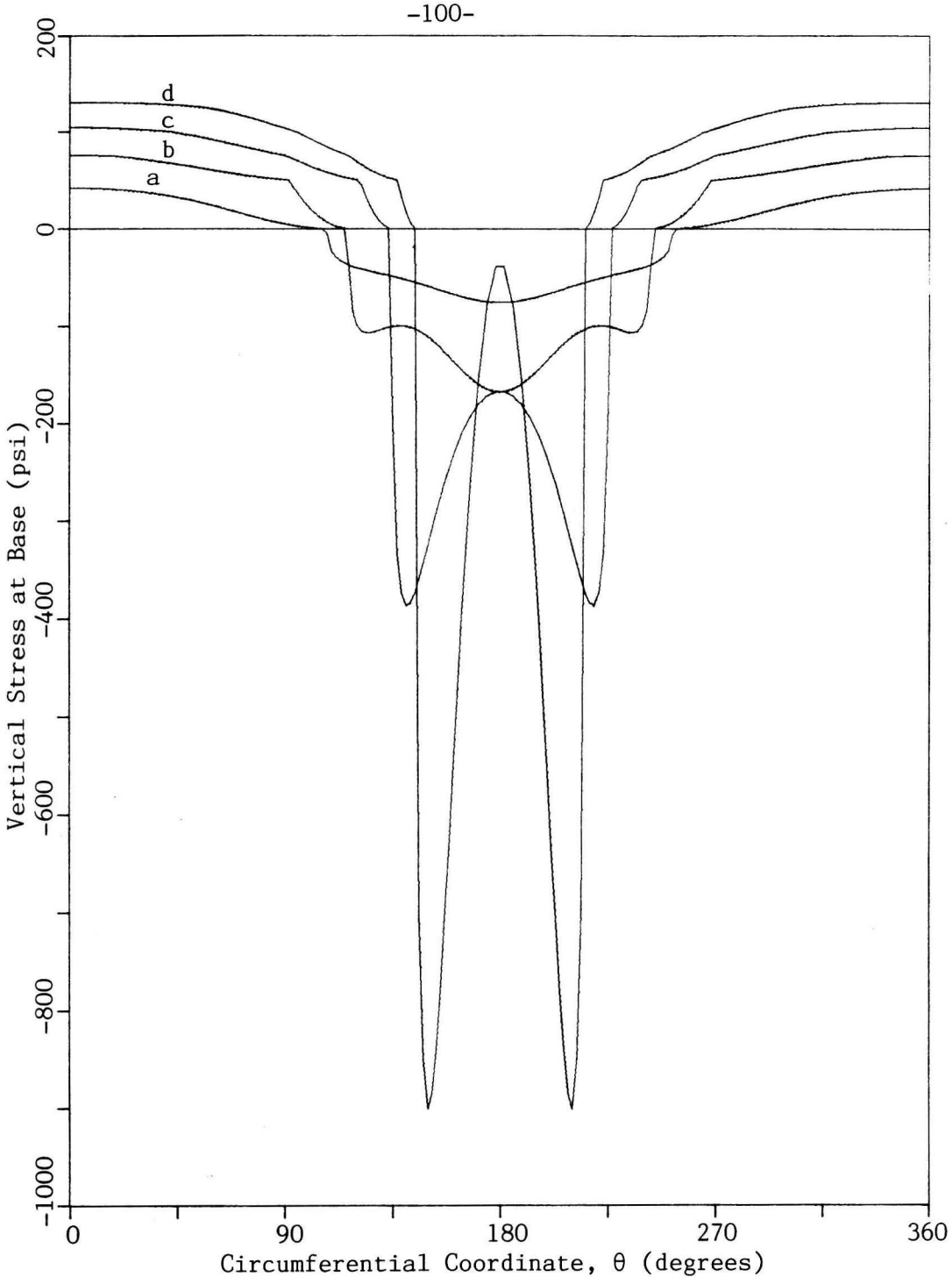


**Figure 4.11:** Calculated vertical stress at the base of the broad aluminum tank tested by Manos and Clough (1982). (a) $4^0$ tilt, (b) $8^0$ tilt, (c) $12^0$ tilt, (d) $16^0$ tilt. [rigid foundation, 5 ft water depth, no roof]

comparing it to the unimodal experimental stress distribution does raise some questions about the validity of the analysis and the assumptions made. It will be seen in Chapter 5 that the bimodal distribution of compressive stresses persists when the assumption of weak circumferential variations in the base plate is relaxed. Also, decreasing the stiffness of the foundation in compression to $10^7$ lb/in$^2$, a value more appropriate for a layer of mortar on a steel tilt table, does not noticeably change the stress distribution. An assumption which is more debatable for the case of a broad tank than for taller tanks, is that the changes in pressure acting at any point on the shell due to tilting are small compared to the hydrostatic pressure at zero tilt. If this is not true, then it is not appropriate to linearize the shell problem about the full, but otherwise not loaded (or tilted) condition, as was done in Appendix B.

The stress distribution from the code approach of Wozniak and Mitchell (1978) is shown in Fig. 4.10 as line (b). Again the peak compressive stress is seen to be much lower than that from the present analysis and the experimental results.

As was the case for the tall tank (Fig. 4.7), the experimental vertical stresses are very small at $\theta = 0$, where the maximum uplift occurs, while large vertical tensions were measured at $\theta = 90^\circ$, and $270^\circ$.

A puzzling feature of the experimental stress distribution is that the area above the zero line appears to be larger than the area below the zero line, indicating that there is a substantial net force acting

downward, at an angle from the vertical equal to the tilt angle $\alpha$. However, equilibrium of forces in that direction indicates that the net force (or the change in the net force due to tilting) can be no larger than the weight of the tank wall, which is very small.*

As for the tall tank, the measured uplift exceeds that predicted by the theory. Here the maximum differs by a factor of 1.5 as compared to a factor of 2.4 and 2.3 for the $n = 0$ and $n = 1$ Fourier coefficients of the uplift of the tall tank.

## 4.3 CLOSING REMARKS

It is seen that there are some significant differences between the results from the tank analysis described in this chapter, and those from experiments. Although some of these differences may be due to experimental error, and the error from scaling the results from the experimenters' reports, the consistency of certain trends in the test results strongly suggests that there are other reasons. For one, the assumption of weak circumferential variations in the base plate, which forms the basis of the analysis for the tank on nonlinear Winkler springs, may not be a good one. Other possible reasons include: Geometrically nonlinear effects in the shell, which are not considered in the linearized formulation of Appendix B, yielding of the aluminum, initial strains (either due to fabrication procedure, or due to yielding that may have occurred during previous testing of the tanks), flexibility of the joint between

---

* To be precise, the average compressive stress at zero tilt is 7 psi, and it decreases by (1-cos $\alpha$) times that amount for a tilt angle $\alpha$.

the inner and outer parts of the base plate, friction between the base plate and the foundation, or other modeling considerations. These possibilities will be discussed further in the next chapter, when the same experimental data are compared to the results of a more comprehensive analysis which does not rely on the assumption of weak circumferential variations.

## 5. NON-AXISYMMETRIC ANALYSIS OF AN UNANCHORED TANK

In Chapter 4 it was seen that, in some instances, the measured stresses and displacements due to tilting of two aluminum tanks differed significantly from analytical results based on the assumption of weak circumferential variations in the base plate. In this chapter, that assumption is relaxed, in order to verify its validity and to see to what extent it might be the cause of the difference between theoretical and experimental results. This requires solution of the two-dimensional nonlinear contact problem for the base plate.

### 5.1 ASSUMPTIONS

The analysis employs the following assumptions

1. Linear, small deflection theory is applicable for the shell, but nonlinear effects due to the internal hydrostatic pressure described in Appendix B are included. This means that the shell problem is linearized about the full but otherwise not loaded (or tilted) condition.
2. The moderate deflection Von Karman theory is used for the base plate. This also implies that strains in the base plate are small, and that the radii of curvature are much larger than the thickness.
3. The base plate material is elastic-perfectly plastic, with a Von Mises yield surface and a yield stress in uniaxial tension of $\sigma_y$. [c.f., in Chapter 2 it was assumed that the moment-

curvature relation is elastic-perfectly plastic, which is not the same assumption].

4. In compression, the foundation under the base plate behaves like a bed of Winkler springs with a modulus of subgrade reaction $k_0$ (foundation pressure per unit deflection). In addition, there is a circular bed of Winkler springs of stiffness $k_e$ (force per unit length per unit deflection) under the tank wall. Neither set of Winkler springs can sustain tension.
5. The foundation is frictionless, except at certain locations close to the center where sliding of the tank can be prevented by horizontal Winkler springs.

## 5.2 FORMULATION

For the non-axisymmetric analysis of the base, the finite difference energy method (FDEM) with an expansion of the displacements into a Fourier series is used. This method has been used with considerable success by Bushnell (1970, 1974, 1981) in his BOSOR (Buckling Of Shells Of Revolution) computer code. However, in his formulation, finite displacements are considered only for the n = 0 Fourier harmonic. The higher Fourier coefficients of the displacements are infinitesimal. Herein, all Fourier coefficients are allowed to be finite. This couples the equations for the Fourier coefficients resulting in a much more complicated problem requiring a much larger computational effort. Despite this coupling, the FDEM has several advantages over the finite element method:

a) Membrane locking problems are avoided.

b) Fewer degrees of freedom are required for a given accuracy.

c) There are no rotational degrees of freedom.

d) Less computational effort is required to form the tangent stiffness matrix.

e) The expansion of the displacements as a Fourier series is compatible with the finite element formulation for the shell given in Appendix B.

f) The method is simpler to implement.

On the other hand, the boundary conditions are a little more complicated, convergence is not necessarily from below, and the computer code had to be developed by the author. On balance, the advantages outweigh these minor drawbacks.

Before concentrating on the details of the analysis of the uplifting part of the base plate, three regions which are treated separately must be established.

The first is a concentric circular inner portion of the base plate, of radius $a_1$, chosen by the analyst such that no part of the inner portion ever uplifts. It is modeled by annular finite elements, possesses only horizontal degrees of freedom, and can be attached to the foundation by linear, horizontal Winkler springs which prevent sliding of the tank.

The second region is the shell and roof. It is modeled with the axisymmetric cylindrical shell elements of Appendix B, with added

stiffnesses due to the roof (Eq. 3.11) and ring stiffeners (Appendix D).

Since the equations for the first and second region are linear, their internal degrees of freedom be eliminated by static condensation to obtain linear boundary conditions for the third region, which is the outer annular portion of the base plate. A portion of this third region is uplifted. It has horizontal and vertical degrees of freedom, and is nonlinear due to plasticity, contact, and finite displacements. The rest of the discussion will concentrate on this nonlinear region. Since most of the computational effort is spent here, it is advisable to make this nonlinear region as small as possible by making the radius of the inner part of the base plate, $a_1$, as large as possible.

The finite element formulation of structural problems involving geometric and material nonlinearities is well known [Zienkiewicz (1977), Bathe (1982)], and will not be repeated here. The essential first steps which vary somewhat from problem to problem are the following:

(i) To establish a finite set of generalized displacements which at any time define the configuration of the structure.

(ii) To express the strains* in terms of those generalized displacements.

---

* Here stresses and strains are to be understood in a generalized fashion as vectors of equal dimension such that the dot product of the stress with an increment in strain is the change in strain energy density. This is the only requirement for the choice of stress and strain vectors. The exact nature of these vectors depends on the structural element being modeled. Also, the change in strain energy density may be a change in strain energy per unit volume, per unit area, or per unit length.

(iii) To be able to calculate stresses and the tangent material matrix (partial derivatives of the stresses with respect to the strains) for any history of strains.

Once these three steps are achieved, the rest of the finite element formulation follows standard procedures.

The only difference between the finite element method and the finite difference energy method (FDEM) is that in the FDEM, displacements are specified at certain nodal points without specifying exactly how the displacements vary in between nodal points, and the strains are only defined at certain "integration points"* as finite differences of the nodal displacements.

Consider now step (i), describing the configuration of the structure in terms of a finite set of generalized displacements. Let there be NN real nodes, which are actually circles, equally spaced with the first node on the inner boundary, $r = a_1$, and the NNth node on the outer boundary $r = a$. Thus the ith node is located at

$$r_i = a_1 + (i-1)h \quad , \tag{5.1}$$

where

$$h = (a-a_1)/(NN-1) \quad . \tag{5.2}$$

---

* These "integration points" are equivalent to the Gaussian integration points often used in the finite element method when numerical integration of the variations of the strain energy density is required. Here they coincide with nodal points.

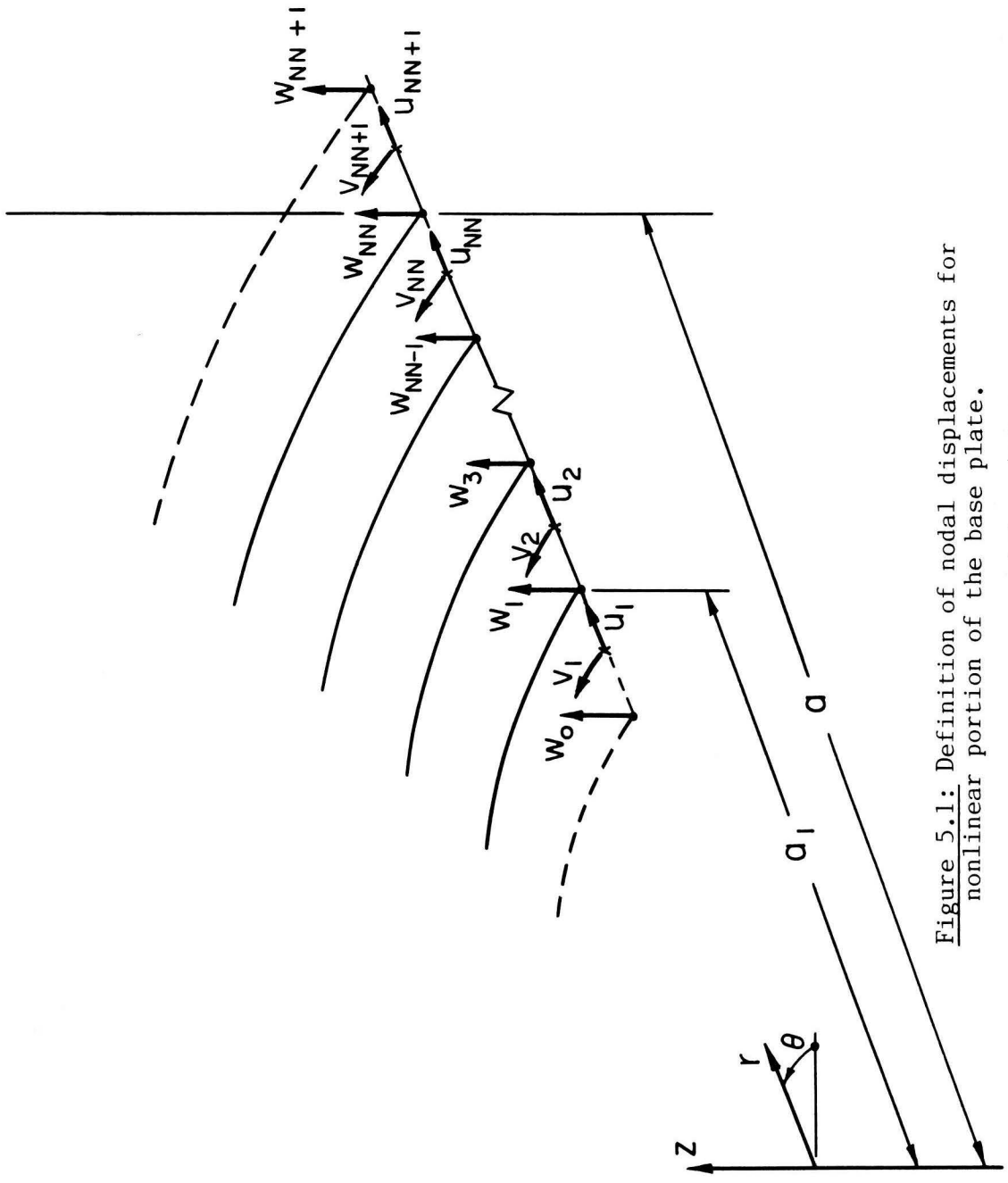


Figure 5.1: Definition of nodal displacements for nonlinear portion of the base plate.

Furthermore, in order to enforce the boundary conditions, a 0th node and an (NN+1)th node are required at locations defined by Eq. 5.1 with i = 0, and i = NN+1 respectively. It is also advantageous to define intermediate nodes, with the ith intermediate node located at $r = r_i - h/2$, for i = 1,2,..., NN, NN+1.

As illustrated in Fig. 5.1, the nodal displacements are

$$w_i = \sum_{n=0}^{NW} w_i^n N_n(\theta) \quad , \tag{5.3}$$

at nodes i = 0,1,2,..., NN, NN+1; and

$$u_i = \sum_{n=0}^{NH} u_i^n \cos n\theta \tag{5.4}$$

$$v_i = \sum_{n=1}^{NH} v_i^n \sin n\theta \quad , \tag{5.5}$$

at the intermediate nodes, i = 1,2,..., NN+1. In Eqs. 5.3 to 5.5 u, v, and w represent the displacements in the radial (positive outwards), circumferential (positive anticlockwise as seen from on top), and vertical (positive upward) directions, respectively. The superscript n is used to identify the coefficients of the expansions, and should not be interpreted as an exponent. NH and NW are the order of the last terms in the Fourier series for horizontal and vertical displacement components, respectively. Finally $N_n(\theta)$ is a cosine series of order NW which satisfies

$$N_n(\tfrac{m\pi}{NW}) = 1 \quad \text{for} \quad m = n$$

$$= 0 \quad \text{for} \quad m \in \{0,1,2,\ldots,NW\}-\{n\} \quad . \qquad (5.6)$$

From the theory of discrete Fourier transforms (see Appendix C), it is readily established that

$$N_n(\theta) = \frac{2\gamma_{n/NW}}{NW} \sum_{k=0}^{NW} \gamma_{k/NW} \cos \frac{nk\pi}{NW} \cos k\theta \quad ,$$

in which

$$\gamma_s = 1/2 \quad \text{for} \quad s = \ldots -2,-1,0,1,2,\ldots$$

$$= 1 \quad \text{otherwise} \quad .$$

The advantage of using Eq. 5.3 rather than a simple cosine series is that added stiffness due to vertical Winkler springs representing the foundation is added into the diagonal elements of the stiffness matrix. Since, for a rigid foundation, the added stiffness may be very large, this is not only convenient, but essential to avoid excessive truncation errors. In essence, using Eq. 5.3 rather than a simple cosine series is equivalent to introducing the change of variables made in Section 4.2.1.

Before proceeding to step (ii), which is to express strains in terms of the generalized displacements, it is appropriate to consider how the variations in strain energy density will be integrated, in order to establish what quantities should be used as strains for each structural element, and at what points the expressions for the strains are required. Four types of structural elements are considered here.

1. The base plate itself.
2. The annular bed of Winkler springs of stiffness $k_o$ (pressure per unit deflection) in compression.
3. The circle of Winkler springs under the base of the tank wall, with stiffness $k_e$ (force per unit length per unit deflection) in compression.
4. Linear constraints applied at any given real node, such as the boundary conditions due to the inner part of the base plate at node 1, and the boundary conditions due to the shell at node NN.

Expressions for the variation in strain energy for each of these four structural elements will be given in Sections 5.1.1 to 5.1.4. These contributions must be summed to obtain the total variation in strain energy.

### 5.2.1 Base Plate

Of the stress components $\sigma_{rr}$, $\sigma_{r\theta}$, $\sigma_{\theta\theta}$, $\sigma_{rz}$, $\sigma_{\theta z}$, and $\sigma_{zz}$, where z is the vertical coordinate (positive upwards, with z = 0 denoting the midsurface of the plate), only the first three are non zero. The variation in the strain energy per unit volume at location $(r,\theta,z)$ can be written as

$$\delta U(r,\theta,z) = \delta\varepsilon^T\sigma \quad , \tag{5.8}$$

in which

$$\sigma = \left[\sigma_r \quad \sigma_\theta \quad \sigma_{r\theta}\right] \tag{5.9a}$$

are the in-plane stresses, and

$$\varepsilon = \left[\bar{\varepsilon}_r \quad \bar{\varepsilon}_\theta \quad 2\bar{\varepsilon}_{r\theta}\right] \tag{5.9b}$$

are the strains. The contribution to the variation in strain energy due to the plate is

$$\int_{a_1}^{a} \int_{-\pi}^{\pi} \int_{-t/2}^{t/2} \delta U(r,\theta,z)\,dz\; r\,d\theta\; dr \quad , \tag{5.10}$$

in which t is the thickness of the base plate. Replacing the integrations with respect to r and θ by summations, and taking advantage of the symmetry of the integrand with respect to θ, expression 5.10 becomes

$$\sum_{i=1}^{NN} h\gamma_{i/NN}\, r_i \left[\frac{2\pi}{NC} \sum_{j=0}^{NC} \gamma_{j/NC} \int_{-t/2}^{t/2} \delta U\left(r_i\,,\, \frac{j\pi}{NC}\,,\, z\right)dz\right] \quad , \tag{5.11}$$

in which NC, the number of integration points around the circumference, is chosen depending on the accuracy desired. The remaining integration across the thickness of the plate is also done numerically using Simpson's rule with five integration points across the thickness. This scheme is exact when the cross section remains elastic, and has the advantage over Gaussian integration that there are points on both surfaces of the plate. Thus yielding starting on the surface of the plate is "detected" immediately. Furthermore, if the section becomes fully plastic in pure bending, Simpson's rule with five integration

points is also exact.

Following Kirchhoff's hypothesis that plane sections remain plane, the strains are written as

$$\begin{aligned} \bar{\varepsilon}_r &= \varepsilon_r - z\,\kappa_r \\ \bar{\varepsilon}_\theta &= \varepsilon_\theta - z\,\kappa_\theta \\ \bar{\varepsilon}_{r\theta} &= \varepsilon_{r\theta} - z\,\kappa_{r\theta} \quad , \end{aligned} \tag{5.12 a-c}$$

in which $\varepsilon_r$, $\varepsilon_\theta$ and $\varepsilon_{r\theta}$ are the midsurface (or membrane) strains, and $\kappa_r$, $\kappa_\theta$ and $\kappa_{r\theta}$ are the curvatures. Their values at a generic integration point located at $(r,\theta) = (r_i, j\pi/NC)$ are given by:

$$\varepsilon_r = \frac{1}{h}\sum_{n=0}^{NH}(u_{i+1}^n - u_i^n)\cos(nj\pi/NC)$$

$$+ \tfrac{1}{2}\left[\frac{1}{2h}\sum_{n=0}^{NH}(w_{i+1}^n - w_{i-1}^n)N_n(j\pi/NC)\right]^2$$

$$\varepsilon_\theta = \sum_{n=1}^{NH}\frac{n}{2r_i}(v_i^n + v_{i+1}^n)\cos(nj\pi/NC)$$

$$+ \sum_{n=0}^{NH}\frac{1}{2r_i}(u_i^n + u_{i+1}^n)\cos(nj\pi/NC)$$

$$+ \tfrac{1}{2}\left[\frac{1}{r_i}\sum_{n=0}^{NW} w_i^n\, N_n^{\cdot}(j\pi/NC)\right]^2$$

$$2\varepsilon_{r\theta} = \sum_{n=1}^{NH} \left[ \frac{1}{h} (v_{i+1}^n - v_i^n) - \frac{n}{2r_i} (u_i^n + u_{i+1}^n) \right.$$

$$\left. - \frac{1}{2r_i} (v_i^n + v_{i+1}^n) \right] \sin(nj\pi/NC)$$

$$+ \left[ \frac{1}{2h} \sum_{n=0}^{NW} (w_{i+1}^n - w_i^n) N_n(j\pi/NC) \right] \left[ \frac{1}{r_i} \sum_{n=0}^{NW} w_i^n N_n^{\cdot}(j\pi/NC) \right]$$

$$\kappa_r = \frac{1}{h^2} \sum_{n=0}^{NW} (w_{i-1}^n - 2w_i^n + w_{i+1}^n) N_n(j\pi/NC)$$

$$\kappa_\theta = \frac{1}{r_i^2} \sum_{n=0}^{NW} w_i^n N_n^{\cdot\cdot}(j\pi/NC)$$

$$+ \frac{1}{2hr_i} \sum_{n=0}^{NW} (w_{i+1}^n - w_{i-1}^n) N_n(j\pi/NC)$$

$$2\kappa_{r\theta} = \sum_{n=0}^{NW} \left[ \frac{1}{r_i h} (w_{i+1}^n - w_{i-1}^n) - \frac{2}{r_i^2} w_i^n \right] N_m^{\cdot}(j\pi/NC) \qquad (5.13\ a\text{-}f)$$

Equations 5.12 and 5.13 define the strains in terms of the generalized displacements. It only remains to establish the stress-strain relationship, and the tangent material matrix. This is done in Appendix F, using the method of radial return (or elastic predictor, radial corrector method).

### 5.2.2 Annular Bed of Winkler Springs

The variation of the strain energy for the annular bed of Winkler springs is

$$\int_{a_1}^{a} \int_{-\pi}^{\pi} k_o C(w)\delta w \, r d\theta \, dr \quad , \tag{5.14}$$

in which

$$\begin{aligned} C(x) &= x \qquad \text{if} \quad x \leq 0 \\ &= 0 \qquad \text{otherwise} \quad . \end{aligned} \tag{5.15}$$

In equation 5.14 the vertical displacement w can be considered to be the "strain," and $\delta$ denotes a variation. With numerical integration expression 5.15 becomes

$$h \sum_{i=1}^{NN} \gamma_{i/NN} \frac{2\pi a}{NW} \sum_{n=0}^{NW} \gamma_{n/NW} \, k_o C(w_i^n)\delta w_i^n \quad . \tag{5.16}$$

Note that the integration in $\theta$ is replaced by summation over NW points, which would normally be less than the number of points (NC) used for integrating the strain energy in the plate. As in Section 4.2, this is considered advantageous in order to avoid locking problems. It also means that these springs affect only the diagonal elements of the stiffness matrix.

### 5.2.3 Circular Bed of Winkler Springs

In Chapter 6, tanks for which the tank wall is preuplifted by placing a annular filler under the tank wall (Fig. 6.1) will be analyzed. For such a tank, the force per unit length in the circular bed of springs under the tank wall is $k_e C(w-w_{pre})$, in which $w_{pre}$ is the

preuplift. As a result, the contribution to the variation in strain energy for these springs is

$$\int_{-\pi}^{\pi} k_e C(w-w_{pre})\delta w \, a d\theta \quad , \tag{5.17}$$

which is approximated by

$$\frac{2\pi a}{NW} \sum_{n=0}^{NW} k_e C(w_{NN}^n - w_{pre})\delta w_{NN}^n \quad . \tag{5.18}$$

In this chapter preuplift is not applied, and therefore $w_{pre} = 0$.

### 5.2.4 Linear Constraints

A linear constraint at node i arises from the static condensation of any linear, axisymmetric structure attached to node i. Thus, there is a constraint at node 1 due to the inner part of the base plate, and at node NN due to the cylindrical shell and roof. The variation of the strain energy for such constraints can be written in the form

$$\sum_{n=0}^{\text{Max}(NH,NW)} \delta_n \pi a \, \delta q_n^T (F_n + K_n q_n) \quad , \tag{5.19}$$

in which

$$\delta_n = \begin{cases} 2 & \text{for} \quad n = 0 \\ 1 & \text{otherwise} \quad , \end{cases} \tag{5.20}$$

$$q_n = \left[ u_n \quad v_n \quad w_n \quad x_n \right] , \tag{5.21}$$

where

$$u_n = \tfrac{1}{2}(u_i^n + u_{i+1}^n) \qquad \text{for} \quad n = 0,1,2,\ldots,NH$$

$$= C \qquad \text{otherwise} , \tag{5.22}$$

$$v_n = \tfrac{1}{2}(v_i^n + v_{i+1}^n) \qquad \text{for} \quad n = 1,2,\ldots,NH$$

$$= 0 \qquad \text{otherwise} , \tag{5.23}$$

$$w_n = \frac{2\gamma_n/NW}{NW} \sum_{k=0}^{NW} \gamma_{k/NW} \, w_i^k \cos(nk\pi/NW)$$

$$\text{for} \quad n = 0,1,\ldots,NW$$

$$= 0 \qquad \text{otherwise} , \tag{5.24}$$

$$x_n = \frac{2\gamma_n/NW}{NW} \sum_{k=0}^{NW} \gamma_{k/NW} \, \frac{1}{2h} \, (w_{i+1}^k - w_{i-1}^k) \cos(nk\pi/NW)$$

$$\text{for} \quad n = 0,1,\ldots,NW$$

$$= 0 \qquad \text{otherwise} , \tag{5.25}$$

are the nth Fourier coefficients of the displacement components in the r, $\theta$, z directions (base plate coordinates) and the rotation about the circumferential axis respectively. $F_n$, $4 \times 1$ vectors, and $K_n$, $4 \times 4$ matrices, are obtained from the static condensation of the attached structure. The elements of the $4 \times 1$ vector $(F_n + K_n q_n)$ are the nth Fourier coefficients of the forces per unit length and the moment per unit length acting on the attached structure in the directions of the

displacements $u_n$, $v_n$, $w_n$ and the rotation $\chi_n$, respectively.

## 5.3 CRITERIA FOR CHOOSING NW, NH, AND NC

The convergence studies in Chapter 4 (Fig. 4) can be used as a guide in choosing the number of Fourier harmonics required for the vertical displacement, NW. For the choice of NH, the number of Fourier harmonics for the horizontal displacements, and NC, the number of integration points in the circumferential direction, the following results were helpful.

Result 1:

If no yielding occurs, then the numerical integration in the circumferential direction indicated in epression 5.11 is exact if

$$NC > \max(2NW, NH) \quad . \tag{5.26}$$

This result can be obtained by using eqs. 5.8 to 5.13 to evaluate the nature of the integrand, and the discrete orthogonality relation of Appendix C. It can also be shown that the variation in strain energy due to bending is integrated exactly if NC > NW.

Result 2:

If

a) there is no yielding, and

b) the horizontal loads are of Fourier order* 2NW,

then the horizontal displacements are of Fourier order 2NW. Thus,

$$u_i^n = v_i^n = 0 \qquad \text{for} \quad n > 2NW \ .$$

This means that under such conditions, making NH greater than 2NW serves no useful purpose.

Briefly, the reason is that vertical displacements of Fourier order NW induce membrane strains of Fourier order 2NW. If no horizontal displacements are allowed while the vertical displacements are applied, the horizontal forces that are required to achieve this are also of Fourier order 2NW. Releasing these, restraining forces results in horizontal displacements of Fourier order 2NW.

Result 3:

Since the variation in the strain energy is not integrated exactly, the displacements do not necessarily converge from below. A special case occurs when

a) NW = 1, and

b) NN and NC are sufficiently large to achieve essentially exact integration of the variation of the strain energy in the base plate.

What is special about this case is that even though the distributed Winkler springs are replaced by discrete springs on the axis of loading, the vertical displacement at any point on the circumference is in between the displacements at the discrete springs. This means that for a rigid foundation the displacements are non-negative over the entire

* Herein a function $f(\theta)$ is said to be of "Fourier order" N if it can be written in the form $f(\theta) = \sum_{n=0}^{N} f_n e^{in\theta}$.

circumference. Hence, the displacements (or, strictly, the work done by the applied loads) are a lower bound.

## 5.4 IMPLEMENTATION AND COMPUTATIONAL CONSIDERATIONS

The generalized displacements are arranged into a vector q as follows

$$q = \left[ w_o^o \; w_o^1 \; \cdots \; w_o^{NW} \; u_1^o \; \cdots \; u_1^{NH} \; v_1^1 \; \cdots \; v_1^{NH} \; w_1^o \; \cdots \; w_1^{NW} \right.$$

$$\left. w_{NN}^o \; \cdots \; w_{NN}^{NW} \; u_{NN+1}^o \; \cdots \; u_{NN+1}^{NH} \; v_{NN+1}^1 \; \cdots \; v_{NN+1}^{NH} \; w_{NN+1}^o \; \cdots \; w_{NN+1}^{NW} \right] \quad , (5.27)$$

the total number of degrees of freedom is

$$\text{NUMDOF} = (NN+2)(NW+1) + (NN+1)(2NH+1) \quad . \qquad (5.28)$$

The generalized displacements which affect the stresses and strains at the ith node are arranged into an "element displacement vector" $q_i$ as follows

$$q_i = \left[ w_{i-1}^o \; \cdots \; w_{i-1}^{NW} \; u_i^o \; \cdots \; u_i^{NH} \; v_i^1 \; \cdots \; v_i^{NH} \; w_i^o \; \cdots \; w_i^{NW} \right.$$

$$\left. u_{i+1}^o \; \cdots \; u_{i+1}^{NH} \; v_{i+1}^1 \; \cdots \; v_{i+1}^{NH} \; w_{i+1}^o \; \cdots \; w_{i+1}^{NW} \right] \quad .$$

The number of elements in this element displacement vector is

$$\text{NBD} = 3(NW+1) + 2(2NH+1) \quad , \qquad (5.29)$$

which is also the half-bandwidth of the tangent stiffness matrix.

Newton Iteration was used to solve the nonlinear algebraic system of equations. The computational effort to factorize the tangent stiffness matrix at each iteration is approximately proportional to NUMDOF $(NBD)^2$, which for NH = NW is in turn approximately proportional to $NN(NW)^2$.

## 5.5 TEST PROBLEMS

The computer program developed for the non-axisymmetric analysis of the base plate will be referred to as NAAOAP (Non-Axisymmetric Analysis of Annular Plates). Constraint conditions can be imposed at any of the nodes. Using this feature, and setting the foundation stiffness to zero, the program can be used for annular plate problems for which the solution can also be obtained with the BOSOR5 program developed by Bushnell (1974)*. For various axisymmetric problems, including one involving a large amount of plastic deformation, the results from the two programs are in good agreement.

In addition, to test the program for non-axisymmetric deformations, with strong geometrically nonlinear effects, the following problem involving bifurcation buckling with a relatively small number of circumferential waves is solved: An annular plate of thickness t = 1 in, modulus of elasticity $E = 29 \times 10^6$ psi, Poisson's ratio $\nu = 0.3$, inner radius 100 in and outer radius 200 in is simply supported ($u = v = w = 0$, $M_r = 0$) at the inner edge, and free at the outer edge.

---

* Some of the features and capabilities of this program are described in Appendix A.

A transverse pressure p is applied. This produces an axisymmetric deformation of the plate. However, as the pressure increases, large compressive membrane forces develop near the outer edge in the circumferential direction. These stresses eventually cause buckling in a non-axisymmetric mode. From the BOSOR5 analysis, the buckling pressure is found to lie between p = 0.21 psi and p = 0.22 psi as indicated in Fig. 5.2 by the vertical lines. The circumferential wavenumber for the critical buckling mode is n = 3. This means that the displacements for the buckling mode vary like cos 3θ or sin 3θ in the circumferential direction.

For the NAAOAP analysis, the tangent stiffness matrix should become singular as the buckling pressure is approached. To avoid this, a small transverse line load (force per unit length = 0.003 lb/in cos 3θ) is applied at the outer edge. This introduces a small displacement (about 0.001 in in the transverse direction) with a circumferential variation similar to that for the buckling mode. The non-axisymmetric line load is kept constant, whereas the pressure p is increased gradually.

The NAAOAP analysis was performed with NN = 21 for the number of nodes, NW = NH = 3 for the number of Fourier coefficients to be included, and NC = 7 to achieve exact integration in the circumferential direction. The n = 0 and n = 3 Fourier coefficients of the transverse displacement at the outer edge are shown in Fig. 5.2. (The n = 1 and n = 2 Fourier coefficients are less than $10^{-9}$ in. The n = 0 Fourier coefficient is in excellent agreement (better than 0.2% for pressures up to the buckling pressure) with the axisymmetric solution from BOSOR5.

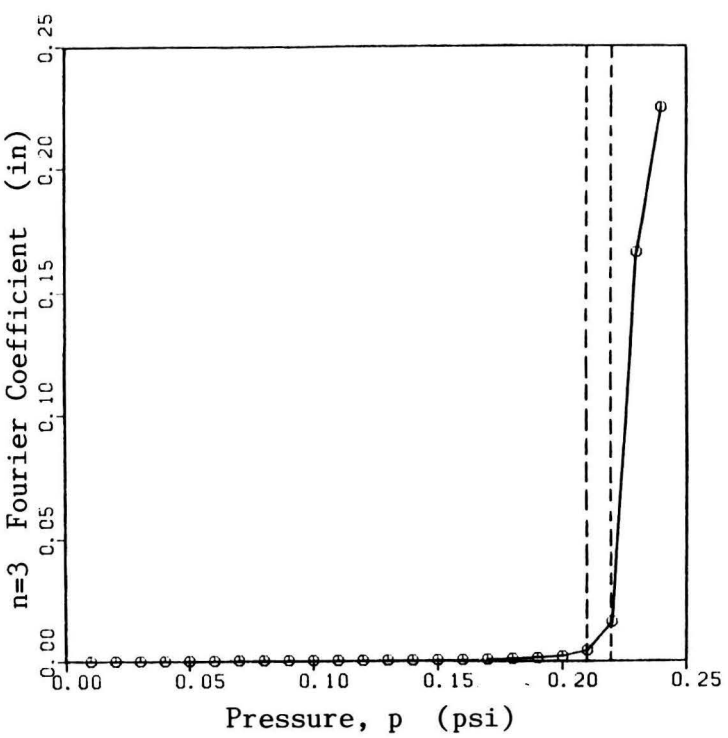


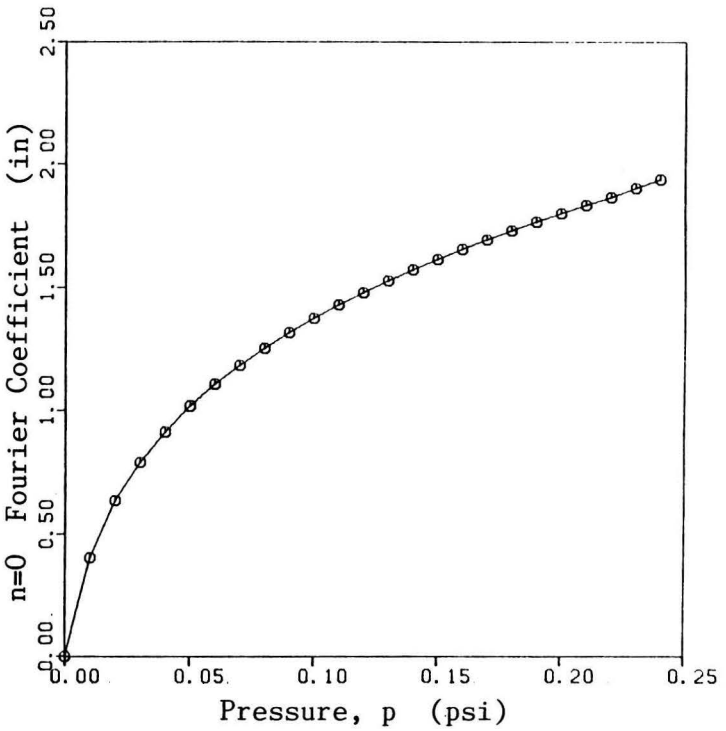


Figure 5.2: Fourier coefficients of the transverse displacement at the outer edge for the annular plate problem described in Section 5.5.
Notes:
a) The dashed vertical lines are the bounds to the buckling pressure established with BOSOR5.
b) Each marker indicates a loading step.

Also, for the n = 3 Fourier coefficient, the behavior is exactly what might be expected: The small displacement due to the non-axisymmetric line load is greatly amplified as the critical pressure is approached. Beyond the critical pressure the non-axisymmetric deformation increases rapidly.

## 5.6 RESULTS

As in Section 4.2.3, the analysis is performed for the tall and broad aluminum tanks tested at the University of California at Berkeley [Clough and Niwa (1979), Manos and Clough (1982)]. These will be discussed in Sections 5.5.1 and 5.5.2. In addition, a mylar tank tested by Shih (1981) is analyzed, and the calculated uplift is compared with the experimental readings in Section 5.5.3.

### 5.6.1 Tall Tank Tested by Clough and Niwa (1979)

This tank, and the assumptions made in modeling it, are described in Section 4.2.3.1. The only difference in this section is that the assumption of weak circumferential variations in the base plate is relaxed, and the changes in pressure acting on the base plate due to tilting are included. However, the effect of changes in the elevation of a point on the base plate on the pressure at that point are neglected. (Recall that the latter are included in the analysis of the shell).

The stiffness in compression for the circular bed of Winkler springs at the edge is taken to be $10^{11}$ lb/in$^2$, and for the annular bed of springs under the nonlinear portion of the base plate, the stiffness is taken to be $10^{10}$ lb/in$^3$.

The inner radius of the annular, nonlinear portion of the base plate is $a_1$ = 38.5 in (see Fig. 5.1). This allows for a maximum width of the uplifted strip of 8 in. NN = 17 is used for the number of nodes, resulting in a radial spacing of 0.5 in between nodes. The inner part of the base plate is attached to the foundation with horizontal Winkler springs of stiffness 2,500 lb/in$^3$ over a circle of radius 7.5 in at the center of the tank.

Based on the convergence study in Fig. 4.6, NW = 30 is chosen so that accurate values of the vertical stresses can be obtained. For the horizontal displacements, NH = 12 is judged sufficient. Finally, NC = 61 is used to achieve exact integration around the circumference.

The results are shown in Table 5.1 lines 4 and 9, and Figures 5.3 to 5.7. In some cases the results of the experiments and the approximate analysis of Chapter 4 are also shown for comparison. Some of the features of these results deserve discussion:

Figures 5.3 and 5.4 indicate that the base plate is uplifted radially inwards from locations where the shell wall (outermost node or circle) is in contact with the foundation. This occurs because the fluid pressure acting on the shell wall causes it to rotate about the circumferential axis at the edge. This rotation is also experienced by the base plate, and causes the base plate to uplift slightly inward from

the edge.

TABLE 5.1. Fourier Amplitudes of Vertical Uplift at Base (in) for the Tall Aluminum Tank Tested by Niwa and Clough (1979) [6.45° tilt, 13 ft water depth]

| | | | | |
|---|---|---|---|---|
| 1. Harmonic number, n | 0 | 1 | 2 | 3 |
| Open Top: | | | | |
| 2. Experiment[1] | 0.46 | 0.54 | 0.06 | .04 |
| 3. Approximate theory of Chapter 4 | 0.195 | 0.234 | 0.032 | -0.003 |
| 4. Present analysis[2] | 0.225 | 0.267 | 0.034 | -0.004 |
| 5. Modified present analysis[3] | 0.316 | 0.362 | 0.038 | -0.004 |
| 6. Modified present analysis[4] | 0.422 | 0.468 | 0.038 | -0.004 |
| Closed Top: | | | | |
| 7. Experiment | 0.39 | 0.44 | 0.03 | 0.03 |
| 8. Approximate theory of Chapter 4 | 0.193 | 0.205 | 0.003 | -0.003 |
| 9. Present analysis[2] | 0.222 | 0.234 | 0.003 | -0.003 |
| 10. Modified present analysis[3] | 0.313 | 0.323 | 0.004 | -0.003 |
| 11. Modified present analysis[4] | 0.428 | 0.436 | 0.004 | -0.003 |

Notes:

1. Experimental data obtained from Clough and Niwa (1979) with the authors' permission.

2. Standard analysis, assumptions include no yielding, and the base plate modeled as one continuous sheet of 0.09 in thick aluminum.

3. Modified analysis, includes plasticity in the base plate with a yield stress of 12 ksi, and a perfectly flexible gasketed joint in the base plate.

4. Modified analysis as described in note 3, but the tilt angle was increased to 8.5° with subsequent unloading to a tilt angle of 6.45°.

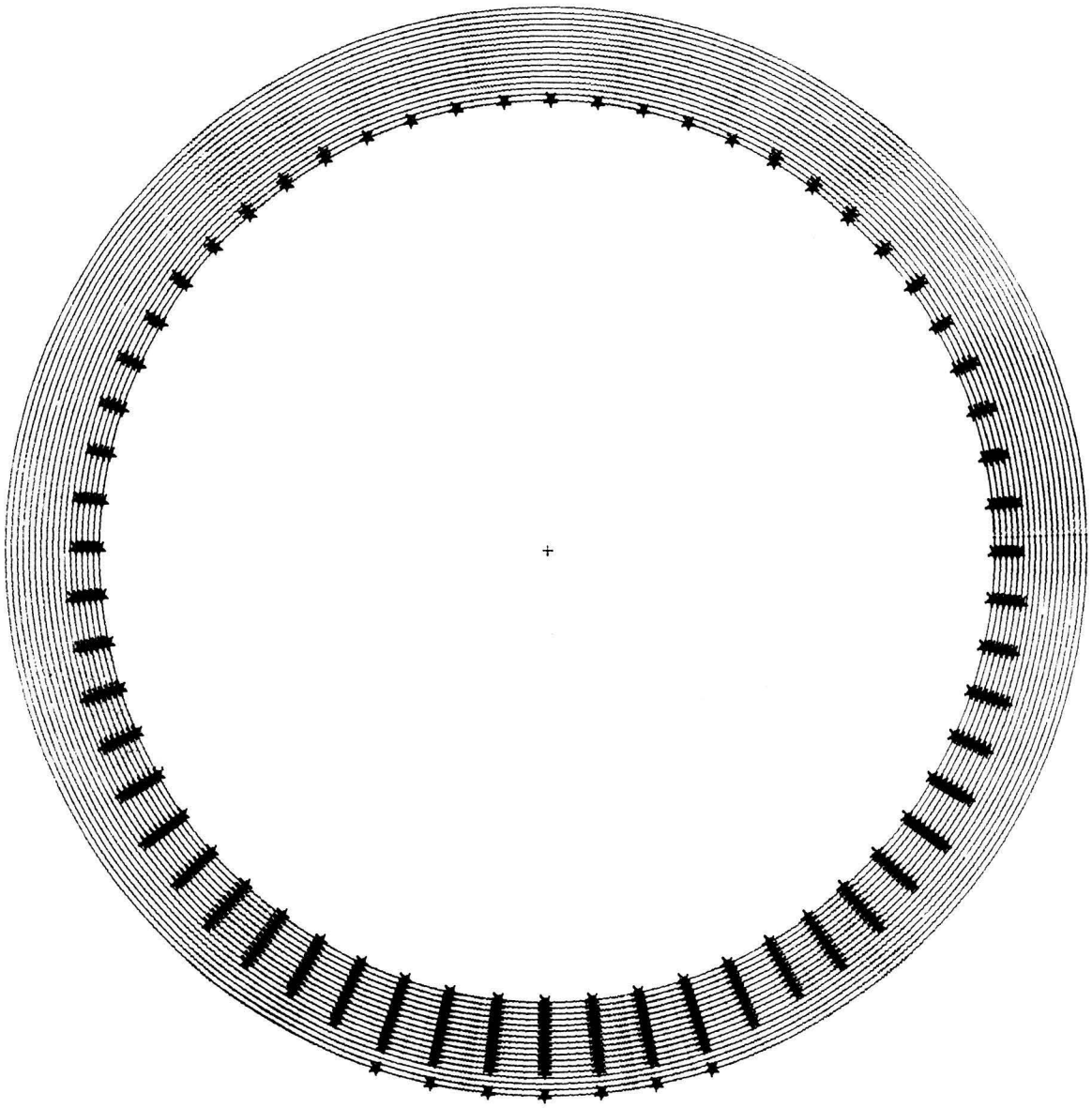

Figure 5.3: Nodes (circles) and contact points (stars) for the analysis of the nonlinear portion of the base plate of the tank tested by Clough and Niwa (1979). [13ft water depth, 6.45° tilt, open top] Each star indicates a discrete Winkler spring in compression.

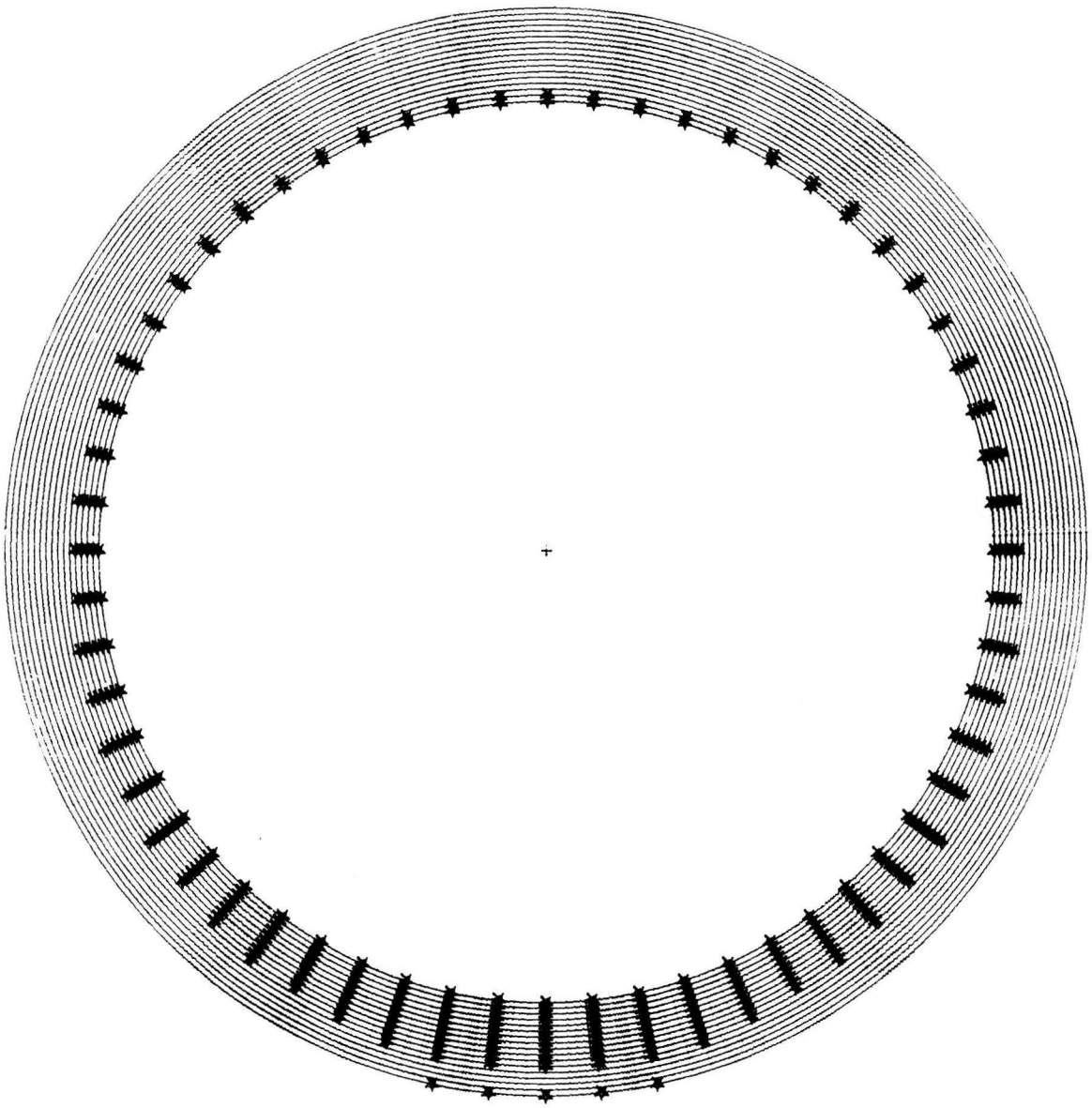

Figure 5.4: Nodes (circles) and contact points (stars) for the analysis of the nonlinear portion of the base plate of the tank tested by Clough and Niwa (1979). [13ft water depth, 6.45° tilt, closed top] Each star indicates a discrete Winkler spring in compression.

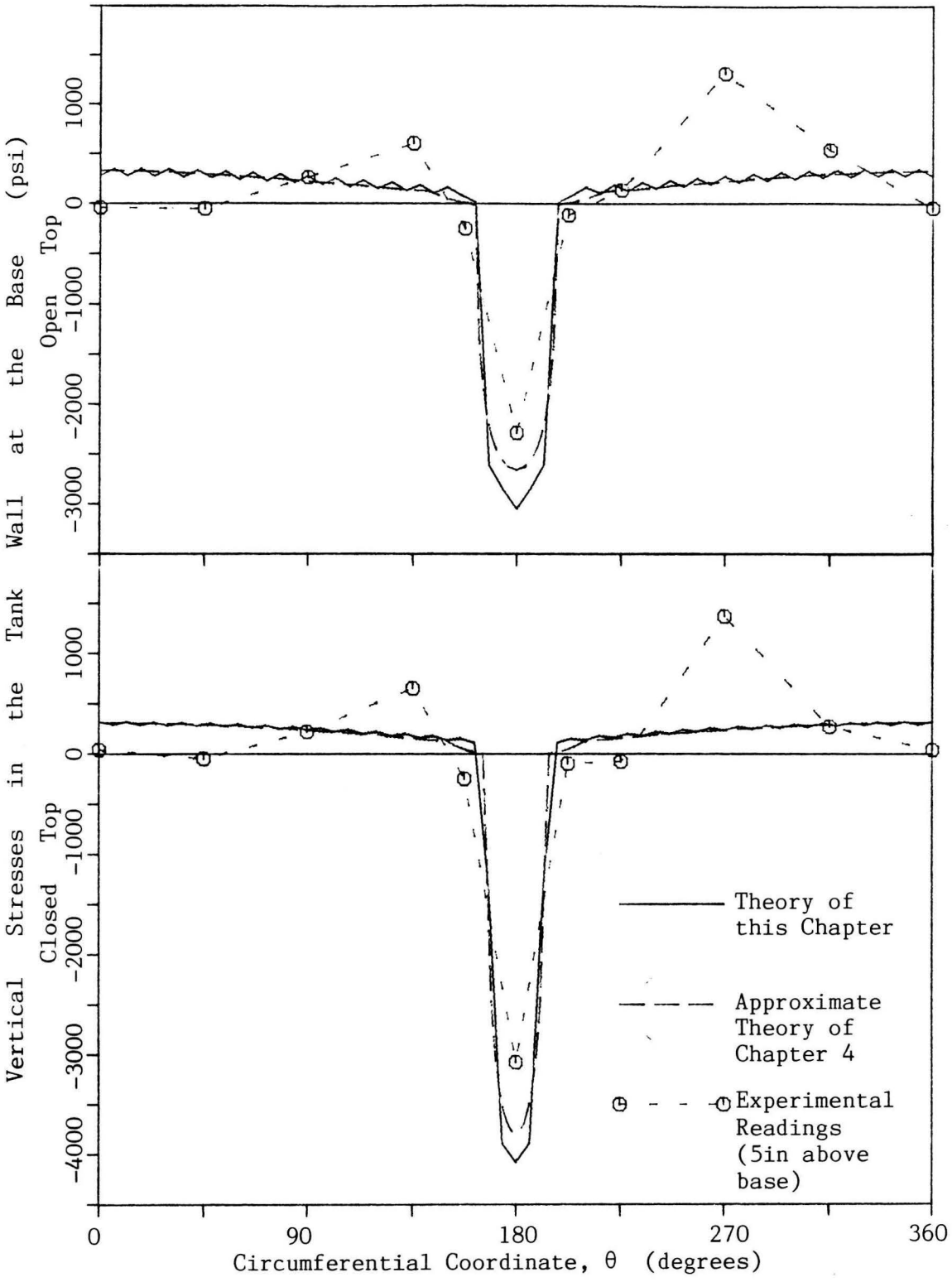


Figure 5.5: Comparison of vertical stresses at the base for the tilt test by Clough and Niwa (1979). [13ft water depth, 6.45° tilt]

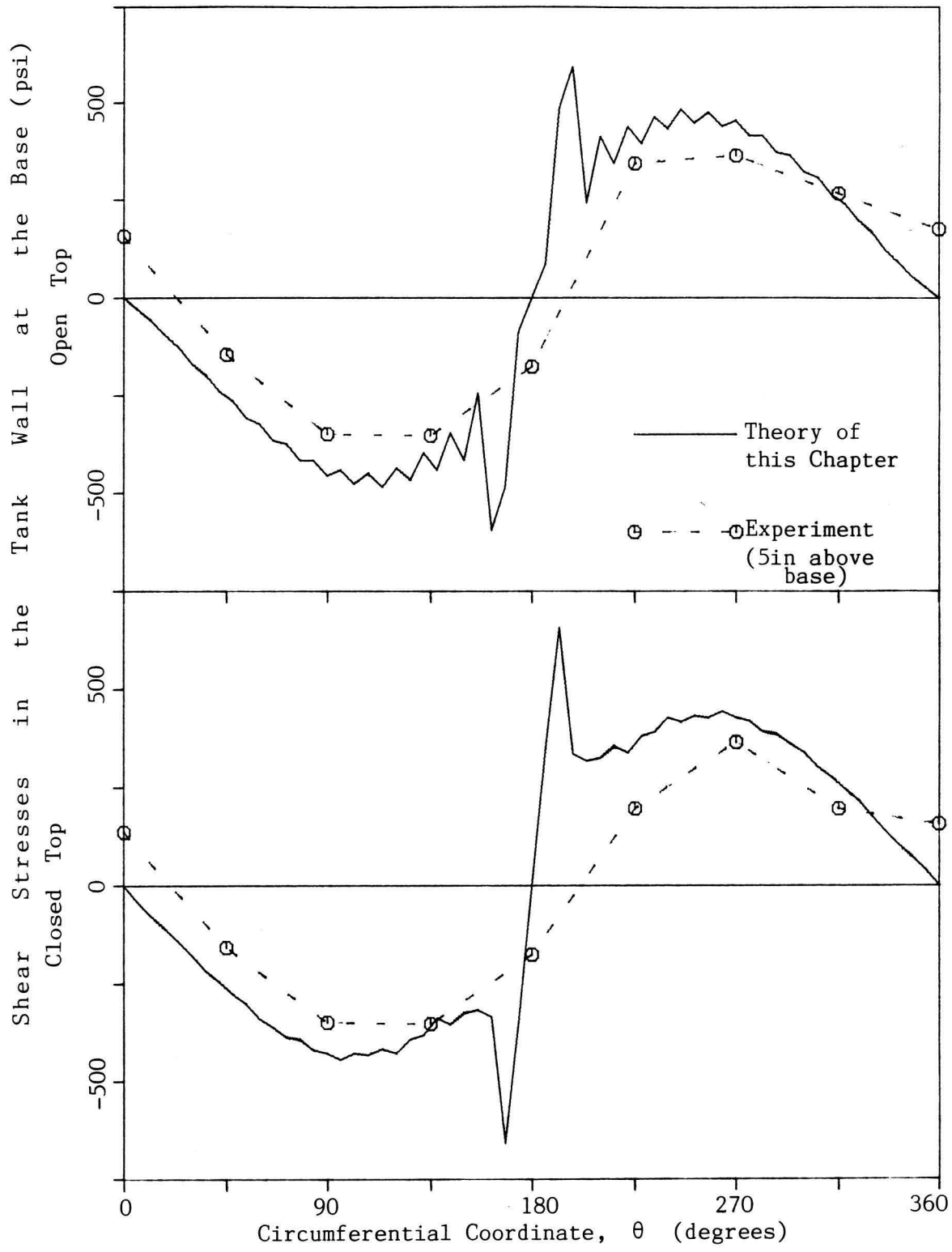


Figure 5.6: Comparison of shear stresses at the base for the tilt test by Clough and Niwa (1982). [13ft water, 6.45° tilt]

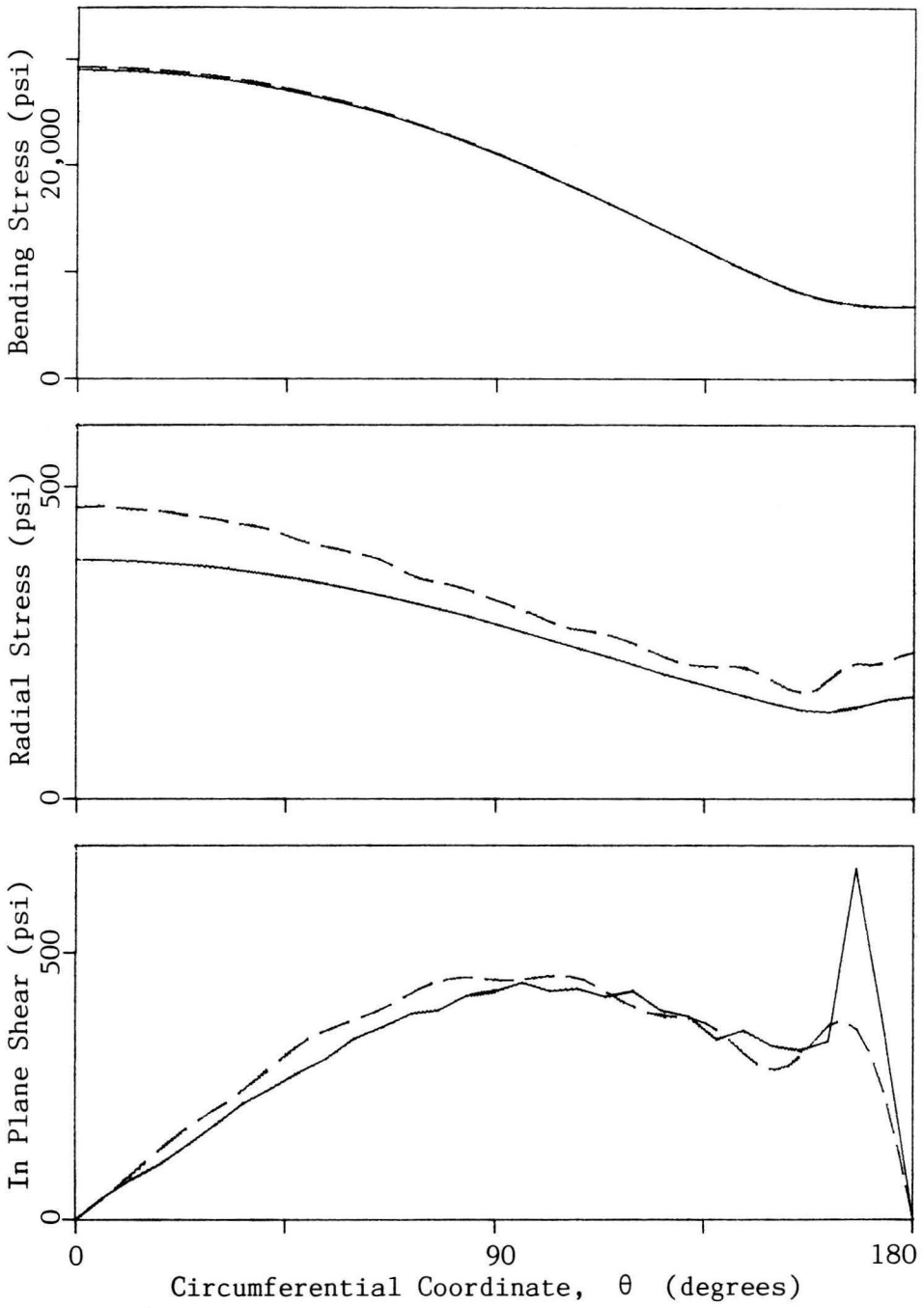


Figure 5.7: Stresses at the junction between the base plate and shell for the tank tested by Clough and Niwa (1979). [closed top, 13ft water, 6.45° tilt] Dashed lines show the stress in the base plate. The continuous lines show the corresponding stress acting on the shell. The mismatch is partly due to discretization error, and partly due to the force carried by the $0.18in^2$ circumferential stiffener, which models the 2in overlap of the base plate beyond the shell wall.

The vertical stresses at the base are in good agreement with those from the approximate analysis. The peak compressive stress also agrees with the experimental result, but the small stress at $\theta = 0$ and large tension at $\theta = 90^{\circ}$ and $270^{\circ}$ observed in the experiment are not matched by the theory.

The sharp peaks in shear stress near $\theta = 180^{\circ}$ (Fig. 5.6) appear to be associated with the large rate of change in the vertical compressive stresses. Similar sharp peaks were obtained in the approximate analysis of Chapter 4 with N = 100 for the number of Fourier harmonics. This suggests that these peaks are not due to discretization error, but arise from some other cause. On the other hand, choosing NH = 12 does not allow circumferential displacements at the base which have Fourier components of order $n \geq 13$. Such displacements could release some of the stress associated with the peaks. Thus, while the peaks exist, the analysis may exaggerate them somewhat.

The experimental shear stresses were measured 5 in above the base. It seems likely that at this elevation the sharp peaks would barely be noticeable. Even if the peaks were present 5 in above the base, not enough measurements were taken to detect them. Finally, although the peaks are remarkable, the stress levels are still low compared to the vertical compressive stresses.

The vertical displacements at the edge (Table 5.1) are a little larger than those from the approximate analysis of Chapter 4, but still significantly smaller than the experimental displacements. In order to examine to what extent these differences might be due to plasticity and

the flexibility of the gasketed joint in the base plate (Detail D in Fig. 4.3), the analysis is repeated with the following assumptions:

(i) The base plate material is elastic-perfectly plastic with a yield stress uniaxial tension of 12 ksi. This corresponds to a yield stress of 36 ksi for the hypothetical steel prototype.

(ii) The gasketed joint in the base plate is perfectly flexible. To balance the lateral component of force which the shell exerts on the base plate, a shear force which varies like sin $\theta$ in the circumferential direction is applied at the inside edge of the outer annular portion of the base plate.

For this modified analysis, the nonlinear portion of the base plate extends inward from the edge to the gasketed joint. The tilt angle was increased gradually to Clough and Niwa's (1979) "standard" tilt angle of $6.45^{\circ}$. Then, in order to examine the effects of residual plastic strains resulting from previous loading of the tank, the tilt angle is increased to $8.5^{\circ}$ (the largest tilt angle for which Niwa and Clough (1979) report results) and reduced again to the standard tilt of $6.45^{\circ}$. The analysis is performed with NN = 21, NW = 5, NH = 4, NC = 6 which is judged sufficient for accurate values of the n = 0 and n = 1 Fourier coefficients of the displacements. Results (Table 5.1), lines 5, 6, 10 and 11) indicate that plasticity in the base plate and the flexibility of the gasketed joint increases the n = 0 and n = 1 coefficients for the uplift by a factor of 1.4. Loading to a tilt angle of $8.5^{\circ}$ and unload-

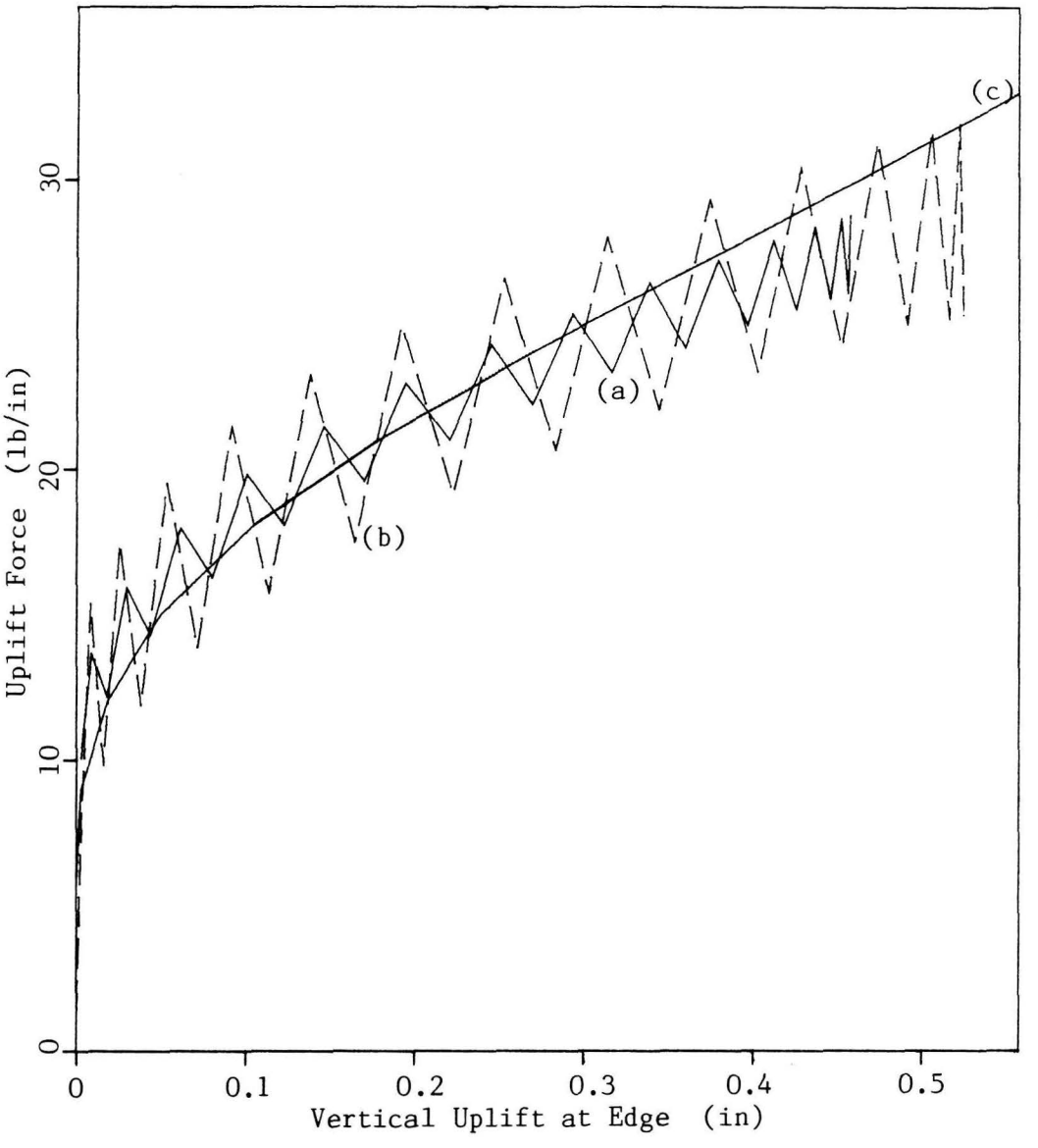


Figure 5.8: Relationship between the uplift force applied at the edge (base plate shear plus vertical component of radial membrane force) and uplift for the tall tank tested by Clough and Niwa (1979).
(a) non-axisymmetric solution, closed top, $6.45^{o}$ tilt
(b) non-axisymmetric solution, open top, $6.45^{o}$ tilt
(c) axisymmetric solution

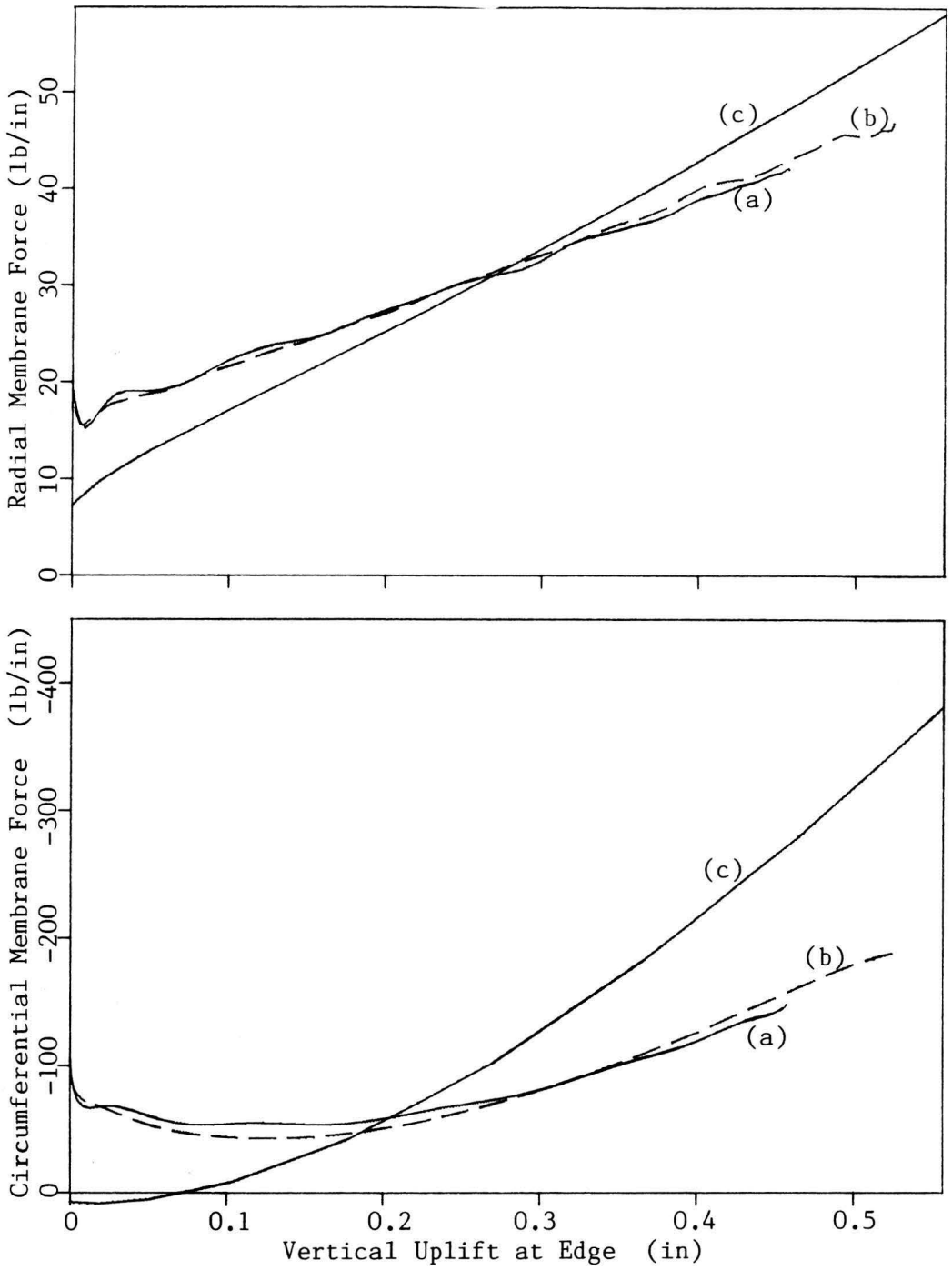


Figure 5.9: Relationship between membrane forces in the base plate at the edge and the vertical uplift at the edge for tall tank tested by Clough and Niwa (1979).
(a) non-axisymmetric solution, closed top, 6.45° tilt
(b) non-axisymmetric solution, open top, 6.45° tilt
(c) axisymmetric solution

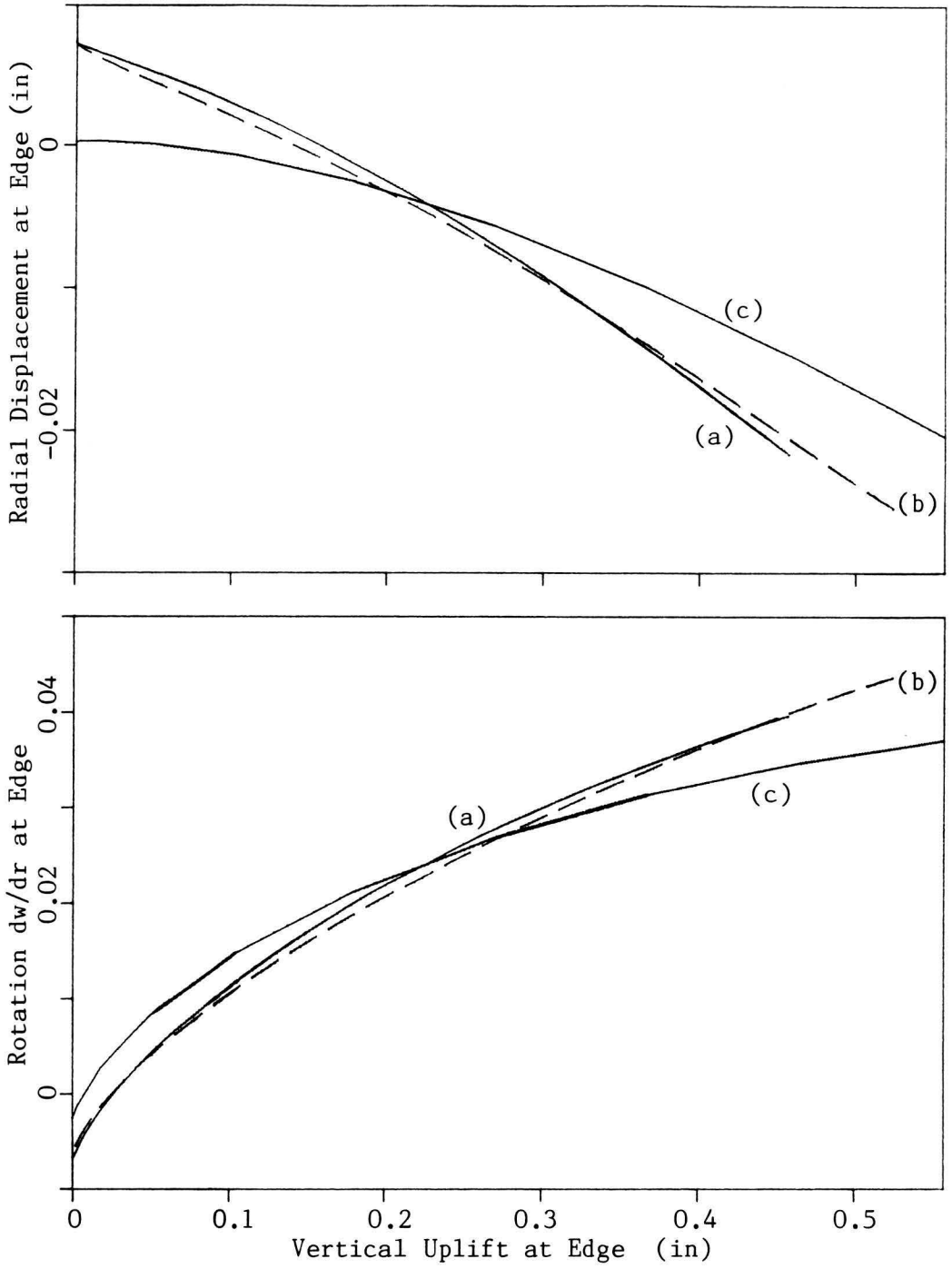


Figure 5.10: Relationship between vertical displacement, radial displacement and rotation at edge for tall tank tested by Clough and Niwa (1979).

(a) non-axisymmetric solution, closed top, 6.45° tilt
(b) non-axisymmetric solution, open top, 6.45° tilt
(c) axisymmetric solution

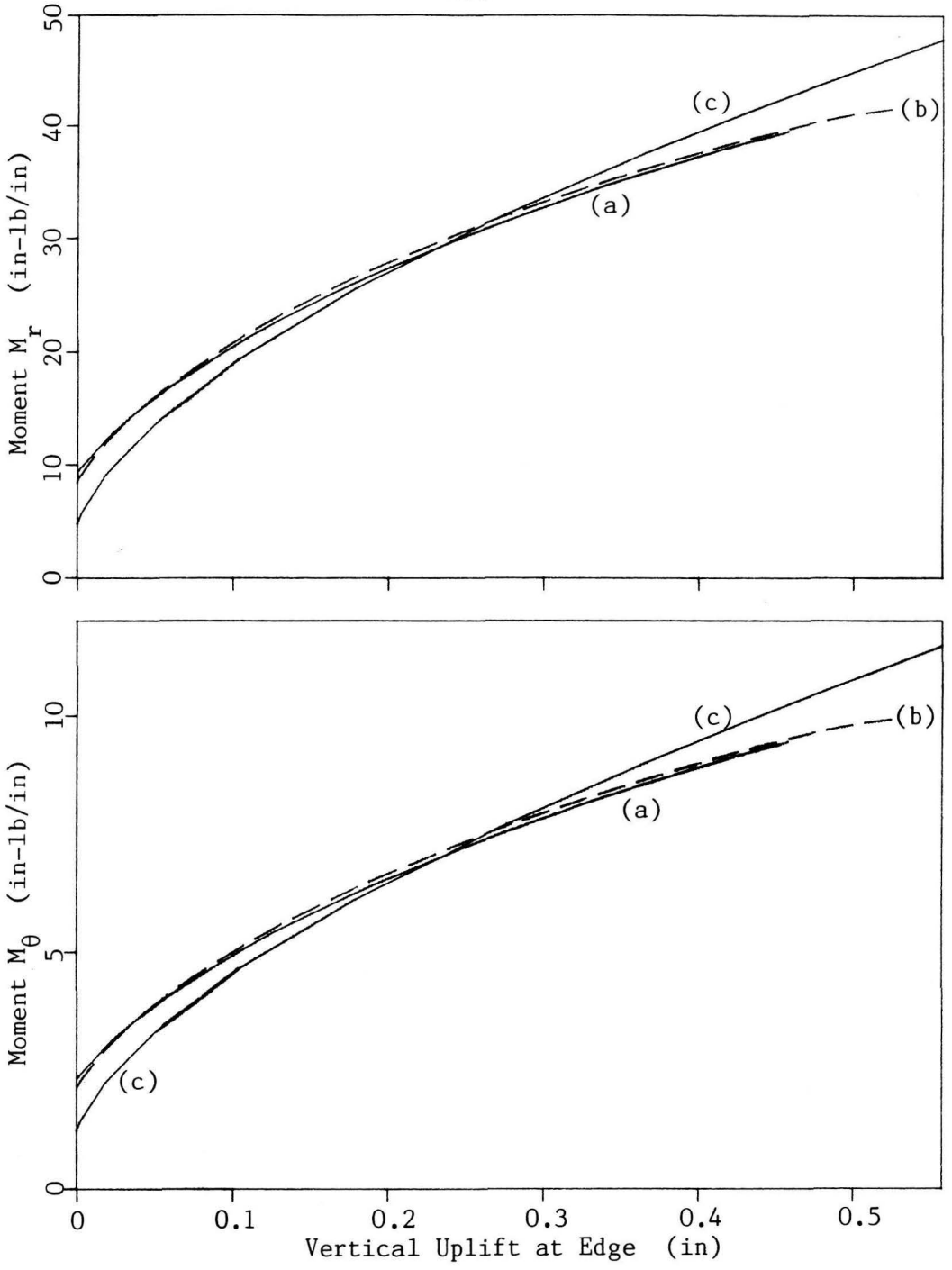


Figure 5.11: Relationship between bending moments in the base plate at the edge, and uplift for the tall tank tested by Clough and Niwa (1979).

(a) non-axisymmetric solution, closed top, $6.45^{o}$ tilt
(b) non-axisymmetric solution, open top, $6.45^{o}$ tilt
(c) axisymmetric solution

ing further increases the n = 0 and n = 1 coefficients of the uplift by a factor of 1.3 to 1.4. Including all these effects results in n = 0 and n = 1 Fourier coefficients of the uplift which are reasonably close to the experimental values.

The comparison between the results from the comprehensive analysis of this chapter and the approximate method of Chapter 4 serve to evaluate the assumption of weak circumferential variations. In Figs. 5.8 to 5.11 this assumption is examined more closely by looking at the relationship between the vertical uplift and various quantities of interest. An example of such a quantity of interest is the vertical uplifting force acting on the base plate at the edge. This uplift force is also equal to the vertical tension in the shell wall. For a given tilt angle, the values of the uplift force and the vertical uplift can be sampled at various points around the circumference for which some uplift occurs, and plotted, as in Fig. 5.8, lines (a) and (b). If the circumferential variations are indeed weak, this relationship between the uplift force and the vertical uplift should coincide identically with that from the axisymmetric solution [Fig. 5.8, line (c)]. As can be seen, the agreement for this case is fairly good.

Figures 5.9 to 5.11 are similar plots for other quantities of interest. Perhaps the plot which best reveals how the assumption of weak circumferential variations might break down is the one for the circumferential membrane force, $N_\theta$, at the edge (Fig. 5.9). It appears that the large circumferential compression that might be expected from the axisymmetric solution where the uplift is a maximum redistributes to

other points on the circumference. As a result of this circumferential spreading of the compressive force $N_\theta$, the axisymmetric solution overestimates the circumferential compression where the uplift is a maximum, but where the uplift is small and the circumferential compression exceeds that from the axisymmetric solution.

For reasons explained in Chapter 2, the circumferential compression at the edge determines to a large extent how much membrane action is present in the base plate. For small circumferential compression at the edge, there is little membrane action, and a smaller uplift force is required for a given amount of uplift. Hence, the circumferential spreading of the circumferential compression should decrease the uplift force for large values of uplift and increase it for small values of uplift. This is what is observed in Fig. 5.8.

### 5.6.2 Broad Tank Tested by Manos and Clough (1982)

The description of this tank and the assumptions made in modeling it can be found in Section 4.2.3.2. Results are shown in Figures 5.12 and 5.13. It is seen that in this case relaxing the assumption of weak circumferential variations in the base plate increases the vertical uplift by a factor of more than 2. One reason for this might be that flexible inextensional modes in the shell wall make a distribution of vertical uplift at the edge possible, for which relatively little membrane action is developed in the base plate.

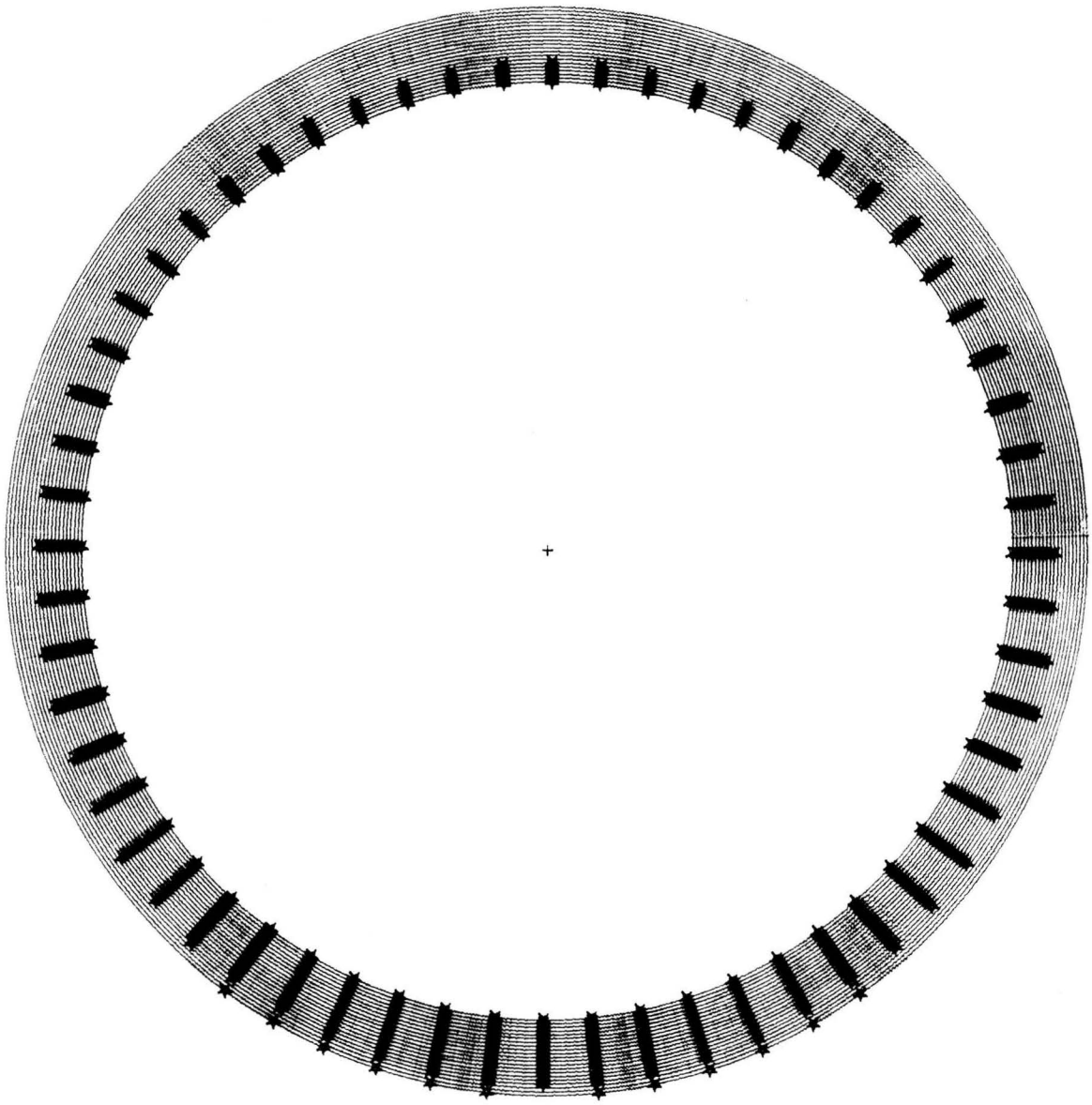

Figure 5.12: Nodes (circles) and contact points (stars) for the analysis of the nonlinear portion of the baseplate for the tank tested by Manos and Clough (1982). [5ft water depth, 16$^{o}$ tilt, open top] Each star indicates a discrete Winkler Spring in compression.

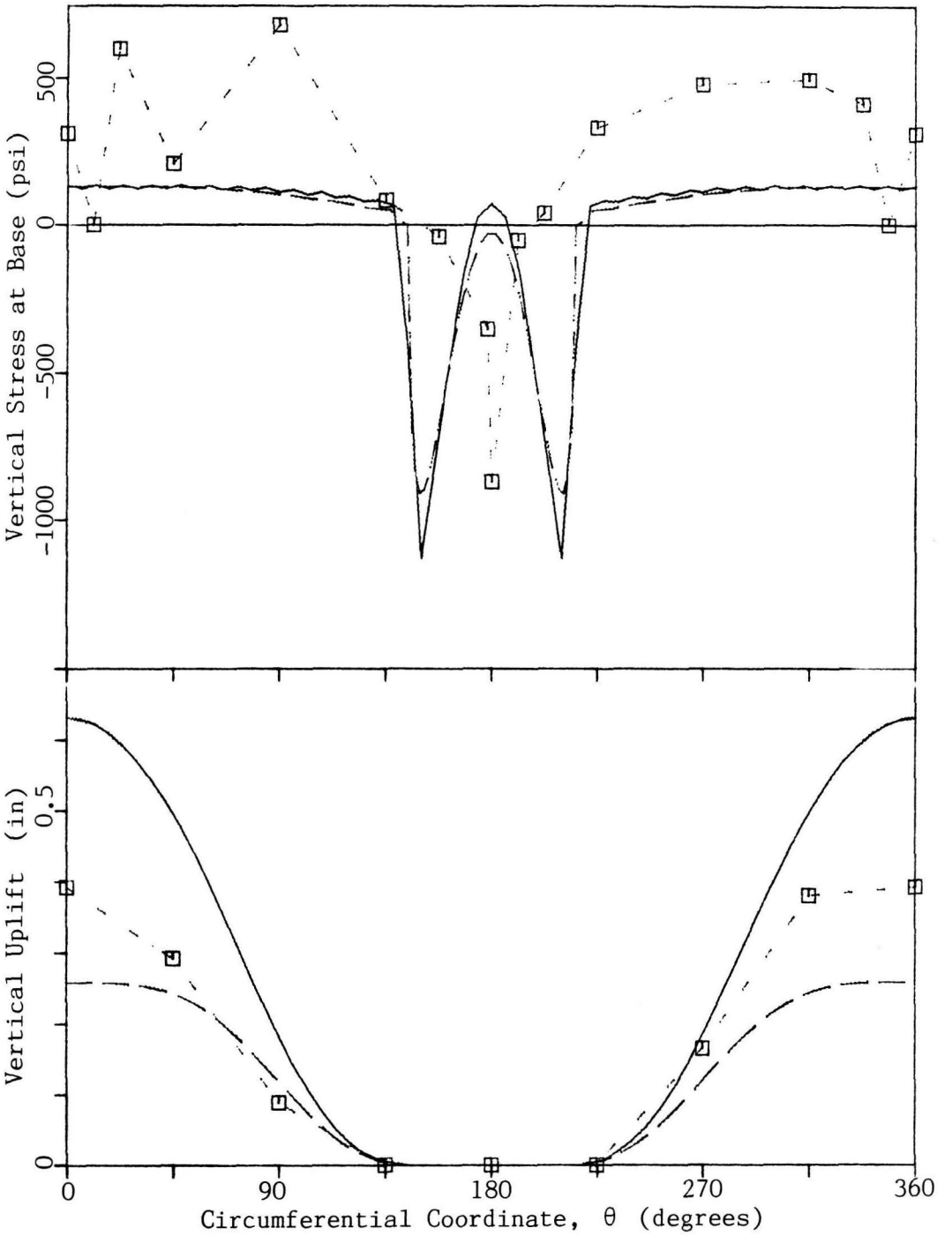


Figure 5.13: Comparison of Results from the analysis in this Chapter (continuous line), the approximate analysis of Chapter 4 (dashed line), and the experimental readings (markers joined by a dashed line) for the broad aluminum tank tested by Manos and Clough (1982). [5ft water depth, $16^{o}$ tilt, open top]. The experimental data are used with the authors' permission.

Another contributing effect is that, where the base plate uplifts the most, the fluid pressure is reduced due to tilting. This applies especially to broad tanks because

a) For a given tilt angle, the change in pressure due to tilting is a larger fraction of the pressure at zero tilt.

b) A larger tilt angle is required to generate a given overturning moment.

This effect is included in the analysis of this chapter, but not in the approximate analysis of Chapter 4.

The breakdown of the assumption of weak circumferential variations is confirmed in Fig. 5.14, where the uplifting force for larger values of the uplift is seen to be much smaller than would be expected from the axisymmetric solution.

Given the large change in the vertical uplift that occurs upon relaxation of the assumption of weak circumferential variations, it is remarkable that the distribution of vertical stresses hardly changes. It still exhibits the bimodal distribution of compressive stresses which is not seen in the experimental data. The analysis even indicates that the shell wall uplifts at $\theta = 180^{\circ}$. As was explained in Section 4.2.3.2, this is consistent with what might be expected from the inextensional shell theory. Although the experimental vertical stresses do not confirm this, the measured radial displacements at the top rim do give an indication that there may be some tendency for uplift at $\theta = 180^{\circ}$. To see this, note that if there is uplift at $\theta = 180^{\circ}$, then

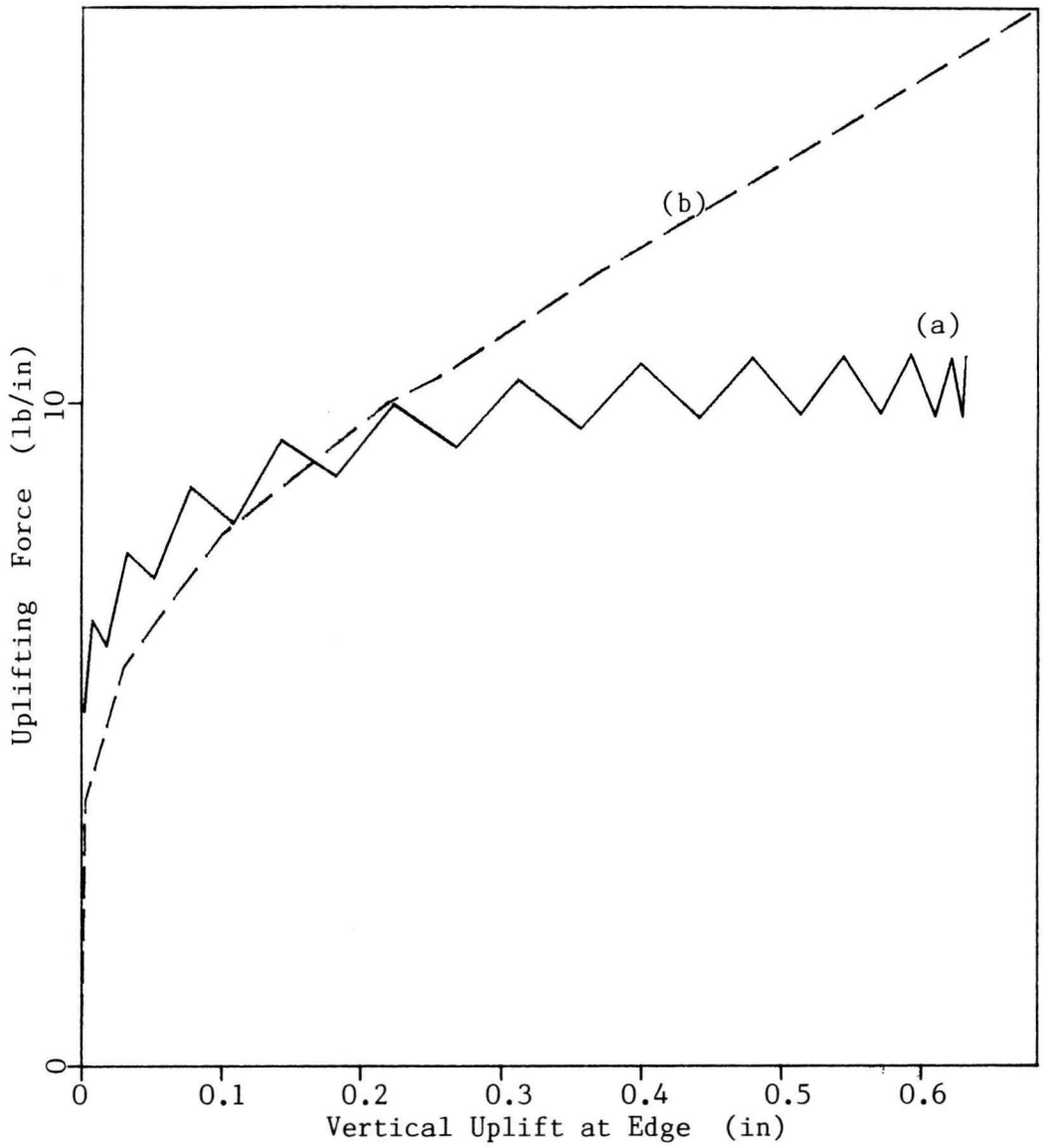


Figure 5.14: Relationship between vertical uplift at the edge, and the vertical uplifting force for the broad tank tested by Manos and Clough (1982)

(a) non-axisymmetric solution, open top, $16^{o}$ tilt

(b) axisymmetric solution

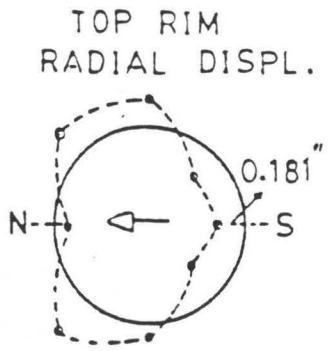


Figure 5.15: Top rim radial displacements. Reproduced from Fig. 5.2.1 in Manos and Clough (1982) with the authors' permission. [5 ft water depth, 16° tilt, rigid foundation, open top].

it is expected that the uplift at $\theta = 180^{\circ}$ is a local maximum. This means that the second derivative of the uplift with respect to $\theta$ (denoted by $U^{\cdot\cdot}$ in Chapters 3 and 4) is negative. From Eq. 3.6c it is seen that the radial displacement must therefore be negative, i.e., inwards. This is exactly what is shown in Fig. 5.15. Although Eq. 3.6c applies for inextensional tanks only, the argument is still relevant, because for a broad, roofless tank such as this one, inextensional deformation modes play an important role.

### 5.6.3 Mylar Tank Tested by Shih (1981)

In his Figure 5.7, Shih (1981) gives the results of a static tilt test on an unanchored mylar tank. The tank used is 5 in in diameter, 10.5 in tall, and the thickness is 0.002 in for both the base plate and the shell. A stiffening rim was provided which essentially prevents out-of-round

deformations at the top. For the analysis, the same effect is achieved with a 0.02 in thick, flat mylar roof. Shih set the tank on a tilt table at a constant tilt angle of $10.3^{\circ}$ and gradually filled it with water, measuring the vertical uplift[1] and the width of the uplifted strip of the base plate.[2]

In modeling the tank, the elastic properties for mylar are taken to be $E = 0.735 \times 10^6$ psi for Young's modulus, and $\nu = 0.3$ for Poisson's ratio. Sliding of the tank is prevented by horizontal Winkler springs of stiffness $10^3$ lb/in$^3$ on a 2 in diameter circle at the center of the tank. The stiffnesses for the vertical springs are taken to be $k_o = 3{,}446$ lb/in$^3$ under the base plate, and $k_e = 516{,}900$ lb/in$^2$ at the edge.

The radial spacing of the nodes in the nonlinear portion of the base plate is 0.05 in. The analysis is performed with NW = NH = 3, NC = 4. This is sufficient to obtain accurate values of the uplift.

In the analysis, the loading process by filling of the tank is simulated by computing the appropriate load vector at each loading step. This means that the water level increases from one loading step to the next. As a result, the stiffness matrix of the shell also changes due to the nonlinear effects associated with the hydrostatic pressure. For simplicity, such changes in the stiffness matrix of the shell are not included in the analysis. Instead, the stiffness matrix of the shell is

---

1 With feeler gauges.

2 By inserting dye under the uplifted portion of the base plate, the extent of the uplifted portion became clearly visible.

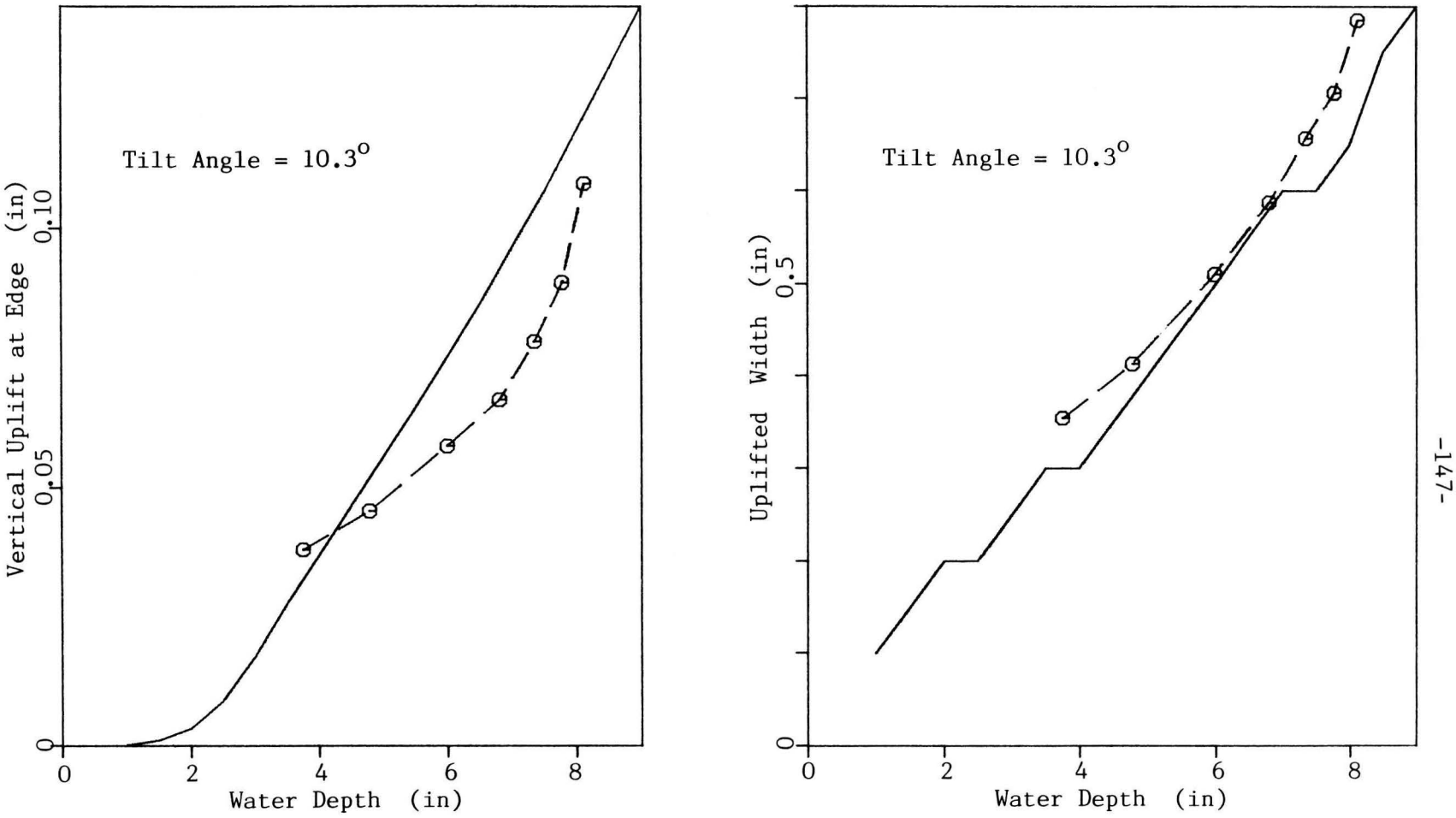


Figure 5.16: Comparison of theoretical results from the non-axisymmetric analysis (continuous line) with experimental readings (joined by dashed lines) obtained from Shih (1981) with his permission.

computed for a water depth of 6.5 in and assumed to remain constant.

The analytical results are compared with Shih's experimental readings in Fig. 5.16. The agreement is acceptable, if one considers the uncertainty in measuring the displacement with feeler gauges. Some of the differences between theory and experiment may also be due to the stiffening effect of a bead of epoxy used to bond the shell to the base plate.

## 5.7 SUMMARY AND CLOSING REMARKS

The comprehensive method of analysis developed in this chapter enables the assumption of weak circumferential variations in the base plate to be relaxed. In doing so it is seen that for a tall tank, this assumption is acceptable. For a broad, roofless tank, however, the assumption seems to be acceptable for calculating the distribution of vertical stresses in the shell at the base, but not for calculating the uplift.

Significant differences between theoretical and experimental results remain, even after relaxing the assumption of weak circumferential variations in the base plate. Exactly why these discrepancies occur is not clear. However, a number of possible explanations can be suggested and evaluated.

Due to its high thermal conductivity, aluminum is difficult to weld. Therefore, some imperfections and residual stresses are inevitable. There may also be some additional residual stress from forming of the aluminum sheet. Whereas for the linear behavior of a structure, the

changes in stresses due to external loading are unaffected by residual stresses, this does not apply for the base plate of a tank, for which the behavior is markedly nonlinear. In particular, it seems likely that there were some residual circumferential tension due to welding at the shell-base plate joint. This tends to reduce the membrane action in the base plate, resulting in larger uplift for a given tilt angle.

It was seen that for the tall aluminum tank, yielding of the aluminum, and the flexibility of the gasketed joint in the base plate have a strong influence on the uplift. The broad aluminum tank did not have a gasketed joint, but its behavior may have been affected by yielding of the aluminum at the time the tilt test was performed, or by residual plastic strains resulting from previous loading of the tank.

Some important effects may have been lost in the linearized formulation for the shell. It would appear, for example, that the relatively sharp peaks in the distribution of compressive stresses at the base may be redistributed by the geometric shortening that occurs when a vertical line on the shell wall becomes a curve. This would result in a somewhat lower peak compressive stress.

Finally, friction between the base plate and the foundation is not considered in the analysis. Such friction forces can change the distribution of membrane forces in the base plate. This in turn may affect membrane action in the uplifted portion of the base plate.

In summary, there are several possible reasons for the differences between the theoretical and experimental results. What is not clear is exactly what effects are responsible for the differences in each case.

Resolving this would require improved capabilities for analysis, including a fully nonlinear formulation for the shell, in conjunction with carefully designed experiments.

## 6. THE PREUPLIFT METHOD

For an unanchored tank, uplift is necessary so that the earthquake induced overturning moment can be balanced by the weight of the fluid resting on an uplifted portion of the base plate. Thus uplift enables the weight of the water to participate in stabilizing the tank. However, uplift also can result in damage to connecting pipes or buckling of the shell wall due to the concentration of vertical compressive stresses at the base.

The question that comes up naturally in this context is: Is it possible to reap the benefits of uplift (stabilization by the weight of the fluid resting on an uplifted portion of the base plate) without incurring its detrimental effects? This can indeed be achieved, if the tank wall is preuplifted all around its circumference by a ring filler, as shown in Fig. 6.1.

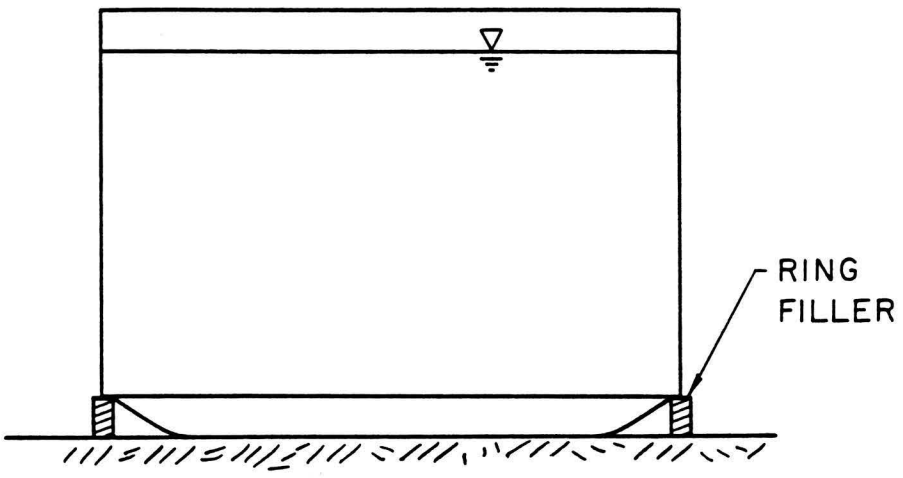


Figure 6.1: A preuplifted tank.

The ring filler is designed in such a way that it carries not only the weight of the tank wall and roof, but also the weight of part of the fluid which rests on the preuplifted portion of the base plate. For uplift to occur, this preload on the ring filler must be overcome by the seismically-induced vertical tension in the shell wall. Thus, for light to moderate ground shaking the tank wall remains in contact with the ring filler all around its circumference, and the tank behaves essentially as if it were anchored even under shaking that would otherwise cause substantial uplift. Furthermore, it will be seen that even under ground shaking strong enough that the tank wall locally looses contact with the ring filler (i.e., major amounts of uplift), preuplift improves the performance of the tank for any given lateral load. This conclusion is supported by experimental and theoretical results. First the experiments and method of analysis are described, then the results presented in the figures are discussed.

## 6.1 EXPERIMENTS

A mylar tank was fabricated following the methods of Shih (1981): The vertical seam in the tank wall was lapped and bonded with 1/4" wide double sided tape. At the junction between the shell wall and the base plate (henceforth referred to as the edge), a thin bead of epoxy was used as a bonding agent. At the top, a lucite ring prevents any out-of-round deformations of the cross section.

The dimensions for the model tank are 5" for the diameter, 9-7/8" for the height, and 0.002" for the thickness of both the tank wall and

Figure 6.2: Experimental setup for tilt tests on a mylar tank.

Figure 6.3: Buckling of an unanchored mylar tank.

the base plate. Since the modulus of elasticity for mylar, 735,000 psi ±9% as quoted by Shih (1981) from Weingarten, et al. (1960), is a factor of 40 less than that for steel, the model tank satisfies the conditions of similarity with a steel tank 40 times larger. This means that the hypothetical steel prototype is 16'-8" in diameter, 32'-11" tall, and both the tank wall and the base plate are 0.08" thick. This shell thickness is close to the minimum that would be required to support the hydrostatic water pressure, if the tank were full.

The test setup is shown in Fig. 6.2. A static lateral load was induced by tilting the specimen on a tilt table which was designed for calibrating accelerometers. In doing so, the vertical lap joint in the shell was oriented on the axis of loading, opposite to the region of vertical compression. Two types of tests were performed:

(i) The tank was filled with water to a depth of 4-9/16" at zero tilt, and the tilt angle was increased in increments of about $3^{o}$, measuring the maximum uplift at each increment with feeler gauges (results in Fig. 6.5).

(ii) The tilt angle was held fixed, and the tank was filled slowly through the aluminum tube visible in Fig. 6.2, until the first signs of a buckle (much smaller than the one shown in Fig. 6.3) could be detected visually, using light reflected on the tank wall. The water levels at buckling are shown in Fig. 6.7 for various tilt angles. Each experimental point is the average of two readings.

In the buckling tests, the first buckle always formed near the base, at the axis of loading. If the water level was increased further, the buckle gradually increased in size and more buckles formed (as in Fig. 6.3). This agrees with Shih's (1981) observation that unanchored tanks do not collapse for water levels significantly higher than the water level at which the first buckle can be detected. However, in contrast to Shih (1981), who measured collapse water levels, here all experimental data relate to incipient buckling. The author considers this to be a more appropriate failure criterion, because mylar tanks probably owe much of their post buckling strength to the fact that the mylar does not yield at stress levels which, when scaled to prototype stresses, are well above the yield stress for the mild steels out of which tanks are typically made.

All tests were performed with and without preuplift. The ring filler consists of a 1/32" thick square sheet of plexiglass with a hole whose diameter is a few hundredth of an inch less than the inner diameter of the tank. This insures that the entire circumference of the tank wall is supported by the filler even if there is a small error in centering the filler.

To prevent slipping of the tank it was bonded to its foundation at the center by a 1/4" square piece of double sided tape.

## 6.2 ANALYSIS

From Chapter 5, for the tall aluminum tank tested by Clough and Niwa (1979), the results from the comprehensive method of analysis are

in close agreement with those from the approximate analysis method described in Chapter 4. The theoretical maximum compressive stresses also agree with the experimental results. Since the mylar tank under consideration in this chapter has about the same height to diameter ratio as the tall aluminum tank of Chapter 5, the approximate method of analysis is used. For the case with preuplift, the vertical uplift varies gradually around the circumference, therefore the accuracy of the approximate method may be expected to be better for the case with preuplift.

Consider the problem of the tank for which the base plate has been replaced by a ring of nonlinear Winkler springs. The force per unit length-deflection relationship for such springs is shown schematically in Fig. 6.4. For a tank without preuplift, the applicable curve is ABCD. The segment BCD of this curve is obtained from the axisymmetric uplift solution, and segment AB is taken to be linear, with a slope $k_e$ that is representative of the stiffness of the foundation in compression. In the analysis reported herein a large number, $k_e = 10 \text{lb/in}^2$, is used to simulate a rigid foundation.

Preuplift can be accounted for simply by modifying the force-deflection relation of the Winkler springs. In this case the force-deflection relation is represented by curve A'CD in Fig. 6.4, in which the segment A'C is taken to be a straight line of slope $k_e$, representative of the flexibility of the foundation and the ring filler in compression. In the present analyses, the ring filler as well as the foundation are taken to be rigid. Correspondingly, $k_e = 10 \text{lb/in}^2$ is

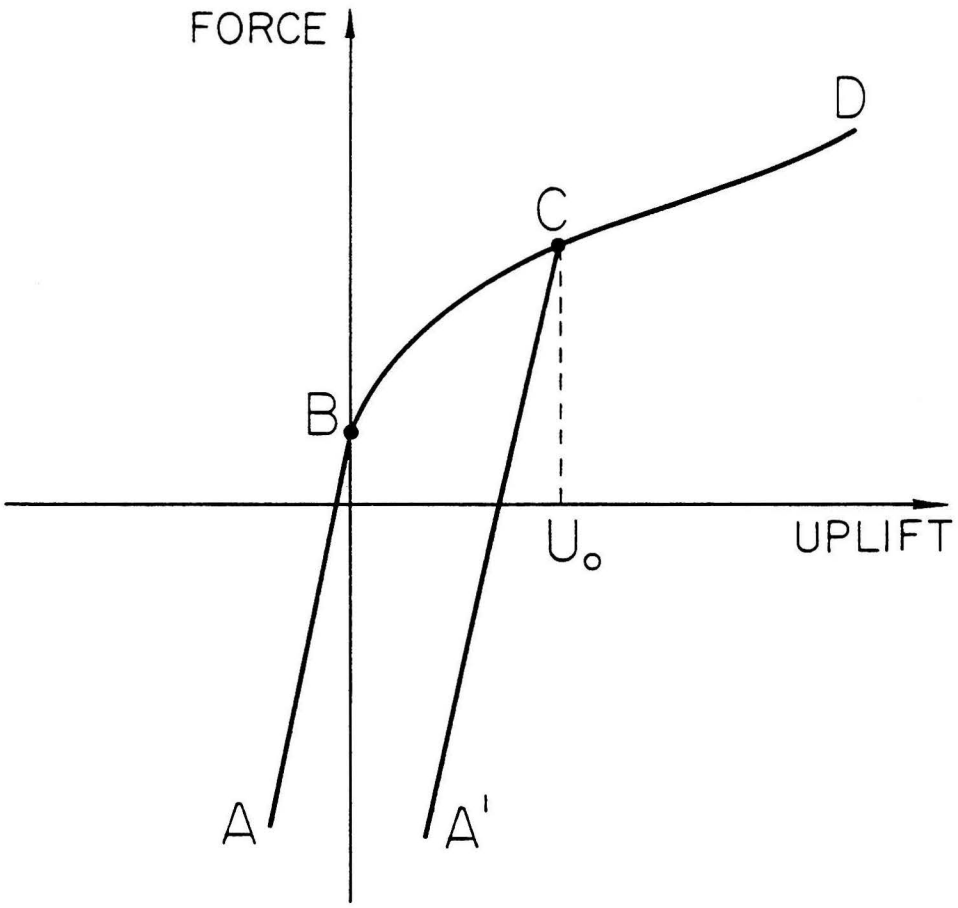


Figure 6.4:
Schematic force-deflection relation for the nonlinear Winkler springs at the base of the tank, without preuplift (curve ABCD), and with preuplift $U_o$ (curve A'CD).

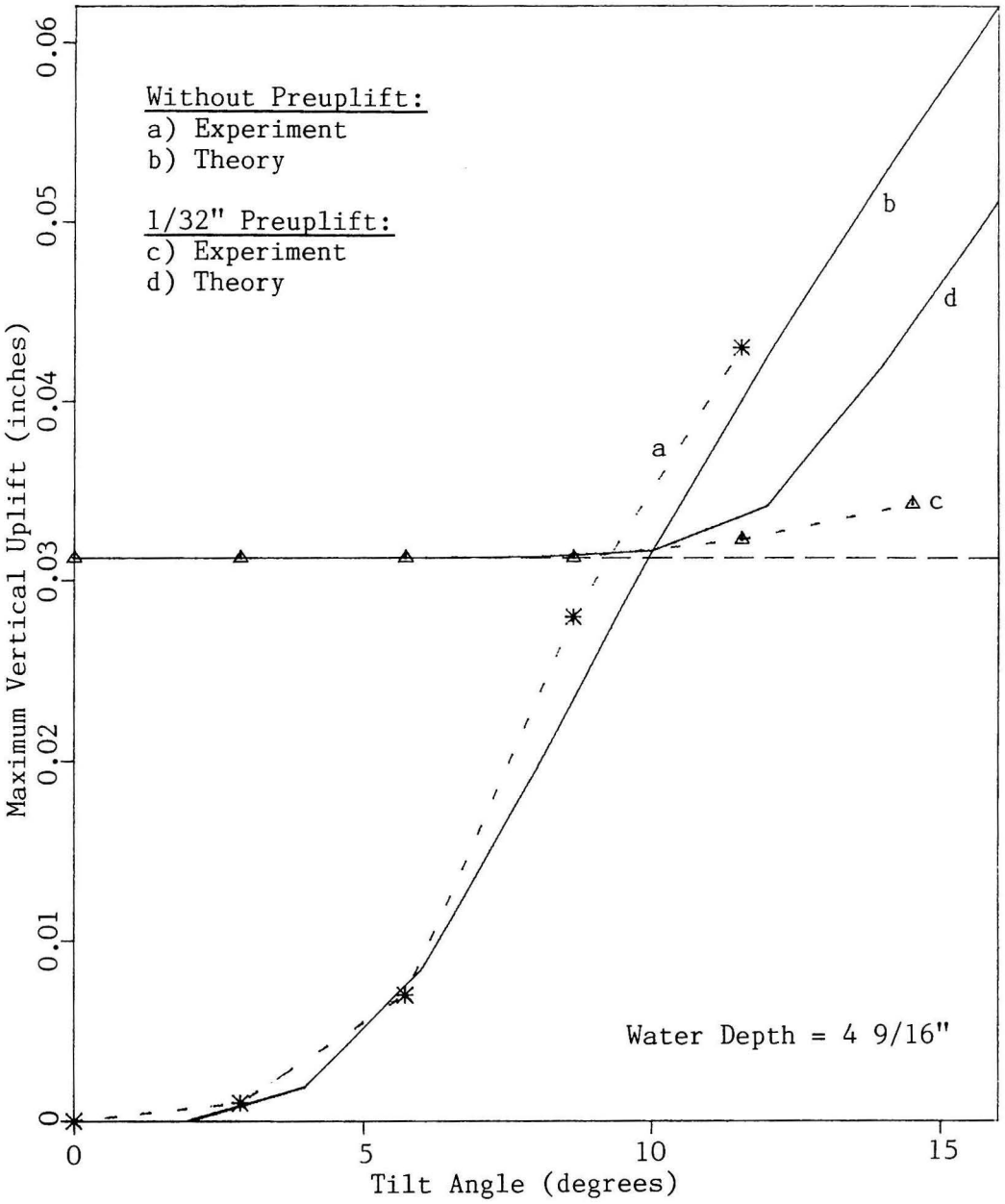


Figure 6.5: Comparison of experimental and theoretical results for the maximum vertical uplift, with or without preuplift. Note: For the preuplifted case, the vertical uplift includes the preuplift.

used, as for the case with no preuplift.

## 6.3 DISCUSSION OF RESULTS

The theoretical and experimental values of the uplift obtained with and without preuplift are shown in Fig. 6.5 as a function of the tilt angle. For the preuplifted case, the uplift shown in Fig. 6.5 includes the preuplift. The uplift due to tilting is much smaller for the preuplifted case. Also, for tilt angles greater than about $10^{o}$, both theory and experiment indicate that the total uplift is less for the preuplifted case.

The agreement between theory and experiment for the case without preuplift is excellent. However, two compensatory effects may have been involved: On one hand it was found that the approximate method of analysis, based on the assumption of weak circumferential variations in the base plate, yields a maximum uplift slightly (10 to 20%) smaller than that from the more comprehensive analysis. On the other hand, the stiffness of the bead of epoxy, which bonds the base plate to the shell, and the stiffness of a small extension of the base plate on the outside of the tank wall were neglected in the analysis.

For the case with preuplift, Fig. 6.5 indicates that uplift due to tilting is less than predicted by the analysis. Perhaps one of the more important contributing factors to this difference is the stiffening effect of the bead of epoxy at the edge. When the tank is uniformly uplifted all around the circumference, the edge tends to move radially inward. Due to the restraining action of the shell and the bead of

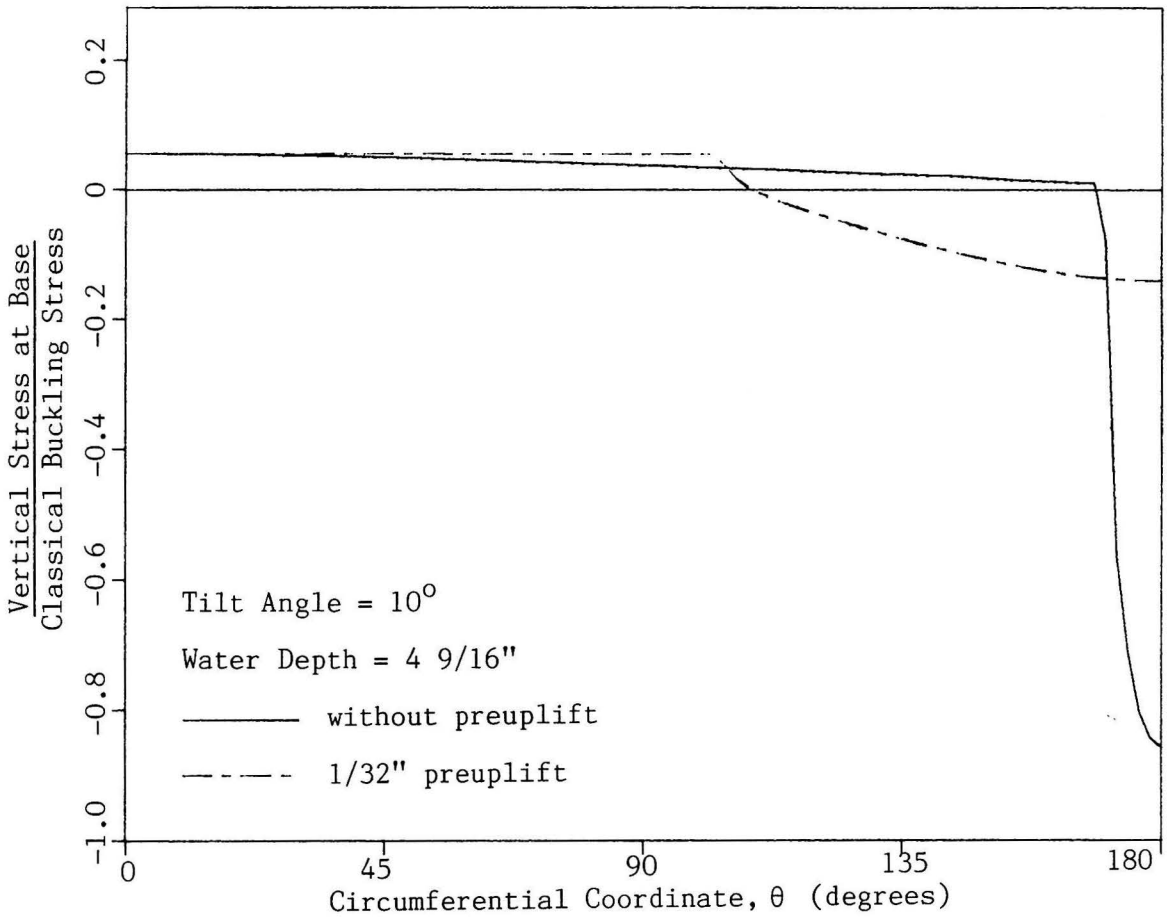


Figure 6.6: Theoretical distribution of vertical stresses in the tank wall at the base.

epoxy, this gives rise to a radial membrane tension in the base plate. For a larger radial tension at the edge, more membrane action is developed in the base plate, and the hold down force for a given amount of uplift is increased. This means that the restraining action due to the axial stiffness of the bead of epoxy will tend to decrease the uplift for a given water level and tilt angle.

The axial stresses at the base, as obtained by analysis, for a water level of 4-9/16" and a tilt angle of $10^{o}$ are shown in Fig. 6.6. The stresses are expressed as a fraction of what is generally referred to as the classical buckling stress [Timoshenko and Gere (1961)], given by

$$f_{CL} = [3(1-\nu^2)]^{-\frac{1}{2}} Et/R \quad , \qquad (6.1)$$

in which E, $\nu$, t, R are Young's modulus, Poisson's ratio, the thickness and the radius of the shell, respectively. The location on the circumference is defined by an angle $\theta$, which is measured from the axis of loading, with $\theta = 0$ on the side which is subject to uplift. Clearly, the maximum compressive stress at $\theta = 180^{o}$ is dramatically reduced by preuplift. No attempt was made to measure the stresses in the mylar.

The stress distributions in Fig. 6.6 suggest that buckling due to the vertical compressive stress would occur at a higher tilt angle and/or water level if the tank is preuplifted. This is confirmed by the experimental data in Fig. 6.7, where the tilt angle for a given water depth at buckling is seen to be 1.5 to 2.0 times larger for the case with preuplift. Since the lateral load is approximately proportional to

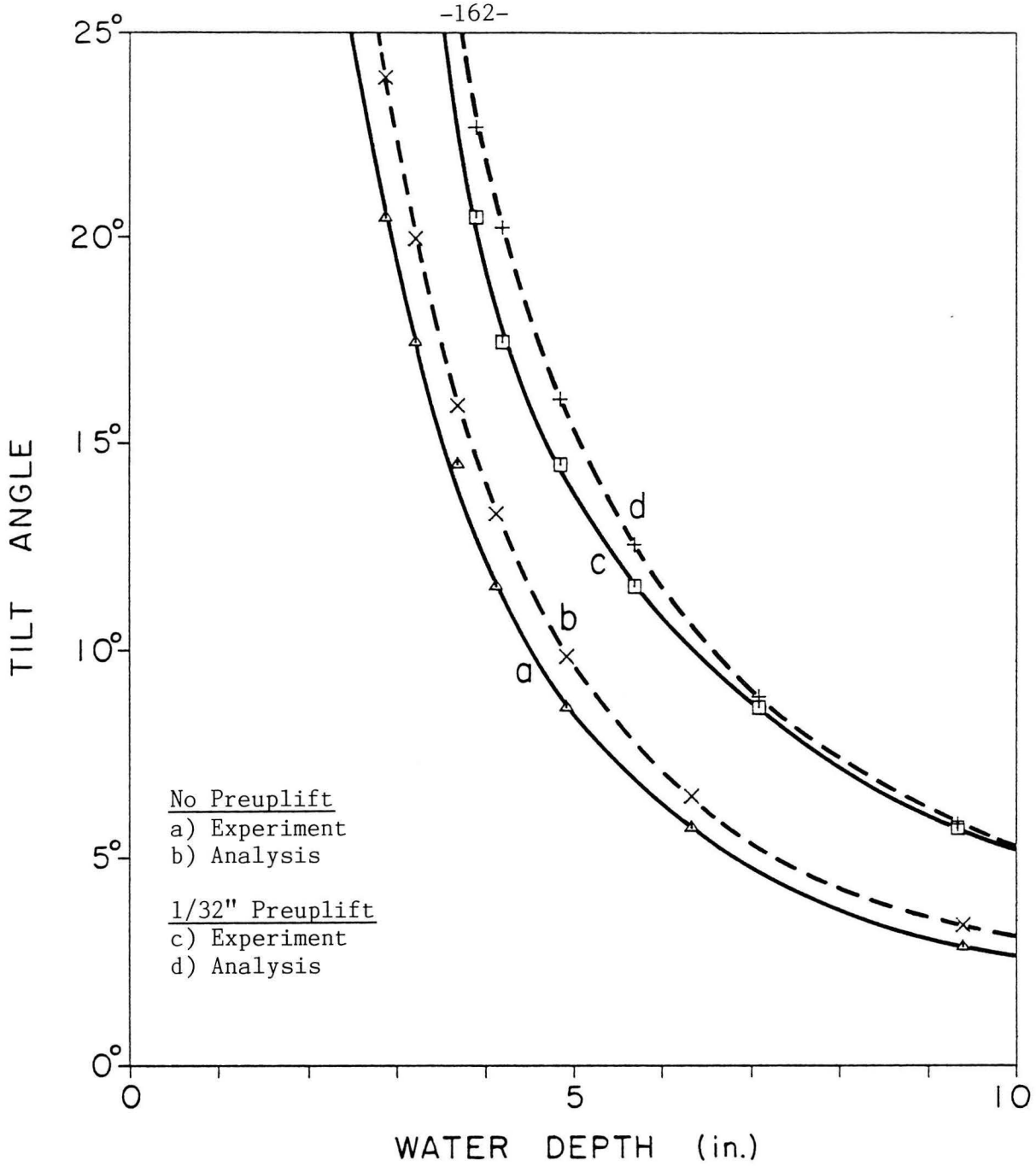


Figure 6.7: Water depth at buckling versus tilt angle from the experiments (continuous lines) and from the approximate analysis with the classical buckling criterion (dashed lines).

the tilt angle, this means that the preuplift increases the lateral load capacity by a factor of up to 2.

In order to obtain the theoretical tilt angles and water depths at buckling, it was assumed that the shell buckles when the peak vertical compressive stress reaches the classical buckling stress given in Eq. (6.1). This assumption is open to debate. On one hand, experiments on cylindrical shells in uniform axial compression [Weingarten, et al. (1960), Babcock (1974), Shih (1981)] indicate that the buckling loads are extremely sensitive to imperfections in the shell, and may be less than half the classical buckling load. On the other hand Shih (1981) found in his tilt tests on anchored mylar tanks, that the calculated peak compressive stress at buckling was about 1.24 times the classical value. He also discusses how the nonuniformity in the prebuckling stress field can result in higher buckling stresses. For an unanchored tank, one might expect that this effect of nonuniformity is even more pronounced, because the region of large vertical compressive stresses is smaller.

The theoretical tilt angles and water levels at buckling, obtained with the classical buckling criterion, are shown in Fig. 6.7, by broken lines. They confirm that preuplift substantially increases the lateral load capacity. Also, the agreement with the experimental data is certainly acceptable, if one considers the uncertainties in the buckling stress.

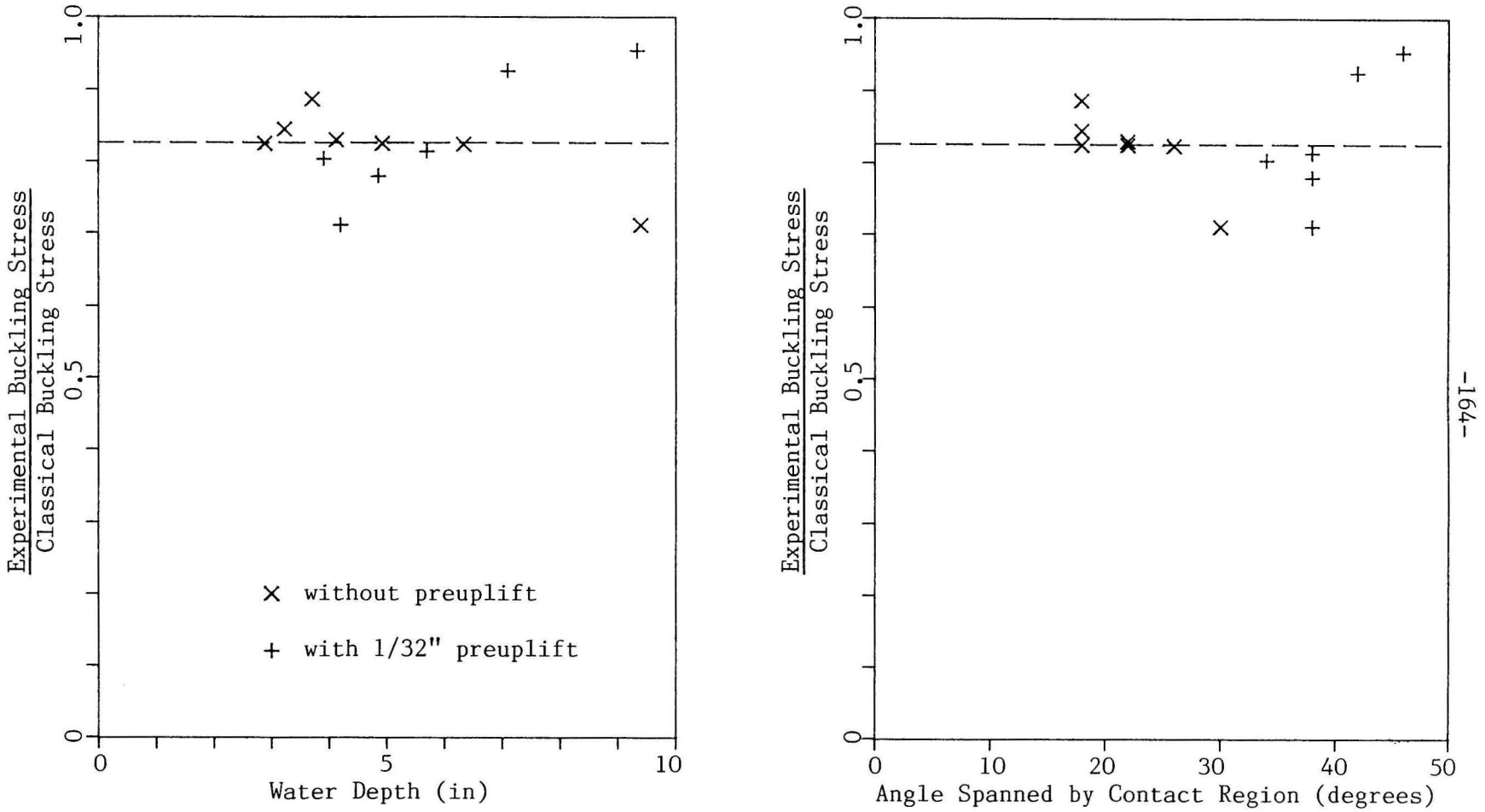


Figure 6.8: Calculated maximum compressive stresses at the tilt angles and water levels for which incipient buckling of the mylar tank was observed in the experiments.

The calculated peak compressive stress at the tilt angles and water levels for which incipient buckling was observed in the experiments will be referred to as the experimental buckling stress. The ratios of these experimental buckling stresses to the classical value of Eq. (6.1) are plotted in Fig. 6.8. The average value is 0.83 as indicated by the broken line. Fig. 6.8 also indicates that neither the internal pressure (which is proportional to the water level), nor the circumferential angle spanned by the contact region, or whether or not the tank is preuplifted seem to have any significant influence on the experimental buckling stress.

## 6.4 CLOSING REMARKS

Both the theoretical and experimental results presented show that preuplift substantially increases the capacity of an unanchored tank to withstand lateral loads due to tilting. There is little doubt that the same conclusion would apply for seismic lateral loads.* However, a number of questions remain unanswered at this time.

(i) Uplift will affect the dynamic response of the tank, by increasing its period of oscillation. For a preuplifted tank, this increase in the period of oscillation is less pronounced. Depending on the relative frequencies of the earthquake and the tank, this means that the preuplifted tank may experience a lateral load which is higher or lower

* Shih (1981) has shown that for an anchored tank, the stresses due to tilting are similar to seismically induced stresses.

than that for the case without preuplift.

(ii) The static stresses in the base plate induced by the preuplift may have some detrimental effect over long periods of time. Indeed, for most mild steel tanks preuplift results in flexural yield at the shell-base plate junction. This means that the weld at the junction must be stronger than both the shell and the base plate, and embrittlement of the heat affected zone must be avoided.

(iii) Some of the effectiveness of the preuplift could be lost due to creep strains in the base plate developing before the earthquake.

(iv) When, after a cycle of uplift, the tank wall descends upon the ring filler, the rapid vertical deceleration of the tank wall may well contribute to a large local hydrodynamic pressure acting on the preuplifted portion of the base plate. This could increase the plastic strains in the base plate and at the junction with the shell wall. As a result some of the effectiveness of the preuplift could be lost, and, ultimately, there may be some danger of tearing at the shell-base plate junction. This problem could be avoided if the ring filler is designed so that under normal operating conditions, it fills the space between the base plate and the foundation, but carries vertical loads only at the edge. This can be achieved by choosing a cross section of the ring filler which matches the deformed shape of the base plate

due to a uniform uplifting force applied at the edge only.

Some of these questions also apply to unanchored tanks without preuplift. For example, the local hydrodynamic pressures mentioned in (iv) above may contribute to the formation of the "elephant foot bulge" so commonly observed. While these issues remain to be studied, and in some cases may limit the effectiveness of preuplift somewhat, the author concludes that preuplift will in most cases significantly improve the behavior of unanchored tanks subject to earthquake loads.

## 7. SUMMARY AND CLOSURE

When a cylindrical steel tank is subjected to earthquake loads, the seismically induced vertical tension in the shell wall at the base exceeds the vertical compression due to the weight of the tank wall and roof (if present). This is true even for relatively light ground shaking. For an unanchored tank, the resulting net vertical tension causes the shell wall to uplift. The base plate is therefore also uplifted. Thus a hold-down force is developed due to the weight of fluid resting on the uplifted portion of the base plate.

The analysis of this problem requires consideration of the shell and the base plate, including nonlinear effects due to finite displacements, yielding of the steel, and loss of contact with the foundation.

The assumptions made in the method of analysis recommended in the current design standards of the American Water Works Association and the American Petroleum Institute are in most cases not applicable, and can result in calculated peak compressive stresses which are too low. On the other hand, the allowable peak compressive stress is also much lower than that observed. Therefore the current design standards are inconsistent rather than necessarily unconservative.

In an attempt to provide a more realistic idealization of the problem, two methods of analysis have been developed. Both are based on the moderate deflection, Von Karman, theory for the base plate, and a linearized formulation for the shell.

The first method of analysis is an approximate one in which the tank wall is supported from below by a circular bed of nonlinear Winkler springs. When in tension, these Winkler springs represent resistance to uplift provided by the base plate. When in compression, the Winkler springs represent the stiffness of the foundation. The force-deflection relation for the Winkler springs is determined from the solution of the axisymmetric problem in which the tank wall is uniformly uplifted all around the circumference. Three computer programs are used for this approximate analysis: One to solve the axisymmetric uplift problem, one to perform a static condensation on the tank wall, and the third uses the output of the previous two to solve the contact problem. Each of these could be run on a personal computer.

The second method of analysis is a more comprehensive one in which the non-axisymmetric problem for the partially uplifted base plate is solved. This is achieved by the finite difference energy method, using an expansion of the displacements as a Fourier series in the circumferential direction. Since both material and geometrical nonlinearities are included, the variations in the strain energy need to be integrated numerically. A tangent stiffness matrix is obtained in which there is coupling between the various Fourier coefficients of the displacements. This makes for a large amount of computational effort if a large number of Fourier coefficients are included in the analysis: A typical problem with 31* Fourier coefficients for the vertical displacements and 13* Fourier coefficients for the horizontal displacements took

* Including the coefficient of order zero.

10 to 15 minutes on a CRAY XMP-2-4 computer. This is about the number of Fourier coefficients required for accuracy in the vertical stresses in the shell wall at the base. However, accurate values of the uplift displacements can be obtained using only two or three Fourier coefficients. As a result the computational effort is reduced by two to three orders of magnitude (a factor of $10^2$-$10^3$). This is important in applying the method for dynamic analysis: The inertial forces and hydrodynamic pressures can be obtained with fairly good accuracy and relatively little computational effort from a time history analysis, using a small number of Fourier coefficients. The most severe inertial forces and hydrodynamic pressures can then be applied as static loads in a subsequent analysis using a larger number of Fourier coefficients, in order to obtain accurate values of the stresses.

In comparing the results from the approximate method of analysis based on the assumption of weak circumferential variations in the base plate to the more comprehensive approach, it is seen that for a tall aluminum tank which was loaded by applying a static tilt, the results from the approximate method of analysis are in close agreement with those from the more comprehensive method. For a broad, roofless tank however, the approximate analysis is distinctly less satisfactory.

As expected, the analyses show that uplift results in a large increase in the peak compressive stress in the tank wall at the base. For a given lateral load, these calculated peak compressive stresses are in good agreement with experimental results. In some cases they exceed the stresses calculated by the procedures outlined in the current API

and AWWA standards by a factor of more than 2. On the other hand, experiments on mylar tanks indicate that the peak compressive stress at which buckling occurs is close to the classical value, which is much larger than the allowable compressive stress permitted by the current design standards.

For most fluid storage tanks, the thickness to radius ratio is such that vertical compressive stresses can be expected to cause elastic buckling before they cause yielding. This is especially so if buckling occurs well before the classical buckling stress is reached. However, as has been suggested by Chen (1984), the combination of vertical stresses close to the classical buckling stress, hoop stresses due to internal hydrostatic and hydrodynamic pressures, and bending stresses due to the restraint at the base may well cause the material to yield before the point of elastic instability. In such cases plastic buckling can be expected to occur soon after the onset of yielding, because of the decrease in the material stiffness. This would probably result in what is generally referred to as an elephant foot bulge.

Hence, yielding as well as elastic instability should be considered as a possible failure mechanism for the tank wall. Whereas for elastic instability, internal pressure tends to increase the buckling stress, for yielding, internal pressure produces hoop tension and bending stresses which combine with the axial compressive stress to produce a more severe loading condition. This is especially important if the internal pressures are amplified by resonant breathing modes [Haroun and Tayel (1984, 1985 a,b), Sakai et al. (1984), Veletsos and Kumar (1984)],

and by the vertical motion of the base associated with rocking.

Although agreement of the theoretical results with available experimental results is good in some cases, in other cases there are significant discrepancies. These discrepancies could be due to geometrically nonlinear effects in the shell, yielding of the aluminum, residual stresses (due to welding, forming of the aluminum sheet, or due to plastic strains that may have developed during previous testing of the tanks), friction between the base plate and the foundation, or other inaccuracies in the mathematical idealization of the tank. Which of these effects is responsible for the discrepancies in each particular case, and to what extent experimental errors may also be involved is not clear.

In order to explain more precisely the differences between theoretical and experimental results, it seems that a program that allows an interplay between testing and analysis would be required. In an integrated program, experimental features could be addressed by special analyses and potential problems indicated by the analysis could be investigated experimentally. For example, the influence of friction between the foundation and the base plate could be virtually eliminated by greasing the surfaces. The tank could be annealed in order to eliminate residual stresses. Or, if this is impractical, an attempt could be made to estimate the residual stresses and they could be included in the analysis. Finally, a high strength material could be used to eliminate the effect of plasticity; or, alternatively, if plasticity is important the entire loading history for the tank could be

reproduced analytically.

In any future experiment it would be important to measure the stresses and displacements at several locations on the uplifted portion of the base plate, since this is where the geometrically nonlinear effects are most pronounced. The stress-strain behavior of the material should be determined experimentally. Also, the effect of heating and cooling from nearby welds on the stress-strain behavior should be investigated.

Using the preuplift method (Fig. 6.1) the hold-down force due to the weight of the fluid resting on an uplifted strip of the base plate can be developed without many of the undesirable consequences of uplift. It is shown by analysis and experiment, that for a 5 in diameter and 9-7/8 in tall mylar tank, a preuplift of 1/32 in increases the resistance to lateral loads due to tilting by a factor of up to 2.

Some questions regarding the preuplift method remain to be investigated: For example, preuplift affects the dynamics of an unanchored tank and therefore has some influence on the maximum lateral force and overturning moment. Also, the relatively large stresses in the base plate during operating conditions may have some detrimental effects such as creep, and the possibility of leakage due to the growth of microcracks. The loss of the effectiveness of the preuplift due to creep strains could be evaluated by an axisymmetric analysis, if a suitable description for the creep behavior of the steel can be found. Although these issues deserve to be studied in more detail, it appears that the seismic performance of unanchored tanks can be improved

significantly by preuplift.

## APPENDIX A - BUCKLING ANALYSIS OF BASE PLATE WITH BOSOR5

This appendix explains the use of the computer program BOSOR5 by Bushnell (1974) to determine the critical load for circumferential buckling in the base plate. Since BOSOR5 does not have built-in capabilities for contact problems, a separate analysis is required for each location of the contact point. The BOSOR5 mathematical model for the example problem of Chapter 2 is shown in Fig. A1. In this figure and in the rest of this appendix the node numbers used refer to those specified by the user. The program inserts additional nodes at junctions in order to model the boundary conditions.

The base plate is modeled as a single conical segment beginning at $(r,z) = (0,0)$ and ending at $(r,z) = (57,0)$. Nodes 1 to 21 are equally spaced on the portion of the base plate which remains in contact with the ground. Nodes 21 to 73 are also equally spaced, and the actual spacing is chosen such that node 21 is at $r = r_o$, the location of the contact point. At this node no rotation or vertical displacement are allowed.

The shell is modeled by a second segment with 61 equally spaced nodes covering a length of 15 in. This length is considered sufficient to model accurately the constraint provided by the shell for rotations and horizontal displacements. In addition, although the vertical stiffness of a 15 in length of shell is lower than that for the full length of the shell, it is seen from Fig. 2.11 that this vertical stiffness is sufficient to suppress any vertical displacements associated with the

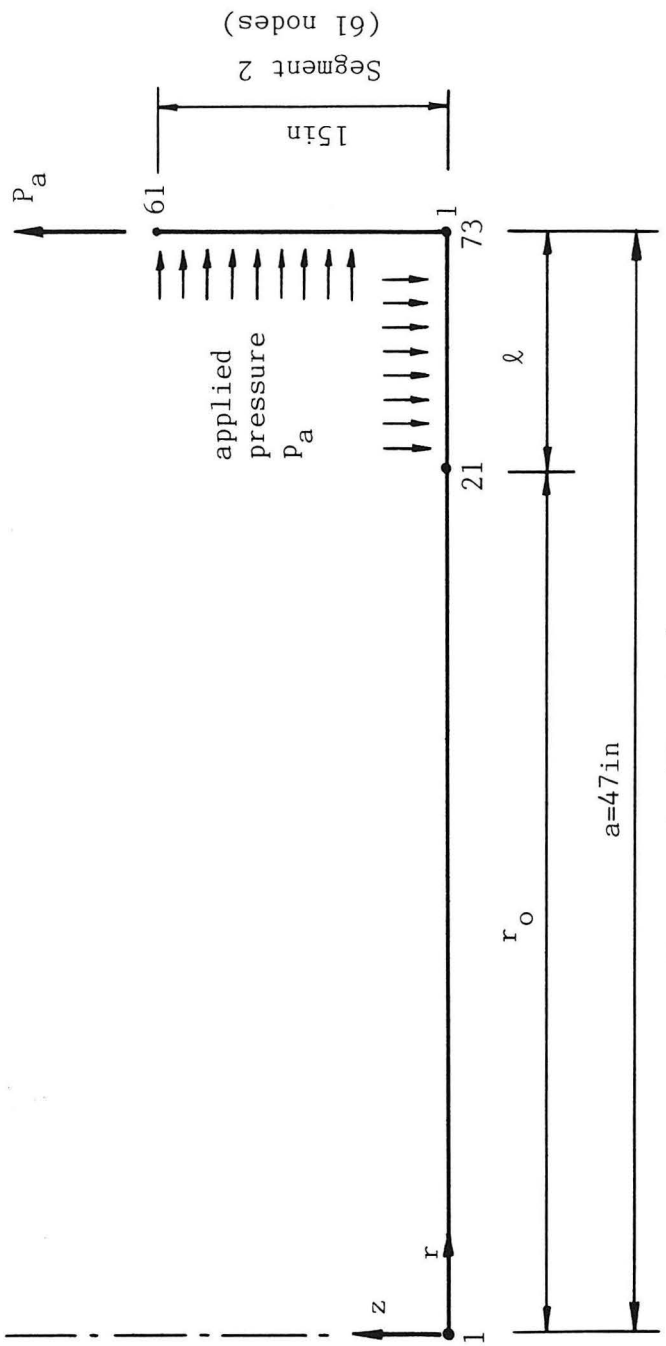


**Figure A1:** BOSOR5 model for the buckling analysis of the wine tank of Niwa and Clough (1982)

buckling mode at the edge.

At the junction between the base plate and the shell, continuity of all displacement components and the rotation is required. The plastic hinge is allowed to form naturally by yielding of the material, which is taken to be linearly strain hardening from 70 ksi at first yield to 70.5 ksi at 1% strain for loading in uniaxial tension. The stress resultants (membrane forces and bending moments) are obtained by numerical integration of the stresses at 7 points across the thickness of the plate. For the prebuckling analysis, the flow theory of plasticity is used with a Von Mises yield surface, and for the buckling analysis the deformation theory of plasticity is used.

The loading is applied as shown in Fig. A1, the applied pressure $p_a$ and the uplift force $P_a$ being given by

$$p_a = \xi p \tag{D1}$$

$$P_a = \xi P \ , \tag{D2}$$

in which

- $p$ = actual pressure as defined in Chapter 2,
- $P$ = uplift force determined by the shooting method (P depends on $r_o$ ), and
- $\xi$ = loading parameter.

Thus the loads are applied proportionally such that when the load parameter reaches unity, the conditions for the contact problem are matched. Although the loading path in this analysis is different from that for

the contact problem in which the radius to the contact point changes, this hardly affects the prebuckling conditions, since path dependencies can only be introduced due to yielding at the plastic hinge. As long as the direction of loading does not change, such path dependencies are limited to interaction effects between the various bending and membrane stresses, which are neglected.

To verify that the prebuckling conditions are suitably simulated by the above procedure, stresses and displacements obtained with BOSOR5 were compared to those obtained by the shooting method. Fig. A2 shows the comparison of vertical displacements, radial bending moments and circumferential membrane forces. Similar agreement was obtained for other quantities. The most noticeable difference is in the hoop compressive force near the edge. It occurs due to interaction between radial bending and circumferential compression: In the presence of large radial bending moments the capacity in circumferential compression is reduced. The effect of a finite plastic hinge length in the BOSOR5 model upon the response near the edge is apparent in Fig. A2a. Since the extent of such local effects is small compared to the buckling wavelength, they were neglected.

The trial and error procedure for determining the buckling load is as follows:

1. Estimate the radius to the contact point, $r_o$, when buckling occurs using results obtained by the shooting method, and simple plate buckling formulae.

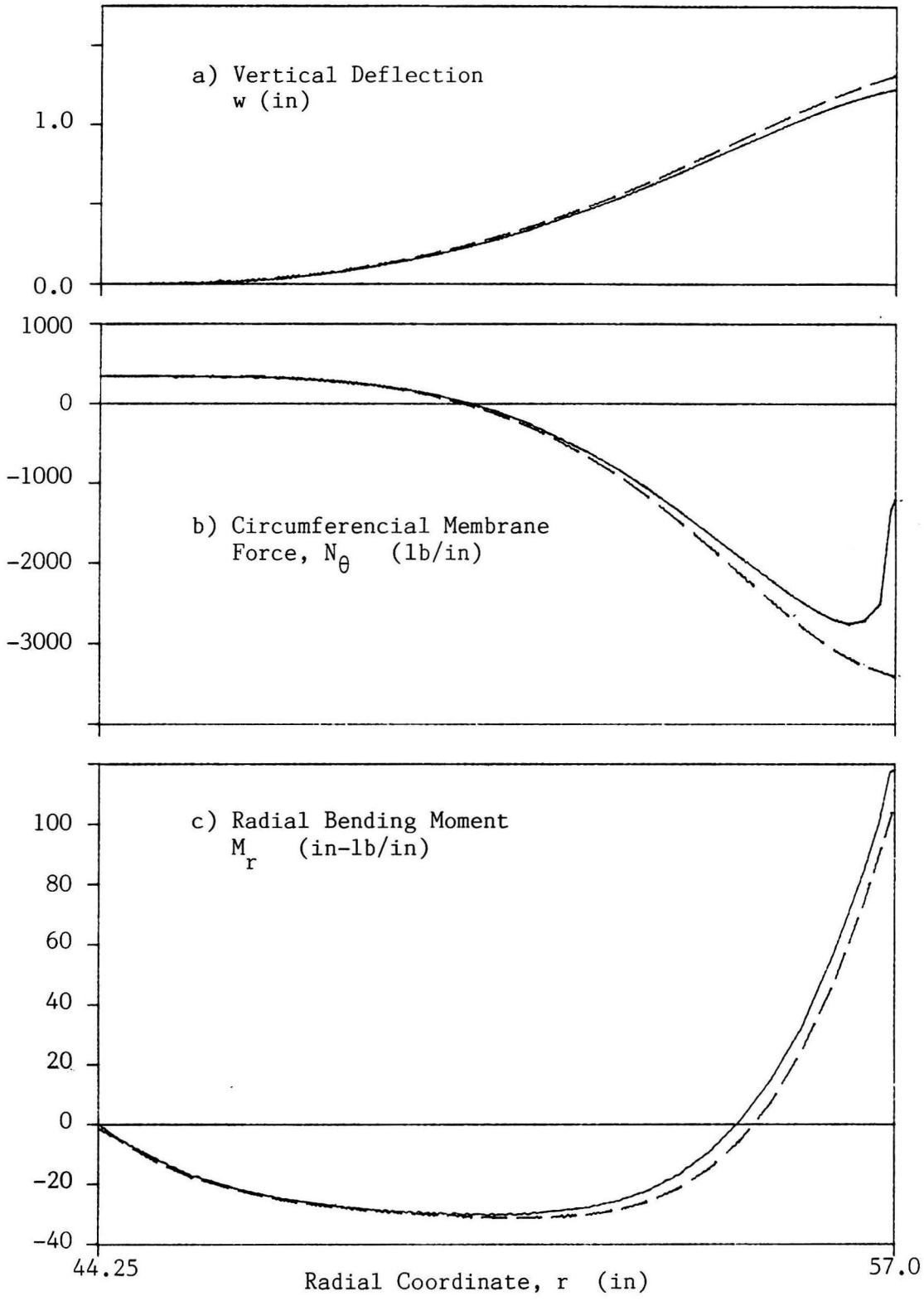


**Figure A2:** Comparison of prebuckling conditions from the BOSOR5 analysis (continuous lines) to those obtained by the shooting method (broken lines).

2. Construct the BOSOR5 model consistent with the chosen value of $r_o$, and determine the value of the load parameter $\xi$ at buckling. If it exceeds unity, try again with a smaller value of $r_o$; if it is less than unity, try again with a larger value of $r_o$.
3. Keep trying until the value of $r_o$ is found for which buckling occurs at $\xi = 1$. For the example tank considered, this occurs for $r_o = 44.25$ in, corresponding to an uplifted width of 12.75 in.

## APPENDIX B - CYLINDRICAL AXISYMMETRIC SHELL ELEMENT

Klein (1964) has presented a derivation of the stiffness matrix for conical, and, as a special case, cylindrical shell elements in which the displacements and stresses vary as trigonometric functions in the circumferential direction. However, for the special case of a cylindrical element his results are not stated in a convenient form. Haroun (1980) considers the specific case of a cylindrical element, but did not state the elements of the stiffness matrix explicitly. In the following pages, an outline of the derivation of such explicit expressions is given, and the final results are stated. The second section in this appendix is devoted to the added stiffness arising from non-linear effects due to internal fluid pressure.

### B1. DERIVATION OF STIFFNESS MATRIX FROM LINEAR SHELL THEORY

The derivation is based on what Flügge (1960) refers to as the "exact"* relationship between the strains at any point and the midsurface displacements, and the principle of virtual displacements. Thus, the need to use classical shell theory and stress resultants is avoided. This approach is generally known as the degeneration approach. A typical element, and the coordinate system used are shown in Fig. B1. It coincides with that of Flügge (1960), with Flügge's $\phi$ replaced by $\theta$. The thickness of the shell, t, is taken to be uniform throughout the

* Flügge's "exact" strain-midsurface displacement relations are only exact for infinitesimal displacements. In other strain-midsurface displacement relations given by Flügge's (1960) the additional assumption that the thickness is very small compared to the radius is made.

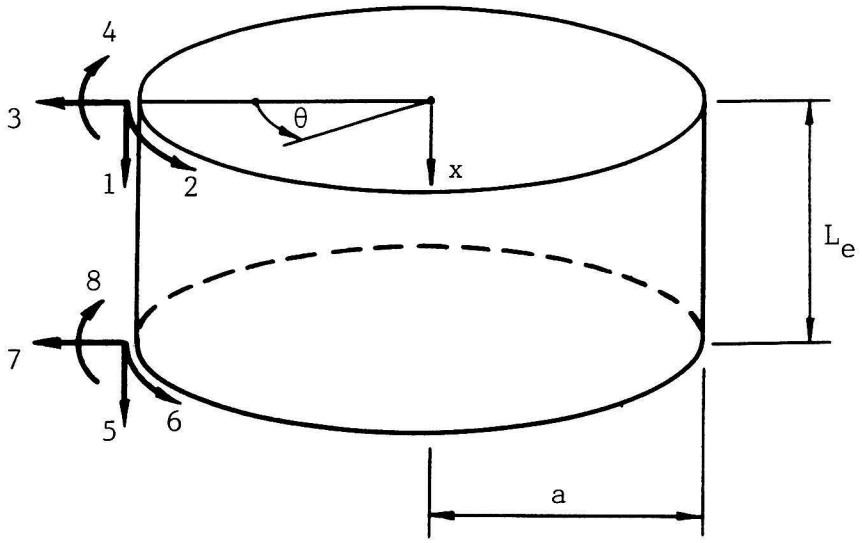


**Figure B1:** Definition of coordinates, element dimensions, and displacement directions corresponding to each of the degrees of freedom.

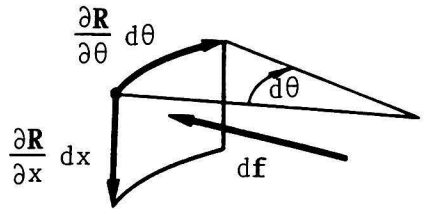


**Figure B2:** Pressure force df acting on an element dθ dx of the shell.

element, and the radius to the midsurface is a. As is indicated in Fig. B1, the intersection of the plane x = 0 and the cylinder will be termed node 1, and the intersection with the plane x = $L_e$, where $L_e$ is the length of the element, will be termed node 2.

The displacement components of the midsurface are defined as:

u = Vertical component of displacement, positive in the direction of increasing x.

v = Circumferential component of displacement positive in the direction of increasing $\theta$.

w = radial displacement, positive outward.

These displacements vary as functions of x and $\theta$. The $\theta$ dependence may be eliminated by making use of the orthogonality of trigonometric functions. In particular it is well known (Flügge, 1960) that in the linear shell theory the solution for radial and vertical loads varying as cos $n\theta$, and tangential loads varying as sin $n\theta$ may be written as

$$u = u_n \cos n\theta \tag{B1a}$$

$$v = \begin{cases} v_n \sin n\theta & \text{for } n \neq 0 \\ v_o & \text{for } n = 0 \end{cases} \tag{B1b}$$

$$w = w_n \cos n\theta \quad , \tag{B1c}$$

in which $u_n$, $v_n$, $w_n$ are functions of x only. In the finite element model it is assumed that $u_n$ and $v_n$ vary linearly between nodal points, and $w_n$ varies as a cubic polynomial. Thus the displacement in the ele-

ment is fully determined by the values of $u_n$, $v_n$, $w_n$, and $dw_n/dx$ at the nodal points. These nodal displacements are arranged into an element displacement vector q as follows

$$q_n = \left[ u_n^1 \; v_n^1 \; w_n^1 \; (dw_n/dx)^1 \; u_n^2 \; v_n^2 \; w_n^2 \; (dw_n/dx)^2 \right]^T , \qquad (B2)$$

in which $u_n^1$ = displacement $u_n$ at node 1, etc. The Fourier coefficients of the displacements are then given by

$$\begin{bmatrix} u_n \\ v_n \\ w_n \end{bmatrix} = Nq_n , \qquad (B2)$$

in which the 3 × 8 interpolation matrix N is given in Table B1.

Using the relation between midsurface displacements and the strains at any location within the shell given in Flügge (1960), the strains can be expressed in the following form:

$$\varepsilon(x,\theta,z) = \Theta(\theta) \; B(x,z) \; q_n , \qquad (B3)$$

in which the variables in parentheses indicate functional dependence, and

z = Distance from point under consideration to the mid surface, positive when the point under consideration is on the outside of the mid surface.

TABLE B1. Expressions for Matrices N and B

$$N = \begin{bmatrix} \xi & 0 & 0 & 0 & \eta & 0 & 0 & 0 \\ 0 & \xi & 0 & 0 & 0 & \eta & 0 & 0 \\ 0 & 0 & N_1 & L_1 & 0 & 0 & N_2 & L_2 \end{bmatrix}$$

$$B = \begin{bmatrix} -\frac{1}{L_e} & 0 & -\frac{\zeta}{a}N_1'' & -\frac{\zeta}{a}L_1'' & \frac{1}{L_e} & 0 & -\frac{\zeta}{a}N_2'' & -\frac{\zeta}{a}L_2'' \\ -\frac{n\xi}{a(1+\zeta)} & -\frac{(1+\zeta)}{L_e} & \frac{n\zeta(2+\zeta)}{a(1+\zeta)}N_1' & \frac{n\zeta(2+\zeta)}{a(1+\zeta)}L_1' & -\frac{n\eta}{a(1+\zeta)} & \frac{(1+\zeta)}{L_e} & \frac{n\zeta(2+\zeta)}{a(1+\zeta)}N_2' & \frac{n\zeta(2+\zeta)}{a(1+\zeta)}L_2' \\ 0 & \frac{n\xi}{a} & \frac{(1+n^2\zeta)}{a(1+\zeta)}N_1 & \frac{(1+n^2\zeta)}{a(1+\zeta)}L_1 & 0 & \frac{n\eta}{a} & \frac{(1+n^2\zeta)}{a(1+\zeta)}N_2 & \frac{(1+n^2\zeta)}{a(1+\zeta)}L_2 \end{bmatrix}$$

in which

$$\zeta = z/a$$

$$\xi = 1 - x/L_e \qquad \eta = x/L_e$$

$$N_1 = 1 - 3(x/L_e)^2 + 2(x/L_e)^3 \qquad N_2 = 3(x/L_e)^2 - 2(x/L_e)^3$$

$$L_1 = L_e[(x/L_e) - 2(x/L_e)^2 + (x/L_e)^3] \qquad L_2 = L_e[-(x/L_e)^2 + (x/L_e)^3]$$

$$(\,)' = a\frac{d}{dx}(\,)$$

$\varepsilon$ = 3 × 1 vector containing the vertical strain, the engineering shear strain, and the hoop or circumferential strain in the order stated.

$$\Theta = \begin{bmatrix} \cos n\theta & & \\ & \sin n\theta & \\ & & \cos n\theta \end{bmatrix} .$$

B = 3 × 8 matrix of interpolation functions and their derivatives given in Table B1.

Nodal loads are defined as forces or moments applied at the midsurface of the shell, expressed as a force or moment per unit length measured along the midsurface of the shell. Any twisting moments acting about x axis are replaced by their statically equivalent tangential and radial shear forces. This leads to the following nodal forces:

$P^i$ = Vertical membrane force at node i acting in the direction of increasing x.

$T^i$ = Tangential shear force at node i acting in the direction of increasing $\theta$.

$Q^i$ = Radial shear force at node i acting radially outwards.

$M^i$ = Moment at node i acting in the same sense as the rotation dw/dx.

These nodal forces are arranged into an element load vector as follows:

$$R = \left[P^1\ T^1\ Q^1\ M^1\ P^2\ T^2\ Q^2\ M^2\ \right]^T \quad . \tag{B4}$$

Note that R depends on $\theta$. Since all radial and vertical loads vary as cos $n\theta$, and all tangential loads vary as sin $n\theta$, R can be expressed as

$$R = \tilde{\Theta}\, R_n \quad , \tag{B5}$$

in which $R_n$ is independent of $\theta$, and $\tilde{\Theta}$ is a $8 \times 8$ diagonal matrix, the first and last four elements of which are given by cos $n\theta$, sin $n\theta$, cos $n\theta$, cos $n\theta$ in the order stated.

The principle of virtual displacements can be written

$$\int_0^{L_e} \int_{-t/2}^{t/2} \int_0^{2\pi} \delta\varepsilon^T D\varepsilon(a+z)\,d\theta\,dz\,dx = \int_0^{2\pi} (\tilde{\Theta}\,\delta q_n)^T(\tilde{\Theta}R_n)a\,d\theta \quad , \tag{B6}$$

in which

$\delta q_n$ = Arbitrary virtual displacement vector.

$\delta\varepsilon = \Theta B\,\delta q_n$ = virtual strains associated with virtual displacements $\delta q_n$.

$$D = \frac{E}{1-\nu^2}\begin{bmatrix} 1 & \nu & \\ \nu & 1 & \\ & & (1-\nu)/2 \end{bmatrix} \quad . \tag{B7}$$

Substituting for $\varepsilon$ from Eq. B3 gives

$$\delta q_n^T \int_0^{L_e} \int_{-t/2}^{t/2} B^T \int_0^{2\pi} \theta^T D\theta d\theta \; B(a+z)\, dz dx\; q_n = \delta q_n^T \int_0^{2\pi} \tilde{\theta}^T \tilde{\theta}\, d\theta\, aRn \quad .(B8)$$

Finally, carrying out the integration with respect to $\theta$, and considering the arbitrary nature of the variation $\delta q$ gives

$$Kq_n = R_n \quad , \tag{B9}$$

in which

$$K = \int_0^{L_e} \int_{-t/2}^{t/2} B^T D B (1+z/a) dz\, dx \tag{B10}$$

is the 8 × 8 symmetric element stiffness matrix. Carrying out the integrations indicated in Eq. 10, expressing the integrals as a power series in $(t/a)$, and neglecting terms of the order $(t/a)^5$ and higher gives:

$$K_{11} = K_{55} = \frac{Et}{1-\nu^2}\left[\frac{1}{L_e} + \left(\frac{1-\nu}{2}\right)\frac{L_e n^2 (1+k)}{3a^2}\right]$$

$$K_{12} = -K_{56} = \frac{Et}{1-\nu^2}\left[\frac{n(1-3\nu)}{4a}\right]$$

$$K_{13} = -K_{57} = \frac{Et}{2a(1-\nu^2)}\left[\nu + n^2 k\left(\frac{1-\nu}{2}\right)\right]$$

$$K_{14} = K_{58} = \frac{Et}{1-\nu^2} - \frac{ak}{L_e} + \frac{L_e}{12a}\left[n^2 k\left(\frac{1-\nu}{2}\right) - \nu\right]$$

$$K_{15} = \frac{Et}{1-\nu^2}\left[-\frac{1}{L_e} + \left(\frac{1-\nu}{2}\right)\frac{L_e n^2(1+k)}{6a^2}\right]$$

$$K_{16} = -K_{25} = -\frac{Et}{1-\nu^2}\left[\frac{n(1+\nu)}{4a}\right]$$

$$K_{17} = -K_{35} = \frac{Et}{2a(1-\nu^2)}\left[n^2 k\left(\frac{1-\nu}{2}\right) - \nu\right]$$

$$K_{18} = K_{45} = \left\{\frac{Et}{1-\nu^2}\frac{ak}{L_e} + \frac{L_e}{12a}\left[\nu - n^2 k\left(\frac{1-\nu}{2}\right)\right]\right\}$$

$$K_{22} = K_{66} = \frac{Et}{1-\nu^2}\left[\frac{L_e n^2}{3a^2} + \left(\frac{1-\nu}{2}\right)\left(\frac{1+3k}{L_e}\right)\right]$$

$$K_{23} = K_{67} = \frac{Et}{1-\nu^2}\left[\frac{7L_e n}{20\ a^2} + \frac{nk}{L_e}\left(\frac{3-\nu}{2}\right)\right]$$

$$K_{24} = -K_{68} = \frac{Et}{1-\nu^2}\left[\frac{L_e^2 n}{20\ a^2} + \nu nk\right]$$

$$K_{26} = \frac{Et}{1-\nu^2}\left[\frac{L_e n^2}{6\ a^2} - \left(\frac{1-\nu}{2}\right)\left(\frac{1+3k}{L_e}\right)\right]$$

$$K_{27} = K_{36} = \frac{Et}{1-\nu^2}\left[\frac{3L_e n}{20\ a^2} - \frac{nk}{L_e}\left(\frac{3-\nu}{2}\right)\right]$$

$$K_{28} = -K_{46} = -\frac{Et\ L_e^2 n}{(1-\nu^2)30\ a^2}$$

$$K_{33} = K_{77} = \frac{Et}{1-\nu^2}\left[\frac{12\ a^2 k}{L_e^3} + \frac{13\ L_e[1+(n^2-1)^2 k]}{35\ a^2} + \frac{12\ kn^2}{5\ L_e}\right]$$

$$K_{34} = -K_{78} = \frac{Et}{1-\nu^2}\left[\frac{6\,a^2k}{L_e^2} + \frac{11\,L_e^2[1+(n^2-1)^2k]}{210\,a^2} + kn^2(\nu+1/5)\right]$$

$$K_{37} = \frac{Et}{1-\nu^2}\left[-\frac{12\,a^2k}{L_e^3} + \frac{9\,L_e[1+(n^2-1)^2k]}{70\,a^2} - \frac{12\,n^2k}{5\,L_e}\right]$$

$$K_{38} = -K_{47} = \frac{Et}{1-\nu^2}\left[\frac{6\,a^2k}{L_e^2} - \frac{13\,L_e^2[1+(n^2-1)^2k]}{420\,a^2} + \frac{n^2k}{5}\right]$$

$$K_{44} = K_{88} = \frac{Et}{1-\nu^2}\left[\frac{4\,a^2k}{L_e} + \frac{L_e^3[1+(n^2-1)^2k]}{105\,a^2} + \frac{4\,L_e\,n^2k}{15}\right]$$

$$K_{48} = \frac{Et}{1-\nu^2}\left[\frac{2a^2k}{L_e} - \frac{L_e^3[1+(n^2-1)^2k]}{140\,a^2} - \frac{L_e n^2k}{15}\right] , \qquad \text{(B11)}$$

in which

$$k = \frac{1}{12}\frac{t^2}{a^2} . \qquad \text{(B12)}$$

Because of the large amount of algebra involved and the possibility of errors, Eqs. B11 were obtained with the aid of a symbolic manipulation computer program, and verified numerically on an example. For the reader who wishes to use these elements and check numerical values of the elements of the stiffness matrix, an example is provided in Table B2.

The total strain energy in an element is $\frac{1}{2}\pi aq^TKq$ for $n \neq 0$, and $\pi aq^TKq$ for $n = 0$, not simply $\frac{1}{2}q^TKq$, as is usually the case.

TABLE B2. Element Stiffness Matrix - Numerical Example

Properties:

Radius to mid-surface: $a = 360$

Length of element: $L = 24$

Thickness of shell: $t = 0.5$

Elastic properties: $E = 30 \times 10^6$ , $\nu = 0.3$

Harmonic number: $n = 5$



Resulting Element Stiffness Matrix, K:

$$\begin{bmatrix}
695716.32 & & & & & \text{symmetric} & & \\
5723.4432 & 265822.26 & & & & & & \\
-6868.1641 & 5342.6256 & 1438.6122 & & & & & \\
-27512.145 & 18318.993 & 7448.0615 & 74405.101 & & & & \\
-682361.62 & 74404.762 & 6868.0997 & 27512.145 & 695716.32 & & & \\
-74404.762 & -227665.97 & 2288.6320 & 12210.012 & -5723.4432 & 265822.26 & & \\
-6868.0997 & 2288.6320 & 87.780661 & -1322.6171 & 6868.1641 & 5342.6256 & 1438.6122 & \\
27512.145 & -12210.012 & 1322.6171 & 15951.194 & -27512.145 & -18318.993 & -7448.0615 & 74405.101
\end{bmatrix}$$

The performance of the element was checked for a semi-infinite cylinder with loads applied at the edge $x = 0$. For this problem the analytical solution is given in Flugge (1960). The finite element model was constructed by discretizing a finite length of the cylinder, enforcing the boundary conditions for a semi-infinite cylinder (available from the analytic solution) at one end, and applying edge loads at the other end. The numerical tests were carried out for $n = 0$ and $n = 5$, and a cylinder with $a/t = 720$, which is typical for a tank. It was found that the elements performed very well: Better than 5% accuracy was obtained with elements of length equal to the characteristic length of the cylinder,

$$\lambda = \left[\frac{at}{3(1-\nu^2)}\right]^{1/2},$$

close to the edge, and better than 1% for half that element size. If only axial force and tangential shear is applied at the edge, better than 5% accuracy in the displacements u, v and w was obtained for an element length of a/4, and better than 1% accuracy for half that element length. This indicates that in a region where bending stresses are negligible, element lengths of a/4 to a/8 can be used. If bending stresses are important, the element length should be of the order of $(at)^{1/2}$.

## B2. ADDED STIFFNESS DUE TO NON-LINEAR EFFECTS

Much like the air pressure in a soap bubble tends to maintain its spherical shape, the fluid pressure in a cylindrical storage tank tends to maintain its round shape. This increase in the stiffness of the shell due to the hydrostatic fluid pressure is a non-linear effect. By established methods for the finite element solution of problems involving geometric nonlinearities (Zienkiewicz, 1977), the tangent stiffness matrix for a shell element subjected to an internal pressure p can be obtained. The added stiffness due to initial circumferential hoop forces has been derived by Haroun (1980) and is given in Table B3 for the coordinate system used here.

Another effect which can be of some importance is the pressure-rotation effect. Since the direction of the normal to the shell surface changes, so does the direction of the pressure load. In addition, the area of an element on the shell changes, so the magnitude of the pressure force changes. Changes in area are proportional to membrane strains which tend to be much smaller than the rotations (expressed in radians). Hence, the pressure rotation effect is more important than the change in area. Here both effects are included. However, the effect of changes in the elevation of the free surface due to deformations of the shell is not considered.

Let $\hat{r}$ $\hat{\theta}$ and $\hat{x}$ be orthonormal unit vectors pointing in the direction of increasing r, $\theta$ and x respectively (see Fig. B1). Then, in the deformed shell, the position vector of a point $(\theta,x)$ on the midsurface of the shell is

TABLE B3. Initial stress matrix $K_\sigma$ to be added to the element stiffness matrix K defined in Eqs. B11 and B12 in order to account for the circumferential stress due to a uniform internal pressure p.

$$K_\sigma = \frac{p}{a}\begin{bmatrix}
\frac{n^2 L_e}{3} & 0 & 0 & 0 & \frac{n^2 L_e}{6} & 0 & 0 & 0 \\
 & \frac{(1+n^2)L_e}{3} & \frac{7n\,L_e}{10} & \frac{n\,L_e^2}{10} & 0 & \frac{(1+n^2)L_e}{6} & \frac{3n\,L_e}{10} & -\frac{n\,L_e^2}{15} \\
 & & \frac{13(1+n^2)L_e}{35} & \frac{11(1+n^2)L_e^2}{210} & 0 & \frac{3n\,L_e}{10} & \frac{9(1+n^2)L_e}{70} & -\frac{13(1+n^2)L_e^2}{420} \\
 & & & \frac{(1+n^2)L_e^3}{105} & 0 & \frac{n\,L_e^2}{15} & \frac{13(1+n^2)L_e^2}{420} & -\frac{(1+n^2)L_e^3}{140} \\
 & & & & \frac{n^2 L_e}{3} & 0 & 0 & 0 \\
 & \text{symmetric} & & & & \frac{(1+n^2)L_e}{3} & \frac{7n\,L_e}{10} & -\frac{n\,L_e^2}{10} \\
 & & & & & & \frac{13(1+n^2)L_e}{35} & -\frac{11(1+n^2)L_e^2}{210} \\
 & & & & & & & \frac{(1+n^2)L_e^3}{105}
\end{bmatrix}$$

$$\underset{\sim}{R} = (a+w)\hat{r} + v\hat{\theta} + (x+u)\hat{x} \quad . \tag{B13}$$

Assume that the pressure p is constant over an element. From Fig. B2 it is seen that the force exerted by the pressure over an element $d\theta dx$ of the shell is given by

$$d\underset{\sim}{f} = p\left(\frac{\partial R}{\partial \theta}\, d\theta\right) \times \left(\frac{\partial R}{\partial x}\, dx\right) \quad , \tag{B14}$$

evaluating the cross product, and neglecting terms which are quadratic in the displacements gives

$$d\underset{\sim}{f} = (X\hat{x}+Y\hat{\theta}+Z\hat{r})a\,d\theta dx \quad , \tag{B15}$$

in which

$$\begin{aligned} X &= -\frac{p}{a}\, w' \\ Y &= \frac{p}{a}\,(v-w^{\cdot}) \\ Z &= p + \frac{p}{a}\,(u'+w+v^{\cdot}) \quad , \end{aligned} \tag{B16 a-c}$$

where

$$(\,)' = \frac{\partial}{\partial x}(\,) \quad \text{and} \quad (\,)^{\cdot} = \frac{\partial}{\partial \theta}(\,) \quad .$$

X, Y and Z represent the forces per unit area acting in the vertical, tangential, and radial directions, respectively. The vertical and tangential forces are due to the pressure-rotation effect. In the expression for the radial force Z, the first term is due to the direct pressure, and will be omitted since it is already present in the usual linear formulation of the problem. The additional terms in Eq. B16c

arise due to the change in area.

Substituting Eqs. B1 into Eqs. B16, and noting that the hydrostatic pressure p is a function of x only and not of $\theta$, it is seen that

$$(X,Y,Z) = (X_n \cos n\theta \ , \ Y_n \sin n\theta \ , \ Z_n \cos n\theta) \quad , \tag{B17}$$

where

$$\begin{aligned} X_n &= \frac{\rho}{a} w'_n \\ Y_n &= \frac{\rho}{a} (v_n + n w_n) \\ Z_n &= p + \frac{\rho}{a} (u'_n + w_n + n v_n) \quad . \end{aligned} \tag{B18}$$

The corresponding nodal loads are given by

$$R_n = \int_0^{L_e} \begin{bmatrix} \xi \ X_n \\ \xi \ Y_n \\ N_1 \ Z_n \\ L_1 \ Z_n \\ \eta \ X_n \\ \eta \ Y_n \\ N_2 \ Z_n \\ L_2 \ Z_n \end{bmatrix} dx \quad . \tag{B19}$$

Substituting from Table B1, Eqs. B2, and Eqs. B18 into Eqn. B19, and performing the integration yields

$$R_n = - K_p \, q_n \tag{B20}$$

for the energy equivalent nodal loads for the pressure-rotation effect, in which $K_p$ is given in Table B4. $K_p$ represents an added stiffness due to the pressure-rotation and the change in area of an element of the shell. The sum of the added stiffnesses due to the initial hoop force and due to the pressure-rotation effect is given in Table B5.

## B3. DISCUSSION OF SYMMETRY

Note from Table B4 that there are two pairs of elements in $K_p$ which make the matrix non-symmetric. The reason for this is that the pressure load as defined here is non-conservative. To see this, consider the following closed cycle of deformations:

0. Start with an undeformed shell element.
1. Extend the element in the vertical, x-direction so as to increase its length from $L_e$ to $L_e + \Delta L_e$. Since this involves only vertical displacements, the work done by the pressure force during this step is

$$\Delta W_1 = 0 \quad .$$

2. Expand the element in the radial direction so as to increase its radius from a to a + Δa. The work done by the pressure force during this step is

TABLE B4. Added element stiffness matrix $K_p$ due to the pressure rotation effect and the effect of changes in the area over which the pressure acts.

$$K_p = \frac{p}{a}\begin{bmatrix}
0 & 0 & -\frac{a}{2} & \frac{aL_e}{12} & 0 & 0 & \frac{a}{2} & -\frac{aL_e}{12} \\
 & -\frac{L_e}{3} & -\frac{7n\,L_e}{20} & -\frac{nL_e^2}{20} & 0 & -\frac{L_e}{6} & -\frac{3n\,L_e}{20} & \frac{nL_e^2}{30} \\
\frac{a}{2} & & -\frac{13\,L_e}{35} & -\frac{11\,L_e^2}{210} & -\frac{a}{2} & -\frac{3n\,L_e}{20} & -\frac{9L_e}{70} & \frac{13\,L_e^2}{420} \\
 & & & -\frac{L_e^3}{105} & -\frac{aL_e}{12} & -\frac{nL_e^2}{30} & -\frac{13\,L_e^2}{420} & \frac{L_e^3}{140} \\
 & & & & 0 & 0 & +\frac{a}{2} & \frac{aL_e}{12} \\
 & & \text{Symmetric except for} & & & -\frac{L_e}{3} & -\frac{7n\,L_e}{20} & \frac{nL_e^2}{20} \\
 & & \text{the elements shown} & & & & -\frac{13\,L_e}{35} & \frac{11\,L_e^2}{210} \\
 & & & & & & & -\frac{L_e^3}{105}
\end{bmatrix}$$

TABLE B5. Total added stiffness matrix $K_a = K_\sigma + K_p$. This matrix must be added to the stiffness matrix defined in Eqs. B11 and B12 in order to obtain the tangent stiffness matrix for an element subjected to a uniform internal pressure p.

$$K_a = \frac{p}{a}$$

$$\begin{bmatrix}
\frac{n^2 L_e}{3} & 0 & -\frac{a}{2} & \frac{aL_e}{12} & \frac{n^2 L_e}{6} & 0 & \frac{a}{2} & -\frac{aL_e}{12} \\
 & \frac{n^2 L_e}{3} & \frac{7n L_e}{20} & \frac{nL_e^2}{20} & 0 & \frac{n^2 L_e}{6} & \frac{3n L_e}{20} & -\frac{nL_e^2}{30} \\
\frac{a}{2} & & \frac{13 n^2 L_e}{35} & \frac{11 n^2 L_e^2}{210} & -\frac{a}{2} & \frac{3n L_e}{20} & \frac{9 n^2 L_e}{70} & -\frac{13 n^2 L_e^2}{420} \\
 & & & \frac{n^2 L_e^3}{105} & -\frac{aL_e}{12} & \frac{nL_e^2}{30} & \frac{13 n^2 L_e^2}{420} & -\frac{n^2 L_e^3}{140} \\
 & & & & \frac{n^2 L_e}{3} & 0 & \frac{a}{2} & \frac{aL_e}{12} \\
 & & & & & \frac{n^2 L_e}{3} & \frac{7n L_e}{20} & -\frac{nL_e^2}{20} \\
 & & & & -\frac{a}{2} & & \frac{13 n^2 L_e}{35} & -\frac{11 n^2 L_e^2}{210} \\
 & & & & & & & \frac{n^2 L_e^3}{105}
\end{bmatrix}$$

Symmetric except for elements shown

$$\Delta W_2 = p(L_e+\Delta L_e)\pi\left[(a+\Delta a)^2 - a^2\right] \quad .$$

3. Remove the extension in the vertical direction, so as to reduce the length of the element back to $L_e$. As in step 1, only vertical displacements are involved. Thus

$$\Delta W_3 = 0 \quad .$$

4. Remove the expansion in the radial direction, bringing the element back to its original, undeformed configuration. The work done by the pressure load during this final step is

$$\Delta W_4 = -pL_e\pi\left[(a+\Delta a)^2 - a^2\right]p \quad .$$

The total work done by the pressure force during this closed cycle of deformation is

$$\Delta W = \sum_{i=1}^{4} \Delta W_i = p\Delta L_e\pi\left[2a\Delta a+(\Delta a)^2\right] \quad ,$$

which is non-zero. This proves that the pressure force is non-conservative. Hence, it should come as no surprise that the finite element formulation leads to a non-symmetric matrix.

Consider now the physical problem of liquid in a tank. Since for any configuration of the tank, the liquid has a well defined gravitational potential, the hydrostatic pressure acting on the tank is a conservative load, and for any conservative system, the tangent stiffness matrix is symmetric. However, for the tank-water system to be conservative in the mathematical formulation of the problem, it would be

necessary to consider the effect of changes in elevation of the free surface due to deformations of the shell, and the effect of changes in elevation of any point on the shell wall on the pressure at that point. Such a formulation would lead to a symmetric stiffness matrix. Hence, the lack of symmetry of the matrices given in Tables 4 and 5 is a result of approximations made in their derivation.

Computationally, non-symmetric matrices are undesirable because of the additional computational effort and storage required. Since here the lack of symmetry arises from neglecting an effect which is presumed to be unimportant, it seems reasonable to make the matrix symmetric. In an attempt to do this one might consider only the pressure-rotation effect, and not the change in area of an element of the shell. In this case, the 1st, 2nd, 5th and 6th rows of $K_p$, would remain unchanged, but the 3rd, 4th, 7th and 8th rows would become zero. This would make the matrix $K_p$ much more non-symmetric. Thus there is a good reason to include the effect of changes in area of an element of the shell wall.

Consider the lack of symmetry in the matrix $K_p$ that remains when the effect of changes in area is considered. Those elements of the matrix $K_p$ which do not have a symmetric counterpart on the other side of the diagonal will be referred to as the "non-symmetric elements" of $K_p$. They are $K_{p31} = -K_{p11} = K_{p57} = -K_{p75} = p/2$. Note that they are independent of element properties. Furthermore, if two elements subjected to the same internal hydrostatic pressure are connected, and their stiffness matrices are superposed in the appropriate way, the non-symmetric elements of the matrices related to the connected node cancel.

For a storage tank, the hydrostatic pressure varies with elevation, so for any pair of elements the average hydrostatic pressure for the upper element is slightly lower than for the lower element, as is shown in Fig. B3. Hence, the non-symmetric elements of the element stiffness matrix do not cancel completely when the global stiffness matrix is formed. For node B of Fig. B3 the non-symmetric elements in the global added stiffness matrix $K_p$ are $k_{13} = -k_{31} = (p_2-p_1)/2$. They apply to degrees of freedom 1 and 3 shown in Fig. B1. If the origin of these non-symmetric terms is traced through the derivation given above, it is seen that: The non-symmetric elements above the diagonal are due to the vertical component of the pressure force arising from the rotation w'/a. The non-symmetric elements below the diagonal on the other hand are due to the increase in radial component of the pressure force arising from changes in area associated with the vertical membrane strain u'/a. Since strains tend to be much smaller than rotations, it is tempting to achieve symmetry by changing the sign of the non-symmetric elements below the diagonal. In the following such a modification will be justified further.

Consider the determination of $k_{31}$ directly, with reference to Fig. B3: In the undeformed configuration of Fig. B3a, the nodal force for degree of freedom 3 is

$$R_3^o = \tfrac{1}{2}\left[p_1 L_1 + p_2 L_2\right] \quad .$$

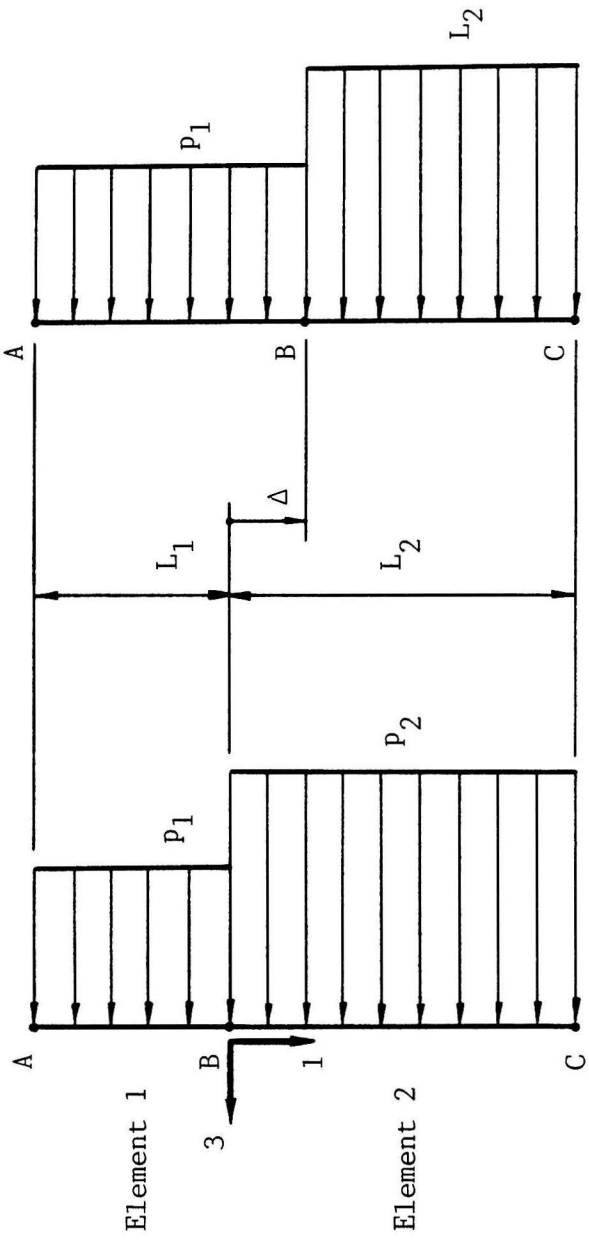


**Figure B3:** Pressure forces acting on 2 Shell Elements,
(a) undeformed configuration
(b) deformed configuration
(displacement Δ for degree of freedom 1)

Next apply a displacement $\Delta$ in the direction of degree of freedom number 1. The resulting configuration is shown in Fig. B3b, together with the pressure distribution that corresponds to the assumption that the pressure is a constant at a given location on the shell. In this deformed configuration, the nodal force for degree of freedom 3 is

$$R_3 = \tfrac{1}{2}\left[p_1(L_1+\Delta) + p_2(L_2-\Delta)\right]$$

$$= R_3^o + k_{31}\Delta \quad \text{with} \quad k_{31} = -\tfrac{1}{2}(p_2-p_1) \quad .$$

However, more realistically, one might assume that the pressure at a given elevation is a constant. Thus if a point on the shell moves vertically, it may move into a region of different pressure. In this case, the nodal force for degree of freedom 3 is obtained by applying the pressure distribution of Fig. B3a to the elements in their deformed configuration of Fig. B3b. Omitting terms of order $\Delta^3$ or higher, the resulting energy consistent nodal force is found to be

$$R_3 = \tfrac{1}{2}\, p_2(L_2-\Delta) + \tfrac{1}{2}\, p_1(L_1+\Delta) + (p_2-p_1)\Delta \quad ,$$

which can be re-written in the form

$$R_3 = R_3^o + k_{31}\Delta \quad \text{with} \quad k_{31} = +\tfrac{1}{2}(p_2-p_1) \quad .$$

Thus, with the assumption that the pressure is a constant at a given elevation, the non-symmetric element $k_{31}$ changes sign, and the lack of symmetry disappears. Similar considerations for other elements of the global stiffness matrix lead to the conclusion that the other elements

are not affected* by the possibility that the pressure at a given point on the shell may change due to vertical displacements at that point. Hence, it is recommended that the added stiffness matrix be taken to be symmetric by using the upper triangular part of the matrices given in Tables 4 and 5.

## B.4 CONCLUDING REMARKS

It must be emphasized that the added stiffness matrix derived here is the change in the tangent stiffness matrix due to loading by the hydrostatic fluid pressure. Additional seismic loads produce further changes in the tangent stiffness matrix and introduce coupling between the various Fourier harmonics (Tani et al. 1984). Ignoring these effects is equivalent to linearizing the problem about the full, but otherwise unloaded state. This is a good approximation only if additional loads due to the earthquake are small compared to the hydrostatic fluid pressure. That is, the hydrodynamic pressures must be small compared to the hydrostatic pressure. Under strong shaking, the hydrodynamic pressures are often of the same order as the hydrostatic pressure. Under such conditions accurate solution of the non-linear problem would require simultaneous solution of non-linear equations at every load or time step. Therefore, although the analysis based on the tangent stiffness matrix derived in this appendix requires no more effort than a fully linear analysis, the accuracy for large seismic loads is open to question.

---

* Except for the term $k_{14}$, where degree of freedom 4 is the rotation, for which the effect is of higher order in the displacements.

## APPENDIX C - RESULTS FROM THE THEORY OF DISCRETE FOURIER TRANSFORMS

The fundamental relation on which the theory of discrete Fourier transforms is based, quoted, for example, in Brigham (1974), can be written in the form

$$\sum_{n=0}^{2N-1} e^{i\pi rn/N} = 2N \quad \text{for} \quad r = \ldots -2N, 0, 2N, \ldots$$

$$= 0 \quad \text{otherwise} \; ; \tag{C1}$$

or, taking the real part of Eq. C1,

$$\sum_{n=0}^{2N-1} \cos(\pi rn/N) = 2N \quad \text{for} \quad r = \ldots -2N, 0, 2N, \ldots$$

$$= 0 \quad \text{otherwise} \; ; \tag{C2}$$

but,

$$\sum_{n=0}^{2N-1} \cos(\pi rn/N) = \sum_{n=0}^{N} \gamma_n \cos(\pi rn/N) + \sum_{n=N}^{2N} \gamma_n \cos(\pi rn/N) \; , \tag{C3}$$

where

$$\gamma_n = \frac{1}{2} \quad \text{for} \quad n = \ldots -2N, -N, 0, N, 2N, \ldots$$

$$= 1 \quad \text{otherwise} \; . \tag{C4}$$

Substituting n = 2N-m, the last sum becomes

$$\sum_{n=N}^{2N} \gamma_n \cos(\pi r n/N) = \sum_{m=0}^{N} \gamma_m \cos[\pi r(2N-m)/N] \quad ,$$

which by periodicity and symmetry of the cosine function is seen to be equal to the first term on the right hand side of Eq. C3. Hence Eq. C2 becomes*

$$\sum_{n=0}^{N} \gamma_n \cos(\pi r n/N) = N \quad \text{for} \quad r = \ldots, -2N, 0, 2N, \ldots$$

$$= 0 \quad \text{otherwise} \quad . \tag{C5}$$

Using Eq. C5 it can be shown that

$$\frac{2}{N} \sum_{i=0}^{N} \gamma_n \gamma_i \cos(mi\pi/N) \cos(ni\pi/N) = \delta_{mn}$$

$$\text{for} \quad m,n = 0,1,2,\ldots,N \quad , \tag{C6}$$

where $\delta_{mn}$ is the Kronecker delta. Furthermore, Eq. C6 can be used to show that if

$$x(\theta) = \sum_{n=0}^{N} x_n \cos n\theta$$

and

---

* A different form based on values of the cosine function at $\theta = \pi r(n-1/2)/N$ does not involve $\gamma_n$ factors, but in the formulation of problems this form does not lead directly to quantities of physical interest at $\theta = 0$ and $\pi$.

$$x^i \equiv x(i\pi/N) = \sum_{n=0}^{N} x_n \cos(ni\pi/N) \quad , \tag{C7}$$

then

$$x_n = \frac{2\gamma_n}{N} \sum_{i=0}^{N} \gamma_i x^i \cos(ni\pi/N) \quad . \tag{C8}$$

## APPENDIX D - STIFFNESS MATRIX FOR A RING ELEMENT

From Lee and Nash (1982), the elements of the 4 × 4 stiffness matrix for a ring stiffener, which is compatible with the element stiffness matrices of Appendix B are

$$K_{11} = EI_z \frac{n^4}{a_o^4} + GI_t \frac{n^2}{a_o^4}$$

$$K_{14} = EI_z \left[\frac{n^2}{a_o^3} - \frac{n^4 e}{a_o^4}\right] + GI_t \frac{n^2 a}{a_o^4}$$

$$K_{22} = EA \frac{n^2}{a^2}$$

$$K_{23} = EA \frac{n}{a\, a_o} \left[1 + \frac{n^2 e}{a}\right]$$

$$K_{33} = \frac{EA}{a_o^2} \left[1 + \frac{n^2 e}{a}\right]^2 + \frac{EI_x}{a_o^4} (1-n^2)^2$$

$$K_{44} = \frac{EI_z}{a_o^2} \left[1 + \frac{n^2 e}{a_o}\right]^2 + \frac{GI_t}{a_o^2} \left[\frac{na}{a_o}\right]^2 \qquad \text{(D1 a-f)}$$

$a$ = radius to midsurface of shell, as in Appendix B

$a_o$ = radius to centroid of ring stiffener

$e = a_o - a$ = radial eccentricity (vertical eccentricity must be zero)

$A$ = cross sectional area of the ring stiffener

$I_x$ = second moment of area for the cross section of the ring about the vertical axis

$I_z$ = second moment of area for the cross section of the ring about the horizontal axis

$I_t$ = torsional constant for the ring cross section

E = Young's modulus for the ring

G = Shear modulus for the ring

n = Fourier harmonic number (as in Appendix B)

The elements of the 4 × 4 stiffness matrix for the ring not stated in Eqs. D1 are either determined from symmetry, or are zero.

Lee and Nash (1982) also included the effects of prestress in the ring. As a result, they also need to consider the reduction of prestress in the shell due to the presence of the ring. This requires the axisymmetric problem to be solved before stiffness matrices for asymmetric loads can be formed. However, in the author's judgment, the stiffening effect due to prestress is approximately the same no matter whether the hydrostatic internal pressure is carried as a prestress in a ring stiffener or in the shell. Hence, assuming that all the internal hydrostatic pressure is carried as a prestress in the shell is expected to be a good approximation. This is the assumption which was made in Appendix B wherein the membrane theory was used to calculate the prestress in the shell. Thus, using the ring element without prestress along with the formulation for the shell in Appendix B accounts for all of the prestress.

## APPENDIX E

In this appendix expressions for the internal fluid pressure acting on the shell wall during a tilt test are given, and expressed as a Fourier series. The definitions of Section 3.1 are used here without restating them. Also, let the location of the surface at zero tilt be at $x = x_s$, and $d = x_s - x$ be the depth under the surface at zero tilt. Then the pressure distribution around the circumference for any given x can be written in the form

$$p = \sum_{n=0}^{\infty} p_n \cos n\theta \quad , \tag{E1}$$

in which three different expressions for the Fourier coefficients $p_n$ apply depending on whether the circumference is fully wetted, partially wetted, or not wetted.

For $x < x_s - a \tan \alpha$, the circumference is fully wetted, and

$$p_o = \gamma_f d \cos \alpha$$

$$p_1 = -\gamma_f a \sin \alpha$$

$$p_n = 0 \quad , \quad n \geq 2 \tag{E2 a-c}$$

in which $\gamma_f$ is the unit weight of the fluid.

For $x_s - a \tan \alpha < x < x_s + a \tan \alpha$, the circumference is partially wetted. The end of the wetted portion occurs at $\theta = \pm\theta_o$ in which

$$\cos \theta_o = d/(a \tan \alpha) \quad . \tag{E3}$$

The coefficients for a Fourier series which is valid on the entire circumference are

$$p_o = \frac{\gamma_f}{\pi} \left[ d \cos \alpha(\pi-\theta_o) + a \sin \alpha \sin \theta_o \right]$$

$$p_1 = \frac{2\gamma_f}{\pi} \left[ -d \cos \alpha \sin \theta_o + a \sin \alpha \left[ \frac{\sin 2\theta_o}{4} - \frac{\pi-\theta_o}{2} \right] \right]$$

$$p_n = \frac{2\gamma_f}{\pi} \left[ -d \cos \alpha \frac{\sin n\theta_o}{n} + a \sin \alpha \left[ \frac{\sin(n+1)\theta_o}{2(n+1)} + \frac{\sin(n-1)\theta_o}{2(n-1} \right] \right]$$

$$\text{for } n \geq 2 \quad . \tag{E3}$$

Finally, for $x \geq x_s + a \tan \alpha$, the circumference is entirely above the fluid, and

$$p_n = 0 \qquad \text{for all } n \quad . \tag{E4}$$

In order to obtain the nodal load vector for an element, it is necessary to multiply the Fourier coefficients $p_n$ by the appropriate interpolation functions (given in Appendix B) and to integrate vertically. When the inside of the element is fully wetted, this integration can be performed analytically. Otherwise, numerical integration must be used.

## APPENDIX F - STRESS-STRAIN RELATION FOR THE BASE PLATE

In this appendix the stress-strain relation for an elastic-perfectly plastic material with a Von Mises yield envelope in plane stress is adapted for use in the non-axisymmetric analysis of the base plate of Chapter 5. The assumption that during each loadstep, yielding occurs at a constant stress equal to the stress at the end of the loadstep is adopted. It is shown that this gives rise to what is generally known as the method of radial return, or elastic predictor, radial corrector method.

As in Eqs. 5.9 the stresses and strains are arranged into vectors

$$\sigma = \left[\sigma_r \quad \sigma_\theta \quad \sigma_{r\theta}\right]^T \tag{F1}$$

and

$$\varepsilon = \left[\varepsilon_r \quad \varepsilon_\theta \quad 2\varepsilon_{r\theta}\right]^T , \tag{F2}$$

respectively. The vertical strain $\varepsilon_z$ is also nonzero, but need not enter in the derivation. Rather than using the results for six components of stress and strain, and specializing them for plane stress conditions, it is much more convenient to derive the results directly for plane stress conditions. For this purpose note that if Drucker's postulate is valid for any closed stress path it is, in particular, valid for any closed stress path for which $\sigma_z = \sigma_{rz} = \sigma_{\theta z} = 0$. It follows that the flow rule for plane stress conditions can be written as

$$d\varepsilon^{p\ell} = \frac{\partial F}{\partial \sigma} d\lambda \quad , \tag{F3}$$

in which the partial differentiation with respect to the stress vector denotes the gradient with respect to the stress components, $\varepsilon^{p\ell}$ are the plastic strains, and

$$F(\sigma) = \tfrac{1}{2} \sigma^T A \sigma - \sigma_y^2 \qquad \text{with} \quad A = \begin{bmatrix} 2 & -1 & \cdot \\ -1 & 2 & \cdot \\ \cdot & \cdot & 6 \end{bmatrix} \tag{F4}$$

is the yield function, which vanishes on the yield surface, and $\sigma_y$ is the uniaxial yield stress. The elastic stress strain relation can be written as

$$\sigma = D\varepsilon^{e\ell} \quad , \tag{F5}$$

where

$$\varepsilon^{e\ell} = \varepsilon - \varepsilon^{p\ell} \tag{F6}$$

are the elastic strains, and

$$D = \frac{E}{1-\nu^2} \begin{bmatrix} 1 & \nu & \cdot \\ \nu & 1 & \cdot \\ \cdot & \cdot & (1-\nu)/2 \end{bmatrix} \quad . \tag{F7}$$

Using Eqs. F3, F5, F6, and the consistency condition,

$$dF = \left(\frac{\partial F}{\partial \sigma}\right)^T d\sigma = 0 \quad , \tag{F8}$$

one obtains

$$d\sigma = \left[ D - \frac{(D \frac{\partial F}{\partial \sigma})(D \frac{\partial F}{\partial \sigma})^T}{(\frac{\partial F}{\partial \sigma})^T D (\frac{\partial F}{\partial \sigma})} \right] d\varepsilon \quad . \tag{F9}$$

The expression in square brackets is the tangent material matrix. To evaluate it as a function of the stresses, note from Eq. F4 that

$$\frac{\partial F}{\partial \sigma} = A\sigma \quad . \tag{F10}$$

The tangent material matrix enables the increment in stress due to an infinitesimal strain increment to be determined. However, in the analysis of the base plate, the strain increment from one loadstep to the next is finite, rather than infinitesimal; this requires additional attention.

Henceforth, let $\sigma$ and $\varepsilon$ denote the stresses at the end of the loadstep and let $\sigma_o$ and $\varepsilon_o$ be the stresses and strains at the beginning of the loadstep. The problem at hand is to determine $\sigma$ given $\varepsilon$, $\varepsilon_o$ and $\sigma_o$. In general, $\sigma$ depends on the path from $\varepsilon_o$ to $\varepsilon$ in the three dimensional strain space. It is therefore necessary to make an assumption which will define this strain path. Perhaps the most natural assumption, and the one that is generally preferred (Krieg and Krieg, 1977; Schreyer, Kulak and Kramer, 1979), is the assumption that the total strain path is a straight line from one loadstep to the next. If this assumption is adopted, a set of ordinary differential equations can be defined for the stress path and the stress $\sigma$ at the end of the loadstep. For plane stress conditions, this set of ordinary differential equations needs to be solved numerically.

An alternative assumption, which turns out to be more convenient mathematically, is that the plastic strain path is a straight line from one loadstep to the next. This means that yielding must occur at constant stress. In addition, to define the stress and strain paths, it is assumed that the constant stress during the yielding process is the stress at the end of the loadstep, $\sigma$. As a result, the plastic strain increment for the loadstep can be written as

$$\Delta\varepsilon^{pl} = \lambda A\sigma \quad . \tag{F11}$$

The stress at the end of the loadstep is

$$\sigma = D(\varepsilon-\varepsilon_o^{pl}-\Delta\varepsilon^{pl}) \quad , \tag{F12}$$

which, after substitution from Eq. F11 becomes

$$\sigma = \sigma^* - \lambda DA\sigma \quad , \tag{F13}$$

where

$$\sigma^* = D(\varepsilon-\varepsilon_o^{pl}) \tag{F14}$$

is sometimes referred to as the elastic predictor stress. From Eq. F13, $\sigma$ can be expressed as a function of the unknown parameter $\lambda$ as follows

$$\sigma = (I+\lambda DA)^{-1} \sigma^* \quad , \tag{F15}$$

which when substituted into Eq. F4, and enforcing the yield condition, $F = 0$, gives an equation in which the only unknown is $\lambda$. To solve this equation by Newton iteration, note from Eq. F15 that

$$\frac{d\sigma}{d\lambda} = -(I+\lambda\, DA)^{-1}\, DA\sigma \quad , \tag{F16}$$

and, using the chain rule, the derivative required in the Newton-Raphson iteration can be expressed as

$$\frac{dF}{d\lambda} = (\frac{\partial F}{\partial \sigma})^T \frac{d\sigma}{d\lambda} \quad , \tag{F17}$$

which, on substitution from Eqs. F10 and F16, becomes

$$\frac{dF}{d\lambda} = -(A\sigma)^T(I+\lambda DA)^{-1}\, DA\sigma \quad . \tag{F18}$$

The numerical procedure for finding the plastic strains at each loadstep is

1. Calculate $\sigma^*$ from Eq. F14, and $F(\sigma^*)$ from Eq. F4.

2. If $F(\sigma^*) \leq 0$, no yield occurs during the loadstep, and $\sigma = \sigma^*$. If $F(\sigma^*) > 0$, continue the procedure, starting with $\sigma^o = \sigma^*$, $\lambda_o = 0$, $i = 0$.

3. Compute $\frac{dF}{d\lambda}$ from Eq. F18, with $\sigma = \sigma_i$, and obtain an improved estimate of $\lambda$ from

$$\lambda_{i+1} = \lambda_i - F(\sigma^{i+1}) / \frac{dF}{d\lambda} \quad .$$

4. Calculate $\sigma^{i+1}$ from Eq. F15 with $\lambda = \lambda_{i+1}$, and compute $F(\sigma^{i+1})$.

5. Repeat steps 3 to 4, incrementing i, each time, until

$$|F(\sigma)/\sigma_Y^2| \leq 2\varepsilon \quad .$$

This assures that the distance from the yield surface is no more than $\varepsilon$ times the yield stress. The value used for $\varepsilon$ is $0.5 \times 10^{-4}$.

The method presented here is generally known as the radial return method, which according to Schreyer et al. (1979) originated from Mendelson (1968). It has been found to give results that are in reasonably good agreement with those from the assumption that the total strain path is a straight line, no matter how large the loadstep.

## APPENDIX G - REFERENCES

American Petroleum Institute (1979), "Welded Tanks for Oil Storage," API Standard 650, 6th edn., Rev. 3.

American Water Works Association (1979), "AWWA Standard for Welded Steel Tanks for Water Storage," ANSI/AWWA D100-79, American Water Works Association, Denver, Colorado.

American Water Works Association (1984), "AWWA Standard for Welded Steel Tanks for Water Storage," ANSI/AWWA D100-84, American Water Works Association, Denver, Colorado.

Auli, W., Fisher, F.D. and Rammerstorfer, F.G. (1985), "Uplifting of Earthquake Loaded Liquid Filled Tanks," 1985 Pressure Vessels and Piping (PVP) Conference, American Society of Mechanical Engineers, New Orleans, June 1985.

Babcock, C.D. (1974), "Experiments in Shell Buckling," Thin Shell Structures, Fung, Y.C. and Sechler, E.E., eds., pp. 345-369, Prentice Hall.

Balendra, T. and Nash, W.A. (1978), "Earthquake Analysis of a Cylindrical Liquid Storage Tank with a Dome by Finite Element Method", Department of Civil Engineering, University of Massachusetts, Amherst, Massachusetts.

Bathe, K.J. (1982), Finite Element Procedures in Engineering Analysis, Prentice Hall, Inc.

Belytschko, T., Liu, W.K. and H. Stolarski (1984), "Locking and Kinematic Modes in Plate and Shell Elements," Bound Volume #H00298, ASME, 1984 PVP Conference, San Antonio, Texas, June 17-21.

Brigham, O.E. (1974), The Fast Fourier Transform , Prentice Hall, Inc.

Bushnell, D. (1970), "Analysis of Buckling and Vibration of Ring Stiffened, Segmented Shells of Revolution," Intl. J. Solids and Structures , Vol. 6, pp. 157-181.

Bushnell, D. (1974), "BOSOR5 - A Computer Program for Buckling of Elastic-Plastic Complex Shells of Revolution Including Large Deflections and Creep," Lockheed Missiles and Space Company, Inc., Sunnyvale, California.

Bushnell, D. (1981), "Computerized Analysis of Shells - Governing Equations, Technical Report AFWAL-81-3048, Appl. Mech. Lab., Lockheed Palo Alto Res. Lab., Palo Alto, California.

Cambra, F.J. (1983), "A Study of Liquid Storage Tank Seismic Uplift Behavior," Earthquake Behavior and Safety of Oil and Gas Storage Facilities, Buried Pipelines and Equipment, 1983 International Symposium on Lifeline, Earthquake Engineering, Portland, Oregon, June 19-24, T. Ariman Editor, PVP-Vol. 77, p. 37.

Chen, G. (1984), "Why the 'Elephant's Foot' Phenomenon of Liquid Storage Tank Happened," Proceedings of the Eighth World Conference in Earthquake Engineering , Vol. 7, pp. 445-452, San Francisco, California, July 21-28, 1984.

Clough, D.P. (1977), "Experimental Evaluation of Seismic Design Methods for Broad Cylindrical Tanks," University of California, Berkeley, EERC Report UCB/EERC-77/10.

Clough, R.W. and Niwa, A. (1979), "Static Tilt Tests of a Tall Cylindrical Liquid Storage Tank," Earthquake Engineering Research Center, University of California, Berkeley, Report No. UCB/EERC 79-06.

Crandall, S.H. and Norman, C.D. (1959), "An Introduction to the Mechanics of Solids," McGraw-Hill.

Flügge, W. (1960), "Stresses in Shells," Springer-Verlag.

Guo, H. and Qin, W.X. (1983), "Axisymmetric Uplift Mechanism of a Cylindrical Liquid Storage Tank," Earthquake Behavior and Safety of Oil and Gas Storage Facilities, Buried Pipelines and Equipment, 1984 International Symposium on Earthquake Engineering, 4th National Conference on Pressure Vessel and Piping Technology, Portland, Oregon, June 19-24, T. Ariman, Editor, PVP-Vol. 77, p. 102.

Hanson, R.D. (1973), "Behavior of Liquid Storage Tanks," The Great Alaska Earthquake of 1964, Engineering, National Academy of Sciences, Washington, D.C., pp. 331-339.

Haroun, M.A. (1980), "Dynamic Analyses of Liquid Storage Tanks," Earthquake Engineering Research Laboratory, Report No. EERL 80-4, California Institute of Technology, Pasadena, California, February 1980.

Haroun, M.A. (1983), "Behavior of Unanchored Oil Storage Tanks: Imperial Valley Earthquake," Journal of Technical Topics in Civil Engineering , ASCE, Vol. 109, No. 1, April 1983, pp. 23-40 (also presented at ASCE Convention, New York, May 11-15, 1981).

Haroun, M.A. and Ellaithy, H.M. (1985), "Model for Flexible Tanks Undergoing Rocking," Journal of Engineering Mechanics , Vol. 111, No. 2, Feb. 1985, pp. 143-157.

Haroun, M.A. and Housner, G.W. (1981), "Seismic Design of Liquid Storage Tanks," Journal of Technical Councils , ASCE, Vol. 107, No. TC1, Proc. Paper 16214, April 1981, pp. 191-207.

Haroun, M.A. and Housner, G.W. (1982a), "Dynamic Characteristics of Liquid Storage Tanks," Journal of the Engineering Mechanics Division , ASCE, Vol. 108, No. EM5, Oct. 1982, pp. 783-800.

Haroun, M.A. and Housner, G.W. (1982b), "Complications in Free Vibration Analysis of Tanks," Journal of the Engineering Mechanics Division , ASCE, Vol. 108, No. EM5, October 1982, pp. 801-818).

Haroun, M.A. and Tayel, M.A. (1984), "Dynamic Behavior of Cylindrical Liquid Storage Tanks Under Vertical Earthquake Excitation," Proceedings of the Eighth World Conference on Earthquake Engineering , Vol. 7, San Francisco, California, June 21-28, 1984, pp. 421-428.

Haroun, M.A. and Tayel, A.T. (1985a), "Axisymmetrical Vibrations of Tanks - Numerical," Journal of Engineering Mechanics , Vol. 111, No. 3, March 1985, pp. 329-345.

Haroun, M.A. and Tayel, A.T. (1985b), "Axisymmetrical Vibrations of Tanks - Analytical," Journal of Engineering Mechanics , Vol. 111, No. 3, March, pp. 346-358.

Housner, G.W. (1957), "Dynamic Pressures on Accelerated Fluid Containers," Bulletin of the Seismological Society of America , Vol. 47, No. 1, pp. 15-35.

Housner, G.W. (1963), "The Dynamic Behavior of Water Tanks," Bulletin of the Seismological Society of America , Vol. 53, No. 1, pp. 381-387.

Ishida, K. (1980), "Rocking Behavior of Cylindrical Liquid Storage Tanks," 7th World Conference on Earthquake Engineering , Vol. 8.

Ishida, K. and Kobayashi, N. (1985), "An Effective Method of Analyzing Rocking Motion for Unanchored Cylindrical Tanks Including Uplift," 1985 Pressure Vessels and Piping (PVP) Conference, American Society of Mechanical Engineers, New Orleans, June 1985.

Jacobsen, L.S. (1949), "Impulsive Hydrodynamics of Fluid Inside a Cylindrical Tank and of a Fluid Surrounding a Cylindrcal Pier," Bulletin of the Seismological Society of America , Vol. 39, pp. 189-204.

Jennings, P.C., Editor (1971), "Engineering Features of the San Fernando Earthquake, February 9, 1971," Earthquake Engineering Research Laboratory, Report No. EERL 71-02, Pasadena, California, June 1971.

Klein, S. (1964), "Matrix Analysis of Shell Structures," S.M. Thesis, ASRL-TR-121-12, Department of Aeronautics and Astronautics, MIT, Cambridge, Massachusetts, June 1964.

Krieg, R.D. and Krieg, D.B. (1977), "Accuracies of Numerical Solution Methods for the Elastic-Perfectly Plastic Model," Journal of Pressure Vessel Technology , ASME, pp. 510-515.

Lee, S.C. and W.A. Nash (1982), "Seismic Response of Prestressed and Ring Stiffened Liquid-Filled Tanks," Department of Civil Engineering, University of Massachusetts, Amherst, MA01003, Dec. 1982.

Leeds, D.J., Editor (1980), "Imperial County, California, Earthquake, October 15, 1979," Reconnaisance Report, Earthquake Engineering Research Institute, February 1980.

Leon, G.S. and Kausel, E.A.M. (1986), "Seismic Analysis of Fluid Storage Tanks," Journal of Structural Engineering, ASCE, Vol. 112, No. 1, pp. 1-18.

Liu, W.K. and Lam, D. (1983), "Nonlinear Analysis of Liquid-Filled Tank," Journal of Engineering Mechanics , ASCE, Vol. 9, No. 9.

Manos, G.C. and Clough, R.W. (1982), "Further Study of the Earthquake Response of a Broad Cylindrical Liquid-Storage Tank Model," Report No. UCB/EERC-82/07, July 1982.

Manos, G.C. and Clough, R.W. (1985), "Tank Damage During the Coalinga Earthquake," Earthquake Engineering and Structural Dynamics, Vol. 13, pp. 449-466.

Mendelson, A. (1968), "Plasticity: Theory and Application," MacMillan Co., N.Y.

Moore, T.A. and Wong, E.K. (1984), "The Response of Cylindrical Liquid Storage Tanks to Earthquakes," Proc. 8th World Conference in Earthquake Engineering , San Francisco, California, July 1984, Vol. 5, pp. 239-246.

Niwa, A. (1978), "Seismic Behavior of Tall Liquid Storage Tanks," Earthquake Engineering Research Center, University of California, Berkeley, Report No. UCB/EERC-78/04.

Niwa, A. and Clough, R.W. (1982), "Buckling of Cylindrical Liquid Storage Tanks Under Earthquake Loading," Earthquake Engineering and Structural Dynamics, Vol. 10, pp. 107-122.

Rinne, J.E. (1967), "Oil Storage Tanks," The Prince William Sound, Alaska, Earthquake of 1964 and Aftershocks," Vol. II, Part A, ESSA, U.S. Coast and Geodetic Survey, Washington: Government Printing Office, pp. 245-252.

Sakai, F., Ogawa, H., Isoe, A. (1984), "Horizontal Vertical and Rocking Fluid-Elastic Response and Design of Cylindrical Liquid Storage Tanks," Proceedings of the Eighth World Conference in Earthquake Engineering , San Francisco, California, July 21-28, 1984, Vol. 5, pp. 263-270.

Shaaban, S.H. and Nash, W.A. (1975), "Finite Element Analysis of a Seismically Excited Cylindrical Storage Tank, Ground Supported and Partially Filled with Liquid," University of Massachusetts, Amherst, Massachusetts, August 1975.

Shibata, H. and Akiyama, H. (1985), "Seismic Capacity Testing of a Thin Wall 500 Ton Cylindrical Tank," Bulletin of the Earthquake Resistant Structure Research Center , No. 18, Institute of Industrial Science, University of Tokyo.

Shih, C.F. (1981), "Failure of Liquid Storage Tanks Due to Earthquake Excitation," Earthquake Engineering Research Laboratory, Report No. 81-04, California Institute of Technology, Pasadena, California.

Shih, C.F. and Babcock, C.D. (1980), "Scale Model Buckling Tests of A Fluid Filled Tank Under Harmonic Excitation," ASME Century 2 Pressure Vessels and Piping Conference, August 1980, 80-C21/PVP-66.

Shih, C.F. and Babcock, C.D. (1984), "Buckling of Oil Storage Tanks in SPPL Tank Farm During the 1979 Imperial Valley Earthquake," ASME Paper No. 84-PVP-74, 1984 PVP Conference and Exhibition, ASME, San Antonio, Texas, June 17-21.

Schreyer, H.L., Kulak, R.F. and Kramer, J.M. (1979), "Accurate Solutions for Elastic-Plastic Models," Journal of Pressure Vessel Technology , ASME, pp. 226-234.

Stoker, J.J. (1968), "Nonlinear Elasticity," Gordon and Breach.

Tani, S., Hori, N. and Yamaguchi, K. (1984), "Nonlinear Dynamic Analysis of Cylindrical Tanks with Imperfect Circular Section Containing Liquid," Eighth World Conference on Earthquake Engineering , San Francisco, July 21-28, Vol. 5, pp. 247-254, 1984.

Timoshenko, S.P. and Gere, J.H. (1961), Theory of Elastic Stability , Second Edition, McGraw-Hill.

Timoshenko, S.P. and Goodier, J.N. (1970), Theory of Elasticity , 3rd ed., McGraw-Hill.

Timoshenko, S. and Woinowsky-Krieger, S. (1959), Theory of Plates and Shells , McGraw-Hill.

Turner, J.W. (1978), "Effect of Out-of-Roundness on the Dynamic Response of Liquid Storage Tanks," M.S. Thesis, Rice University, Houston, Texas, May 1978.

Veletsos, A.S. (1974), "Seismic Effects in Flexible Liquid Storage Tanks," Proceedings of the International Association for Earthquake Engineering , Fifth World Conference, Rome, Italy, Vol. 1, pp. 630-639.

Veletsos, A.S. and Kumar, A. (1984), "Dynamic Response of Vertically Excited Liquid Storage Tanks," Proceedings of the Eighth World Conference in Earthquake Engineering , Vol. 7, pp. 453-460, San Francisco, California, July 21-28, 1984.

Veletsos, A.S. and Yang, J.Y. (1977), "Advances in Civil Engineering Through Engineering Mechanics," Proceedings of the Annual EMD Specialty Conference , Raleigh, N.C., ASCE, pp. 1-24, 1977.

Weingarten, V.I., Morgan, E.J. and Seide, P. (1960), Final Report on Development of Design Criteria for Elastic Stability of Thin Shell Structures, STL/TR-60-0000-19425, Space Technology Laboratories, Inc., Los Angeles, California.

Wozniak, R.S. and Mitchell, W.W. (1978), "Basis of Seismic Design Provisions for Welded Oil Storage Tanks," Advances in Storage Tank Design API, 43rd Midyear Meeting, Toronto, Ontario, Canada.

Zienkiewicz, O.C. (1977), "The Finite Element Method," 3rd Edition, McGraw-Hill.

Zui, H. and Shinke, T. (1984), "Seismic Analysis of Cylindrical Tanks with Initial Irregularities on Side Walls," Paper No. 84-PVP-70, 1984 PVP Conference and Exhibition, American Society of Mechanical Engineers, San Antonio, Texas, June 17-21, 1984.